

**Extreme Ultraviolet Spectroscopy of Ultrafast Excitations in  
Magnetic Alloys**

by

**Sinéad A. Ryan**

MPhys, University of St. Andrews, 2018

A thesis submitted to the  
Faculty of the Graduate School of the  
University of Colorado in partial fulfillment  
of the requirements for the degree of  
Doctor of Philosophy  
Department of Physics

2024

Committee Members:

Margaret M. Murnane, Chair

Hans Nembach

Henry C. Kapteyn

Joseph Berry

Mark Hofer

Ryan, Sinéad A. (Ph.D., Physics)

Extreme Ultraviolet Spectroscopy of Ultrafast Excitations in Magnetic Alloys

Thesis directed by Prof. Margaret M. Murnane

Magnetic materials play a vital role in modern technology, serving as essential components in a wide range of applications from power generation to data storage. However, there are still many open questions about the nature of the complex quantum mechanical phenomena and many-body interactions which shape the landscape of ferromagnetism. The next generation of logic devices may rely on fast switching of magnetic states. Electronic control of magnetic states is limited to nanosecond timescales. However, we have a faster tool. Pulsed lasers can measure and manipulate magnetic materials on their fundamental timescales. In this thesis, I present experiments in which I manipulate magnetic states in alloys on their fastest timescales: ranging from few-femtoseconds spin-transfers in Heusler alloys to magnetization reorientations in ferrimagnets which take tens of picoseconds. I utilize high harmonic generation (HHG) to produce an extreme ultraviolet probe for resonant measurements of the transverse magneto-optical Kerr effect (TMOKE) at the tabletop X-MATTER beamline. In Chapter 4, by tuning the driving laser, I measure across the entire  $M$ -edges of transition metals within Heusler alloys with unprecedented resolution in both probing energy and time. Furthermore, I present the first fluence-dependent measurements of spin-transfer. In Chapter 5, I present the first ultrafast study of the material  $TbMn_6Sn_6$ . I measure a laser-induced spin reorientation on its natural timescale. I present a time-dependent model of the laser-induced reorientation which arises from competing temperature-dependent magnetocrystalline anisotropies. In this thesis, I examine the intricate relationship between energy, angular momentum, bonding, and quantum mechanical exchange within the complex many-body physics of magnetism in condensed matter systems.

## Dedication

To my family.

## Acknowledgements

The past six years spent in Boulder have been some of the best of my life. Thank you to everyone who has helped me along the way. Thank you to my supervisors Margaret Murnane and Henry Kapteyn for your wisdom and guidance. Thank you to Christian Gentry who was a patient and knowledgeable mentor while teaching me the fundamentals of our laser systems. Thank you to Emma Cating-Subramanian- your science and life advice has been invaluable. Thank you to Peter Johnsen who designed the superb X-MATTER beamline. Thank you for keeping me sane working throughout the COVID pandemic and for the hundreds of hours we spent discussing magnetism. Thank you to Mohamed Elhanoty, and the whole team at Uppsala University, for an exceptionally close and productive theory collaboration. The Heusler research would not have succeeded without your ideas, enthusiasm and hard work. Thank you to all my collaborators at NIST for sharing their fantastic samples as well as their ideas: Hans Nembach, Justin Shaw, Thomas Silva, Michael Tanksalvala, and Jacob Wisser. With special thanks to Hans and Justin for their help with the modeling of Tb166. Thank you to all my collaborators who sent so many interesting and unique alloys to study, especially our colleagues at the Max Planck Institute and University of Notre Dame. Thank you to Michael Hemmer and Michael Gerrity for their assistance with fixing broken lasers- you saved the day many times. Thank you to Anya Grafov and Na Li who assisted with so much of the work in this thesis and will continue these ideas after I leave. Thank you to Drew Morrill for being a mentor, friend and at times a guardian angel- always calling in times of flood, fire and pandemic. Thank you to Noah Schlossberger for being my first friend in Boulder. I can't believe all the fun times we have had together including learning to ski, mountain biking and working on my

car. Thank you to my friends for their good company and support: Nik, Caron, Hannah, Jet, Tehya, and many more. Thanks to Tanya Gupta who flew all the way from the UK to visit me. Thank you to Persephone Poulton for the kind words and messages across an ocean. Thank you to my family for their love and support as well as visits to Boulder. Thank you to Patrick McArdle for being my biggest cheerleader and always lending a listening ear and a shoulder to cry on. I couldn't have done it without you.

## Contents

<b>Chapter</b>	
<b>1</b>	<b>1</b>
1.1	2
1.2	3
1.2.1	3
1.2.2	5
1.3	7
<b>2</b>	<b>8</b>
2.1	8
2.1.1	8
2.1.2	10
2.1.3	11
2.1.4	11
2.1.5	15
2.2	17
2.2.1	17
2.2.2	18
2.3	20
2.3.1	21

2.3.2	Superdiffusive Spin Currents . . . . .	24
2.3.3	Electron-Magnon Interaction . . . . .	25
2.3.4	Polarized Phonon Generation . . . . .	25
2.3.5	Microscopic SOC Mediated Spin-Flips . . . . .	26
2.4	Conclusion . . . . .	26
<b>3</b>	<b>Experimental Techniques</b>	<b>27</b>
3.1	Magneto-Optical Techniques . . . . .	27
3.1.1	Resonant Magneto-Optical Techniques . . . . .	31
3.2	High Harmonic Generation . . . . .	34
3.2.1	Three-Step Model . . . . .	34
3.2.2	Phase-Matching . . . . .	38
3.3	Beamline Design . . . . .	40
3.4	Conclusion . . . . .	40
<b>4</b>	<b>Ultrafast Magnetization Dynamics in Heusler Systems</b>	<b>43</b>
4.1	Introduction to Heuslers . . . . .	45
4.2	Introduction to OISTR . . . . .	47
4.3	<i>Co<sub>2</sub>MnGa</i> . . . . .	48
4.3.1	Results for <i>Co<sub>2</sub>MnGa</i> . . . . .	49
4.3.2	Discussion of <i>Co<sub>2</sub>MnGa</i> . . . . .	59
4.3.3	Conclusion . . . . .	61
4.3.4	Supplemental Figures . . . . .	62
4.4	Comparison with <i>Co<sub>2</sub>MnGe</i> and <i>Co</i> . . . . .	70
4.4.1	Results . . . . .	72
4.4.2	Discussion . . . . .	82
4.4.3	Conclusion . . . . .	84
4.4.4	Supplemental Figures . . . . .	85

4.5	Experimental Design . . . . .	91
4.6	Future Work . . . . .	92
4.7	Conclusion . . . . .	93
<b>5</b>	<b>Spin Reorientation Transitions</b>	<b>94</b>
5.1	Introduction . . . . .	94
5.1.1	Introduction to Tb166 . . . . .	94
5.1.2	Introduction to Magnetic Switching and Spin Precession . . . . .	98
5.2	Results . . . . .	102
5.2.1	In-plane $Mn$ Moment . . . . .	102
5.2.2	Sample Temperature . . . . .	102
5.2.3	Fluence-dependent Dynamics . . . . .	104
5.2.4	Building a Model of Tb166 . . . . .	111
5.2.5	Modeling Results . . . . .	114
5.3	Conclusion . . . . .	123
5.4	Signal Normalization . . . . .	124
<b>6</b>	<b>Outlook</b>	<b>128</b>
6.1	Future Beamline Upgrades . . . . .	128
6.1.1	Temperature Control . . . . .	128
6.1.2	Sample Chamber . . . . .	130
6.1.3	Pump Upgrades . . . . .	132
6.1.4	Probe Upgrades . . . . .	135
6.2	Conclusion and Final Remarks . . . . .	135
	<b>Bibliography</b>	<b>137</b>

## Tables

### Table

1.1	Nobel prize winners. . . . .	4
2.1	A comparison of rare-Earth and transition metal magnetism. . . . .	18
5.1	Calculations of the normalization factors used for each fluence on Tb166 . . . . .	127

## Figures

### Figure

2.1	The Bethe-Slater curve. . . . .	9
2.2	Band model of ferromagnetism. . . . .	14
2.3	The Slater-Pauling curve. . . . .	19
2.4	Schematic of the three temperature model. . . . .	22
2.5	Three temperature modeling in Ni. . . . .	23
3.1	The three most common MOKE Geometries. . . . .	28
3.2	Schematic of the XMCD effect. . . . .	35
3.3	Three-step model of high harmonic generation. . . . .	35
3.4	A photo of the X-MATTER beamline. . . . .	41
3.5	The layout of optics in the X-MATTER beamline. . . . .	41
4.1	Illustration of ultrafast laser excitation and high harmonic probing of the spin system in a Heusler compound. . . . .	46
4.2	The three excitation types included in the theoretical calculations, and the ground state density of states. . . . .	50
4.3	Experimental and theoretical magnetic asymmetries. . . . .	52
4.4	Theory calculations for pump induced excitations of <i>Co</i> and <i>Mn</i> . . . . .	54
4.5	The fluence dependence of the MOKE asymmetry signal measured at the <i>Co</i> peak. . . . .	58
4.6	Experimental design. . . . .	63

4.7	Energy-dependent transient magnetic asymmetry with probing energies from 44.9 eV to 58.0 eV. . . . .	64
4.8	Energy-dependent transient magnetic asymmetry with probing energies from 58.5 eV to 72.7 eV. . . . .	65
4.9	Theoretical asymmetry curves at 0 fs, 40 fs, 80 fs and 100 fs following laser excitation from a 2.2 mJ/cm <sup>2</sup> pump pulse. . . . .	66
4.10	Fluence-dependent transient magnetic asymmetry measurements with five different probing energies from 47.9 eV to 63.6 eV. . . . .	67
4.11	The simulated transient changes in magnetic moment of Co and Mn with a pump fluence of 8.4 mJ/cm <sup>2</sup> . . . . .	68
4.12	The theoretical definition of $t = 0$ relative to the time-dependent amplitude of the simulated incident pump pulse. . . . .	68
4.13	The calculated theoretical magnetic asymmetry dynamics with and without convolving with a measurement probe. . . . .	69
4.14	The calculated spin-resolved projected density of states (PDOS). . . . .	74
4.15	The measured and calculated ground state asymmetries. . . . .	75
4.16	Examples of transient MOKE signals from the regions of enhancement that were highlighted in gray in Fig. 4.15. . . . .	78
4.17	Fluence dependence at the peak of the Co signal for the three samples. . . . .	81
4.18	The absolute enhancements in the theoretical asymmetries. . . . .	83
4.19	Energy-dependent Co dynamics from to 42.4 eV to 59.3 eV. . . . .	86
4.20	Energy-dependent Co dynamics from to 59.8 eV to 72.6 eV. . . . .	87
4.21	Energy-dependent Co <sub>2</sub> MnGe dynamics from to 42.6 eV to 57.3 eV. . . . .	88
4.22	Energy-dependent Co <sub>2</sub> MnGe dynamics from to 58.3 eV to 71.4 eV. . . . .	89
4.23	Fluence- and energy-dependent Co <sub>2</sub> MnGe dynamics. . . . .	90
5.1	Introduction to TbMn <sub>6</sub> Sn <sub>6</sub> . . . . .	97

5.2	Spin dynamics under the Landau-Lifshitz-Gilbert equation. . . . .	101
5.3	The calculated in-plane projection of the $Mn$ moment vs. temperature with an in-plane applied field of $+185 \text{ mT}$ . . . . .	103
5.4	The relationship between the static (pre-pump) magnetic signal and the recorded sample temperature. . . . .	105
5.5	Fluence-dependent measured dynamic TMOKE asymmetries of the Tb166 in-plane $Mn$ moment probed at $46.2 \pm 0.2 \text{ eV}$ . . . . .	107
5.6	Exponential fit of the experimental spin reorientation. . . . .	109
5.7	Ultrafast demagnetization of Tb166 with $1.1 \text{ mJ/cm}^2$ pump fluence. . . . .	110
5.8	A low fluence dynamic model of Tb166. . . . .	118
5.9	A 3-dimensional depiction of the dynamics of the Tb166 magnetization vector. . . . .	121
5.10	Modeling the high fluence behavior of Tb166. . . . .	123
6.1	A possible design for a combined red and blue pump arm. . . . .	134

# Chapter 1

## Motivation

As the global economy becomes increasingly dependent on big data and green energy, we should expect an ever-growing need for high-quality magnetic materials for data storage[1], wind power, and electric vehicles[2]. Approximately 90% of cloud storage utilizes perpendicular magnetic recording[3], and our data storage requirements in 2025 may be more than 90 times greater than they were in 2010[4]. One study noted that meeting global wind power targets for 2050 will require an 11- to 26- fold increase in World production of rare-Earth elements[2]. One promising avenue for future magnetic technologies is the implementation of spintronics, which makes use of both the electronic and magnetic properties of electrons. Spintronic architectures allow for more efficient data storage[5]. Additionally, ultrafast spintronics, where magnetic states are controlled by very short laser pulses, could facilitate control on much faster timescales than any existing technologies[6]. However, such advancements will require a deeper understanding of the fundamental science of ultrafast magnetism.

Since Beaupaire *et al.*'s[7] 1996 discovery of sub-picosecond demagnetization of Ni, there have been many open questions about the nature of ultrafast processes in magnetic materials. These questions have included: how can angular momentum be dissipated on such short timescales[8, 9, 10, 11], what are the dominant demagnetization pathways[12, 13, 14, 15, 16], and how do we interpret optical measurements of ultrafast magnetism[17, 18, 19, 20]?

In this thesis, I will explore laser-induced ultrafast dynamics in magnetic systems. In the first chapter, I explain the importance of magnetic materials both from a historical perspective and in relation to prospective emerging technologies. The second chapter will serve as an overview of

important concepts in magnetism with a specific focus on ultrafast effects. In the third chapter, I will provide an overview of the magneto-optical techniques utilized for sample measurements at the X-MATTER beamline. In the fourth chapter, I will give an overview of laser-induced spin-transfer effects in the Heusler alloys  $Co_2MnGa$  and  $Co_2MnGe$ , on sub 100-femtosecond timescales with unprecedented energy resolution across the  $Co$  and  $Mn$   $M$ -edges. This study investigates the manipulation of a material's spin state via the excitation of spin-polarized electrons throughout the band structure by direct laser excitation. The fifth chapter examines a longer timescales, 10's of picoseconds, in relation to laser-induced macroscopic spin precession. I investigate a spin-reorientation phase transition in the Kagome ferrimagnet  $TbMn_6Sn_6$ . Through measurement and modeling, I determine the intrinsic timescale of the phase transition. In the final chapter, I discuss the potential for future upgrades to the X-MATTER beamline and provide some concluding remarks.

## 1.1 Magnets of the Past

Magnets have been a longtime fascination for humanity's most curious minds: scientists, philosophers, and children. The oldest technological application of magnets are compasses, the development of which has allowed humans to navigate across the planet. The first magnets used for compasses were lodestones. Lodestones are a type of rock which contain ferromagnetic pieces of the iron oxide known as magnetite. Lodestones can be magnetized by lightening strikes or by lava cooling in the presence of the the Earth's magnetic field. Lodestones were independently discovered in ancient Greece, China, and Mesoamerica. It is claimed that word "magnet" comes from ancient Greek region of Magnesia where lodestone was mined[21]. The school of Greek philosophers known as Animalists believed that the properties of lodestone were divine. The ancient Greek philosopher, Thales of Miletus (famous for the quote "know thyself"), went as far as to claim that all magnets possess a soul. This idea persisted in Europe for more than two thousand years.

William Gilbert is often referred to as the "Father of magnetism". He was born in 1544 and served as Queen Elizabeth's personal physician. He performed physics experiments as a hobby. He wrote his masterpiece "De Magnete" over the course of 17 years. This work combined contemporary

knowledge of magnetism with his own experiments. It was the first written claim that the Earth is a magnet. Gilbert dispelled common myths such as the idea that magnets won't work in the vicinity of diamonds, or after being rubbed with garlic or onions. Gilbert also believed that magnets, and by extension the Earth, have souls. In *De Magnete* he states that a lodestone is a "part and choice offspring of its animate mother the earth"[22]. The philosopher and scientist, René Descartes, purported that magnetism comes from a secretion from the pores of a magnet which he called "threaded parts". This was widely accepted due to Descartes' good reputation.

The nineteenth century marked the rise of a modern scientific approach to studying magnetism. In 1819, Hans Christian Oersted discovered that a magnetic field can be created by current in a wire. One year after Oersted's discovery, Jean-Baptist Biot and Felix Savart derived an expression for the magnetic field surrounding a current carrying wire. In 1831, Michael Faraday discovered magnetic induction, and in 1865 James Clark Maxwell published his theory of electromagnetism. In the 20th century, a more atom-based and, eventually, quantum mechanical picture was developed.

Table 1.1 is a selection of Nobel Prize winners which exemplify important discoveries from the 20th century to present which have been instrumental to this thesis work. This includes work in the fields of both magnetism and optics as well as other relevant topics.

## 1.2 Magnets of the Future

### 1.2.1 Energy

Permanent magnets are our most efficient tool for converting between mechanical motion and electrical energy. This makes them a very important commodity in the energy sector. If we wish to keep up with the energy demands of modern society, while simultaneously reducing carbon emissions in light of the impending climate crisis, we will need an unprecedented quantity of high quality magnetic materials.

The conversion between mechanical energy and electrical energy via permanent magnets has allowed us to separate the generation of energy from its consumption. For example, in the past, the

Table 1.1: **Nobel prize winners.** A list of Nobel prize winning research that has contributed greatly to the science and technology utilized in this work.

Year	Awardees	Topic
2023	Pierre Agostini, Ferenc Krausz, Anne L’Huillier	attosecond pulses
2018	Gérard Mourou and Donna Strickland	chirped pulse amplification
2016	David J. Thouless, F. Duncan M. Haldane, J. Michael Kosterlitz	topology in matter
2009	Willard S. Boyle and George E. Smith	invention of the CCD
1981	Kai M. Siegbahn	laser spectroscopy
1970	Louis Eugène Félix Néel	antiferromagnetism & ferrimagnetism
1955	Polykarp Kusch	magnetic moment of the electron
1924	Karl Manne Georg Siegbahn	x-ray spectroscopy
1922	Niels Henrik David Bohr	structure of the atom
1918	Max Karl Ernst Ludwig Planck	energy quanta
1904	Lord Rayleigh	discovery of argon
1902	Hendrik Antoon Lorentz and Pieter Zeeman	Zeeman effect
1901	Wilhelm Conrad Röntgen	discovery of x-rays

location of a mill might have been chosen based on access to wind or water power. Today, we run appliances on electrical power generated by power plants which can be hundreds of miles away.

Let us consider the major sources of main's power in the United States[23]: fossil fuels (60.4%), nuclear (18.2%), and renewables (21.3%). All three of these require huge amounts of permanent magnets. Power plants can run on nuclear energy, biofuels, geothermals, or fossil fuels. All of these work on a similar principle. Heat is produced from a fuel source which generates steam. The steam turns a turbine. The technology of using steam to generate motion has not been usurped in the last 200 years. motion of the turbines then drives magnetic generators which produce electricity. Magnetic generators work by rotating very strong permanent magnets inside a coil of wire in order to generate an electric current. Wind and hydroelectric power take an even more direct approach. Wind or water turns the turbine blades which then drive a magnetic generator. A typical wind turbine requires 250-650 *kg* of NdFeB to produce 1 *MW* of electricity[24, 25]. To reach wind power targets for 2050, we will require an 11- to 26- fold increase in world production of rare-Earth elements[2].

The only exception is solar power, which accounts for 3.4% of US energy, and doesn't require any magnets. However, that isn't exactly true- solar cells are manufactured using magnetron sputtering!

Gasoline vehicles are one of the few widespread examples of a consumer product where the energy source and device are not isolated, i.e. they rely on local combustion rather than mains power or batteries. However, even in the case of gasoline cars, magnets form an important part of the car's alternator among other components. Furthermore, the push for green energy has created a rapidly growing market for electric vehicles. Permanent magnets are integral to the motor of electric vehicles and each car contain 2-4 *kg* of high quality permanent magnets.

### 1.2.2 Information Technology

Magnetic materials play a key role in the information technology sector. Historically, one very important application has been the use of magnetic materials for memory. In particular, hard disk drives (HDDs), magnetic tapes, and magnetic random access memory (MRAM) are all forms of

magnetic storage.

With the rise of machine learning, cryptocurrencies, smart devices and a growing commercial hunger for "big data", the need for efficiency data storage and computation is more relevant than ever. Since 2012, the computational resources needed to train AI models has been doubling every 3.4 months[26]. Data centers account for 1-1.5 % of the World's energy consumption[27] and Bitcoin mining consumes more energy than the country of Norway[28].

Despite HDDs, in many ways, being eclipsed by more durable and efficient solid state drives (SSDs), HDDs still account for 54% of the World's data and 90% of cloud data storage[3]. This is because HDDs are still significantly cheaper per TB of storage. The commercial viability of controlling magnetic materials with pulsed lasers (the central goal of this thesis) is about to be put to the test. Seagate will release a heat-assisted magnetic recording (HAMR) device (a 32 TB HDD with a built-in pulsed laser) for the first time this year. They are expecting to sell about one million units in the first half 2024[29].

Spintronics is a very promising emerging research field[30]. Spintronic devices utilize the electron's magnetic moment in conjunction with its charge. This adds an extra dimension to conventional electronics. Spintronic devices have the potential to be faster and more efficient than traditional semiconductor devices. This is because spin information can travel much faster than electrical signals and doesn't suffer from Ohmic heating. Two of the most important devices in the first generation of spintronics were: giant magnetoresistance (GMR) sensors and magnetic tunnel junctions (MTJ). In 1997, IBM sold the first hard disk with a GMR sensor head[31]. This is now the industry standard. GMR sensors are also popular in automotive and biosensing applications. MTJs are used for logic and memories applications. They are most often used in non-volatile memory (where stored data is not lost if power is removed). MTJs are also popular for data processing and sensing applications due to their low power consumption, small footprint, and high performance capabilities in difficult environmental conditions[32]. In coming years, emerging technologies will drive further integration of spintronic devices into the semiconductor industry. Some of these may include[33]: organic spintronics, graphene based spintronics, and single-spin logic devices.

### **1.3 Conclusion**

Magnetic materials have formed an integral part of the technological and cultural landscape of the past several thousand years. Nonetheless, the field of condensed matter physics is still very much in its infancy. Emerging magnetic technologies will shape the future of the energy and information technology sectors.

## Chapter 2

### Introduction to Magnetism in Solids

In this chapter, I will explain some of the basic physics of magnetic materials including: exchange interaction, spin-orbit coupling, Hund's rule, Stoner and Heisenberg models, magnetic anisotropy, and where to find magnetism on the periodic table. This general overview will be followed by an introduction to ultrafast magnetism. I will summarize key concepts in the field of ultrafast magnetism including: the three temperature model, Elliot-Yafet scattering, Coulomb scattering, superdiffusive spin currents, electron-magnon interactions, polarized phonon generation, and spin-flips.

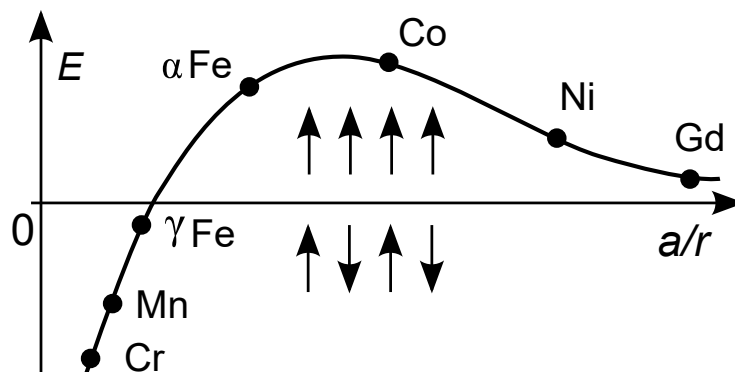
#### 2.1 Fundamentals of Magnetism

##### 2.1.1 Exchange Interaction

The exchange interaction forms the basis of magnetism in materials. In fact, prior to a very recent *Nature* publication[34], non-exchange interaction based magnetism had never been shown in an extended material. The exchange interaction is a fundamentally quantum mechanical interaction arising from the interplay of the Pauli exclusion principle with the Coulomb interaction in materials. That is to say, permanent magnets have no classical description. Next time you look a fridge magnet, consider it for what it is, an intrinsically quantum mechanical object. The exchange interaction is often treated simplistically: as a term in a Hamiltonian which acts to align or anti-align spins. In the coming paragraphs, I consider the origins of this term and find that it is deeply rooted in symmetry and lattice spacing.

The Pauli exclusion principle requires that fermions (in this case electrons) have wavefunctions which are anti-symmetric under exchange. This requires a combination of either: a spatially symmetric wavefunction with an anti-symmetric spin wavefunction, or, a spatially anti-symmetric wavefunction with a spatially symmetric wavefunction. The symmetries of the spatial electron wavefunctions in a solid are determined by the Coulomb interaction. The Coulomb interaction dictates that electrons repel each other but are attracted to nuclei. When atoms are closely packed, the Coulomb energy is minimized by symmetric spatial wavefunctions. However, when atoms in the lattice are further apart, the Coulomb energy is minimized by anti-symmetric spatial wavefunctions. The Coulomb interaction is defined by the overlap of the electron wavefunction with the lattice sites. Therefore, closely packed lattices result in symmetric spatial wavefunctions combined with anti-symmetric spin wavefunctions. Anti-symmetric spin wavefunctions come from antiferromagnetic spin alignment. Conversely, for more loosely packed lattices, anti-symmetric spatial wavefunctions are energetically preferable and, therefore, the spin coupling will be symmetric, i.e. ferromagnetic. This relationship between lattice spacing and spin coupling is exemplified by the Bethe-Slater curve, Fig. 2.1.

Figure 2.1: **The Bethe-Slater curve.** Reproduced from [35]. The x-axis represents the atomic spacing divided by the radius of the outer electron shell. The y-axis represents the exchange interaction energy. For elements with a larger  $a/r$  spacing, ferromagnetic order is preferred. For elements with a smaller  $a/r$  spacing, antiferromagnetic order is preferred. *Fe* is an interesting example where different allotropes ( $\alpha$  *Fe* vs.  $\gamma$  *Fe*) have different atomic spacings, and therefore, different magnetic orders.



The exchange interaction can manifest itself in many complex ways in real materials. Some of these include: superexchange; double exchange; and the Dzyaloshinskii–Moriya interaction (abbreviated to DMI and sometimes referred to as the anti-symmetric exchange). Superexchange occurs when magnetic ions with no direct overlap of their electronic orbitals couple via an intervening non-magnetic ion. This can lead to either ferromagnetic or antiferromagnetic coupling depending on the strength of the orbital overlap with the intervening ion. This mechanism is common in transition metals oxides where the  $2p$  orbitals of oxygen mediate a superexchange between the  $3d$  magnets. Double exchange is similar to superexchange. However, in double exchange, the magnetic ions have different valence states and the non-magnetic ions facilitate the transfer of an electron from one magnetic ion to the other. Manganites and magnetite both exhibit double exchange.

DMI arises due to the combination of strong spin-orbit coupling (see Section 2.1.2) and a crystal structure which lacks inversion symmetry. DMI favors perpendicular spin alignments unlike the exchange interaction which favors parallel spin alignments. This means DMI is required to produce many interesting non-collinear magnetic textures such as chiral domain walls and skyrmions. Inversion symmetry is broken in non-centrosymmetric crystal structures as well as in multilayer samples. Strong spin-orbit coupling can be introduced by heavier transition metals such as platinum.

### 2.1.2 Spin-Orbit Coupling

Spin-orbit coupling (SOC) is the coupling between an electron’s spin moment and its orbital motion. In the reference frame of the moving electron, the electric potential of the atomic nuclei has a magnetic component. Energy is minimized when the spin aligns with this perceived moment. SOC can give rise to preferred directions of magnetization in materials, see Section 2.1.5.2 *Magnetocrystalline Anisotropy*.

Spin-orbit coupling creates a splitting of energy levels in atoms leading to fine structure in the emission and absorption spectra. This fine structure is what led to the initial discovery of SOC in the early 20th century. Quantum mechanically, the orbital angular momentum,  $L$ , couples to the spin,  $S$ , to create  $J = L + S$ , the total angular momentum.

Although SOC is generally 10-100 times weaker than the exchange interaction[36], the importance of spin-orbit coupling in magnetic materials cannot be understated. Without the coupling of spin and lattice, magnetic materials would behave very differently. For example, we expect a compass needle to align with an externally applied field and therefore help us determine the direction of magnetic north. However, without SOC inside the compass needle, the spins would simply reorient without any motion of the needle (i.e the lattice).

### 2.1.3 Hund's Rule

Hund's rule can be used to determine the ground state of an atom. Hund's rule is composed of two parts: (1) every orbital is occupied with one spin before any orbitals are doubly filled, and (2) all electrons in singly-filled orbitals have the same spin-state.

Hund's rule assumes that the repulsion between the outer electrons is stronger than their spin-orbit interaction. Therefore, Hund's rule only applies for light atoms, where spin-orbit coupling does not dominate. This regime, dominated by electron-electron interactions, is known as the  $L - S$ , or Russell-Saunders, coupling regime.

### 2.1.4 Heisenberg and Stoner Models

There are two main competing models of magnetism: the molecular field theory of magnetism and the band theory of ferromagnetism. These are sometimes referred to as the Heisenberg and Stoner models. Both models provide useful insights into understanding magnetic materials. However, neither provides a full description. The reconciliation of these two models remains an unanswered question in magnetism.

#### 2.1.4.1 Molecular Field Theory of Ferromagnetism

In 1907, Weiss developed a phenomenological model of magnetism known as the "molecular field theory". Weiss realized that the dipolar interaction wasn't strong enough to explain ferromagnetism. However, he did not have knowledge of the quantum mechanisms of the exchange interaction.

Therefore, Weiss conceived of a molecular field,  $H_W$ , which is proportional to the magnetization,  $M$ :

$$H_W = \beta M \quad (2.1)$$

where  $\beta$  is the molecular field constant. This molecular field has extremely high field strengths for the  $3d$  transition metals, e.g. on the order of  $1000 T$ . Rather than considering the individual interactions between adjacent spins, the Weiss model describes the interactions using an effective field. With this model, Weiss and Curie created a predictive law of temperature-dependent magnetism. Specifically, the magnetic susceptibility,  $\chi$ , can be related to the temperature,  $T$ , through the Curie-Weiss Law:

$$\chi = \frac{C}{T - T_C} \quad (2.2)$$

where  $C$  is a material specific constant and  $T_C$  is the Curie temperature.  $T_C$  is the temperature at which a material loses its ferromagnetic properties and becomes a paramagnet.

Following the discovery of quantum mechanics, Heisenberg extended the molecular field theory to include the exchange interaction between neighboring spins. The Heisenberg Hamiltonian for a many spin system is given as follows:

$$H_{eff} = - \sum_{i \neq j}^N J_{ij} \mathbf{s}_i \cdot \mathbf{s}_j \quad (2.3)$$

where  $J_{ij}$  is the exchange coupling between the  $i^{th}$  spin  $s_i$  and the  $j^{th}$  spin  $s_j$ . This Hamiltonian assumes that spin contributions dominate the material's magnetism since the Hamiltonian doesn't include orbital contributions. The combination of the Weiss field with the Heisenberg Hamiltonian creates a temperature-dependent model for magnetism. However, this model fails to correctly predict the magnetic moments of transition metals.

### 2.1.4.2 Band Model of Ferromagnetism

The Stoner Model is a band-like model of ferromagnetism in metals developed in the 1930s to explain the fractional magnetic moments of the transition metals. In transition metals, magnetism comes from spins in delocalized "itinerant" orbitals which are not well described in the Heisenberg picture. In the Stoner model, the exchange interaction splits the bands of a material by spin state, Fig. 2.2. The exchange splitting is on the order of 1 eV, and it is assumed that the exchange splitting occurs due to the presence of a molecular field. The more populated, lower energy spin state, is referred to as the majority band, while the less populated, higher energy spin state, is referred to as the minority band. This can be formulated as follows:

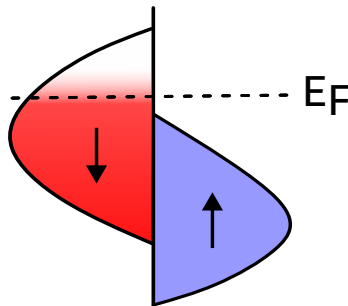
$$E_{\uparrow}(k) = \epsilon(k) - I \frac{N_{\uparrow} - N_{\downarrow}}{N}, E_{\downarrow}(k) = \epsilon(k) + I \frac{N_{\uparrow} - N_{\downarrow}}{N} \quad (2.4)$$

where  $\epsilon(k)$  is the dispersion relation of spinless electrons, and  $I$  is the Stoner parameter. The Stoner parameter is combined with the spin ratio to form the exchange energy. This formulation allows for non-integer spin moments per atom. Note that conventions differ on the assignment of spin directions for the majority and minority bands. The magnet moment,  $m$ , of a spin,  $s$ , is often defined as:  $\mathbf{m} = -2\mu_{\mathbf{B}}\mathbf{s}/\hbar$ . The negative sign in this equation means that the magnetic moment points oppositely to the "spin direction". This means, if there is a net magnetic moment in the "up direction" then majority band would be "spin-down". In this thesis, I will omit the negative sign and define the majority band as "spin-up". This will be particularly relevant in Chapter 4.

The Stoner model can be summarized by three basic assumptions: (1) the magnetic moments of transition metals (*Fe*, *Co*, *Ni*) come from the *d*-shells which are bonded into bands. (2) The energies of the spin-up and spin-down bands are shifted relative to each other due to the molecular field. (3) The bands are filled based on a Fermi-filling with temperature-dependent smearing.

One of the most important predictions of the Stoner model is the *Stoner criterion*. The Stoner criterion determines whether a material will spontaneously magnetize (i.e. be ferromagnetic) based on the satisfaction of the following condition:

Figure 2.2: **Band model of ferromagnetism.** The less populated band, i.e. red, is referred to as the minority band. The more populated band, i.e. blue, is referred to as the majority band. The bands fill up to the Fermi energy ( $E_F$ ) based on Fermi statistics. Non-zero temperature induces a Fermi smearing effect at the Fermi level. When one band is completely filled, as shown here, this is referred to as "strong ferromagnetism".



$$\frac{2\mu_B H(0)}{N} D(E_F) \geq 1 \quad (2.5)$$

where  $H(0)$  is the molecular field at 0  $K$ ,  $N$  is the number of electrons per atom in the  $d$ -shell, and  $D(E_F)$  is the density of states at the Fermi energy. That is to say, spontaneous magnetization depends, not only on the strength of the molecular field, but also the density of states at the Fermi energy.

While the Stoner model can be used to explain non-integer spins in metals, temperature-dependent effects are not well described. Unlike the Heisenberg model, the Stoner model cannot accurately predict a material's Curie temperature or other temperature-dependent effects. In fact, the Stoner model predicts Curie temperatures as large as 10,000  $K$ .

Attempts have been made to combine the two models. For example, the Self-Consistent Renormalization (SCR) theory which was first proposed by Moriya and Kawabata in 1973. The SCR theory adds correlative effects to the Stoner Model and can explain the Curie-Weiss Law. However, the reconciliation of these two approaches is still considered one of the great unsolved problems of magnetism.

### 2.1.5 Magnetic Anisotropy

Magnetic anisotropy describes differences in energy that can occur when a material is magnetized in different directions. There are several possible origins of anisotropy, with the most common being:

- (1) Shape anisotropy
- (2) Magnetocrystalline anisotropy
- (3) Magnetoelastic anisotropy.

### 2.1.5.1 Shape Anisotropy

The shape of a magnetic object influences the energy associated with magnetizing it in a given direction. These shape related energy differences are known as shape anisotropy. In general, energy is minimized when moments are oriented along the long-axis of a material. More formally, shape effects can be quantified by calculating the demagnetizing field. The demagnetizing field (or H-field) is the field generated by the magnetization of the magnet. When considering the field outside of the magnet itself, the demagnetizing field is often referred to as the stray field. Like all magnetic fields, energy is stored in the stray field. Therefore, to minimize energy, stray fields should be minimized. For example, the stray field will be much larger for a thin film which is magnetized out-of-plane rather than in-plane. Therefore, thin films have a strong shape anisotropy. Different shapes can be classified based on their "demagnetization factor",  $N$ , which represents the ratio of the demagnetizing field to the magnetizing field. For example, the demagnetizing factor of a sphere is  $1/3$ , while the demagnetizing factor for a thin film is close to zero when magnetized in-plane and close to one when magnetized out-of-plane. The shape of a magnet can be engineered to obtain desirable properties based on shape anisotropy.

### 2.1.5.2 Magnetocrystalline Anisotropy

In magnetic materials, certain crystallographic directions may be more difficult to magnetize than others. This phenomena is known as magnetocrystalline anisotropy. Magnetocrystalline anisotropy arises from the spin-orbit coupling, see 2.1.2. The relationship between orbital shape, specifically the ligand fields of neighboring atoms, and magnetocrystalline anisotropy is described in more detail by Bruno's model[37]. Magnetocrystalline anisotropy gives rise to the concept of easy and hard crystal axes. The easy axis require the least energy to magnetize. Meanwhile, magnetizing along the hard axis requires the most energy. It is important to note that the easy and hard axes are bi-directional. This means that for a material with one easy axis, there will be two stable energy minima (e.g. the up and down directions along this axis). This is an important concept in magnetic

switching. To reverse the magnetization from one direction along the easy axis to the other, the energy barrier of the hard axis must be surpassed. If there is a large energy difference between the easy and hard axes, then when the magnetization points along the easy axis, this configuration will be very stable. However, there will be a larger barrier to overcome for magnetic switching.

### 2.1.5.3 Magnetoelastic Anisotropy

Applying strain or deformations to a magnetic material will impact the shape of bonding orbitals and, therefore, change the spin-orbit coupling. The influence of stress and strain on magnetization is called magnetoelastic anisotropy. An inverse effect exists, called magnetorestriction, where the magnetization of a material induces strain. Magnetorestriction can lead to deformations and shape changes.

Magnetoelastic anisotropy means that magnetic moments in materials often align with mechanical strain. This is important to consider in the growth and manufacturing of high-quality magnets. The relationship between strain and magnetization can also be exploited in the design of sensors[38] and actuators[39].

## 2.2 Magnetism and the Periodic Table

All magnets can be grouped into two main categories: the rare-Earth metals (REs) and the transition metals (TMs). In many cases, the most desirable properties for technology applications come from alloying the REs and TMs together. Some of the main differences between the two are described in the following sections and summarized in Table 2.1.

### 2.2.1 Transition Metals

Only the first row of the transition metals ( $3d$ ) are magnetic in their pure unalloyed form. The orbital overlap of the  $4d$  and  $5d$  shells are too strong to support magnetism. The magnetism of the TMs is itinerant, meaning the electrons are delocalized.  $Ni$ ,  $Fe$ , and  $Co$  are ferromagnetic in their pure form.  $Fe$  can also be antiferromagnetic depending on the packing density of the

Table 2.1: **A comparison of rare-Earth and transition metal magnetism.**

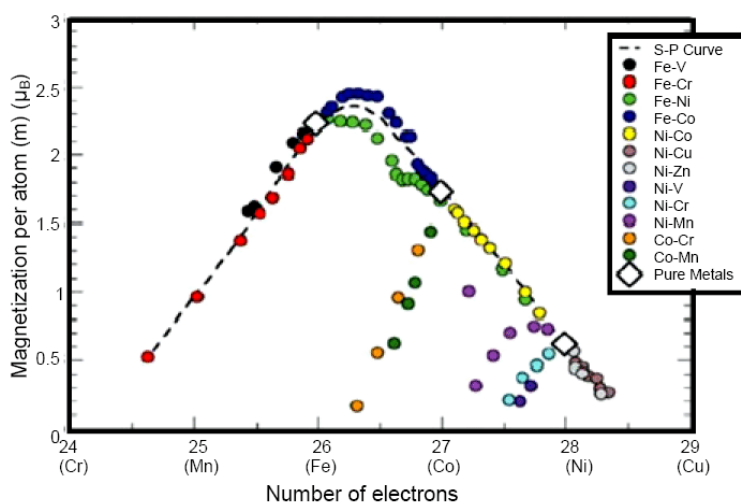
Property	Rare-Earth	Transition Metal
Magnetic Shell	localized $4f$ -shell	itinerant $3d$ -shell
Coercivity	High	Low
Magnetic Moment	High	Low
Curie Temperature	Low	High

atoms as shown in the Bethe-Slater curve, Fig 2.1. *Cr* and *Mn* are antiferromagnetic in their pure form. In a TM metal, the spherical harmonics of the individual atoms hybridize to form highly symmetric cubic harmonics. Because of this high symmetry, the TMs behave as though they have only spin moments and no orbital moments. Therefore, the observed magnetic moments don't follow Hund's rule. Instead, the relationship between the number of electrons and the magnetic moment is described by the Slater-Pauling curve, Fig. 2.3. The high symmetry of the TMs means that the magnetocrystalline anisotropy is generally low and, therefore, the magnetization direction is easy to flip, i.e low coercivity. This makes the TMs ideal for applications where the magnetization direction needs to be changed rapidly. For example, iron cores are traditionally used in electromagnets as they require only a small applied current to magnetize in the desired direction. Similarly, the magnetic platters used for perpendicular magnetic recording (PMR) in magnetic hard drives are often made of the TM alloy *CoCrPt*. The domains in the platter need to be stable enough to keep their state while having a low enough coercivity that they can be "written" without too large of an energy barrier.

### 2.2.2 Rare-Earth Metals

The  $4f$  rare-Earth metals (also known as the lanthanides) are impractical to use as magnets in their pure form and so they are generally alloyed. This is because in their pure form, they have very low Curie temperatures (e.g. 87K for *Dy* and 25 K for *Tm*) as well as being soft and reactive in

Figure 2.3: **The Slater-Pauling curve.** Reproduced from [40]. The magnetic moment of transition metals and their alloys can be related to the number of electrons.



air and water. RE elements are actually rather plentiful despite their name. However, they are only found in very low concentrations making them difficult, expensive and environmentally damaging to extract[41]. The strongest man-made magnet is neodymium which was invented rather recently (1980). Despite sharing a name with its RE constituent, it is actually an alloy between neodymium, iron and boron (NdFeB). In their alloyed form, RE magnets are still susceptible to corrosion and quite brittle. For this reason, they are generally manufactured with a protective coating, e.g. a nickel plating. RE metals have extremely high anisotropy due to their crystal structure. This makes it very challenging to change their magnetization direction, i.e. their coercivity is large. For this reason, REs are ideal for applications where it isn't desirable for the magnetization to change, e.g. as permanent magnets in motors and generators. Unlike the delocalized TMs, the REs' magnetism is confined to localized  $f$ -shells. The RE magnetism follows Hund's rule. The magnetic moment can be extremely large, with up to 7 unpaired electrons on a single atom. For example, a neodymium magnetic stores about 18 times as much magnetic energy per volume as pure iron.

### 2.3 Ultrafast Magnetism

The first discovery of sub-picosecond demagnetization came from Beaupaire *et al.* in a  $Ni$  sample in 1996[7]. This discovery was very surprising as it was previously believed that demagnetization processes require 100's of ps to occur[42, 43] as was measured in rare-Earth metals. This discovery sparked a heated ongoing debate throughout the past several decades as to the true mechanisms of ultrafast demagnetization. The main question being, how can the angular momentum of the spin system be dissipated on such short timescales? Many phenomena have been suggested as dominant effects including: Elliott-Yafet based spin-flip scattering from phonons and defects[10, 44, 45, 46, 47], electron-electron Coulomb scattering[48, 49, 45], electron-magnon scattering[50, 51, 52], superdiffusive spin currents[16, 53, 54, 55], polarized phonon generation[11], and SOC mediated spin-flips induced by a non-equilibrium distribution of electrons[56, 57].

Beaupaire *et al.*[7] explained their 1996 result with a phenomenological model called the "three temperature model" or 3TM. In the 3TM, the spin system, electron system, and phonon system all

have distinct temperature distributions. The 3TM was an extension of the existing two temperature model which describes the electrons and lattice in a metal as having distinct temperatures[58, 59]. In the 3TM, the excitation laser directly couples to the electron system through dipolar electronic excitations. The electrons quickly forms a thermal distribution through rapid electron-electron scattering. This elevated electron temperature then couples to the spin and lattice temperature baths, Fig. 2.4. The time-dependent behavior is governed by the heat capacities of each system and the coupling constants between them, Fig. 2.5. There have been several extensions to this model. For example, Koopmans *et al.*[10] created a microscopic three-temperature model (M3TM) which also accounts for conservation of angular momentum. The original 3TM only included energy conservation. Shim *et al.*[60] proposed an extended three temperature model (E3TM) which explores the role of the non-thermal electron distribution that occurs at early times. Koopmans *et al.*[44] proposed a distinction between type I and type II demagnetization which explains the much differing timescales between rare-Earth and transition metal demagnetizations.

### 2.3.1 Elliott-Yafet and Coulomb Scattering

Elliott-Yafet (EY) scattering was named after the ground breaking work of Y. Yafet[64] and R. J. Elliott[65]. It may be convenient to assume that the electrons in a ferromagnet have well-defined spin states. However, the spin-orbit interaction mixes electrons' spin states. Therefore, electrons in a ferromagnet actually exist in a superposition of up and down states. Furthermore, any scattering event between an electron and a phonon (or defect) will change the electron's state and can, therefore, change the probability of finding that electron in a spin-up or spin-down state. Because the scattering event changes the electron's spin state, there is a transfer of angular momentum between the spin system and the lattice. This electron-phonon scattering can occur on very short timescales. Therefore, this provides a pathway for spin-flips on the 100 *fs* timescales observed in ultrafast demagnetization. This scattering channel is known as Elliot-Yafet scattering.

Coulomb scattering is related to the mechanisms of EY scattering as it also relies on the presence of spin-orbit interaction to mediate angular momentum transfer to the lattice. However,

Figure 2.4: **Schematic of the three temperature model.** The electron bath is excited by the pump laser pulse. The rate of energy transfer between the three temperature baths is mediated by the strength of the coupling between them:  $G_{e-s}$ ,  $G_{l-s}$ ,  $G_{e-l}$ .

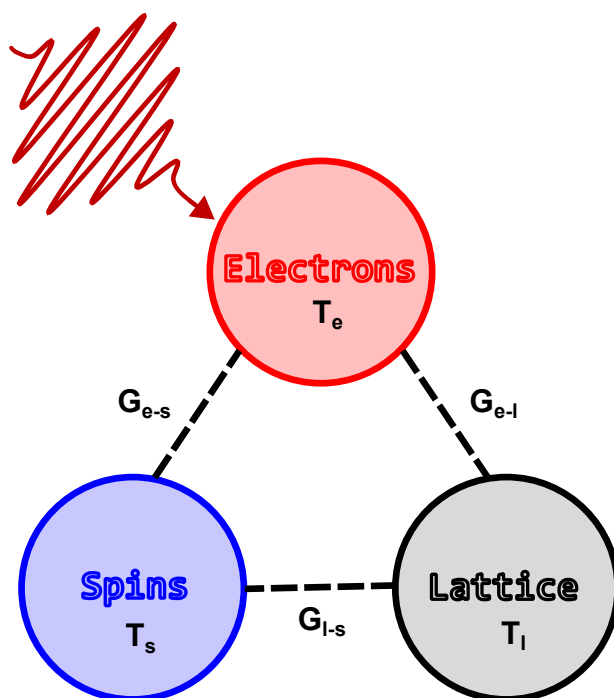
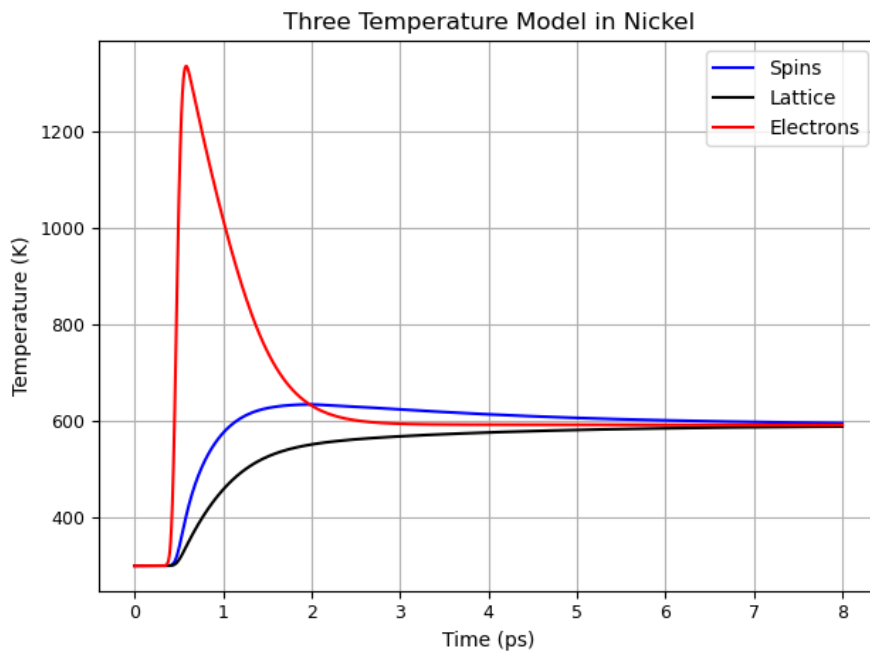


Figure 2.5: **Three temperature modeling in Ni.** An example of the three temperature model applied to the ultrafast excitation of Ni. The incident fluence is  $2.4 \text{ mJ/cm}^2$  at  $780 \text{ nm}$  and an incidence angle of  $50^\circ$ . This model was created using the NTMPy python package[61] developed by Alber *et al.*[62]. Temperature-dependent heat capacities of the *Ni* spin and electron systems were obtained Tengdin *et al.*[63].



instead of being based on electron-phonon or electron-defect scattering, Coulomb scattering is based on electron-electron scattering. EY scattering is generally considered to be quasi-elastic. This means that it can only cause a spin-flip between states in the minority and majority bands if they are energetically close. However, electron-electron scattering is not quasi-elastic and so there are many more options for possible transitions between minority and majority bands[48]. This argument may be used to justify the importance or dominance of Coulomb scattering over Elliot-Yafet scattering.

### 2.3.2 Superdiffusive Spin Currents

Superdiffusive spin currents cause an ultrafast reduction in the magnetization of a material by rapidly transporting spin polarization away from the region of probing. This overcomes the issues of angular momentum dissipation on ultrafast timescales by simply transporting angular momentum rather than dissipating it. The term "superdiffusive" is used because the transport characteristics cannot be classified as either ballistic nor diffusive. The transport is initially ballistic and then transitions into a more diffusive regime before becoming fully diffusive. Battiato *et al.*[55] proposed a semi-classical model for this superdiffusive regime. The same authors published a follow up study analyzing superdiffusive spin transport in layered heterostructures[66]. The formation of a superdiffusive spin current is reliant on differing lifetimes between spin-up and spin-down bands. This leads to increased transport for one spin-species over the other. Spin-polarized electrons which are transported out of the region must be replaced to maintain a net zero charge (as one would expect in a conductor). Therefore, there is a compensating flow of diffusive spin-down electrons into the region.

One of the most conclusive demonstration of superdiffusive spin currents was the work of Turgut *et al.*[16], inspired by [53], where spin currents were transmitted from a laser pumped *Ni* sample into a *Fe* sample separated by a spacer layer. The *Fe* layer either experienced a transient reduction or enhancement in magnetization (this was dependent on whether it was coupled ferromagnetically or antiferromagnetically with the *Ni* layer). Furthermore, the strength of the changes in the *Fe* magnetism could be controlled by choosing either a spin-transmitting or spin-scattering spacer layer.

The timescale of the *Ni* demagnetization, and the concurrent changes in the *Fe* magnetization, were on the order of a few hundred femtoseconds.

Another experimental work showed that superdiffusive spin currents could travel from laser excited gold into an adjacent magnetized *Ni* layer, leading to the demagnetization of the *Ni*[54]. Meanwhile, other experiments have contested the importance of the contribution of superdiffusive spin currents[67, 68].

### 2.3.3 Electron-Magnon Interaction

Magnons are quasi-particles composed of quantized bosonic spin waves. They represent a collective excitation of the spin system. The generation of one magnon lowers the magnetization of a ferromagnet by two Bohr magnetons. The energy of a magnon depends on its wavelength, i.e. how many lattice sites a single spin-flip is spread over. Under equilibrium conditions, and below the Curie temperature (i.e. in the ferromagnetic phase), the magnetization of a material deviates from its saturation value based on a temperature-dependent Bose-Einstein distribution of magnons. Ultrafast laser excitation creates a hot electron distribution where collisions can take place in a momentum regime which far exceeds the normal range of Fermi-smearing in equilibrium. Since the majority band is mostly filled, most spin-flip processes will move electrons from the majority band into the minority band. Individual spin-flips then decay into magnons modes[50]. This can be thought of a plucked string decaying into constituent harmonic modes. These magnon modes are quenched by the spin-orbit coupling. This allows a transfer of spin momentum to the lattice. This scheme present a method of transferring angular momentum from the spin-system to the lattice without any scattering with phonons (i.e. the EY scattering description).

### 2.3.4 Polarized Phonon Generation

Polarized phonon generation is a relatively new theory[11] which proposes that angular momentum can be conserved during ultrafast demagnetization because it is transferred to the lattice through the generation of circularly polarized phonons in an ultrafast analogy to the Einstein-de

Haas effect. The Einstein-de Haas effect is the striking observation that changing the magnetization of a suspended magnet will cause it to rotate. The angular momentum change in the spin system is compensated by a macroscopic rotation of the entire material. This is the only experiment that Einstein ever performed! The spin-phonon coupling mechanism which mediates the creation of polarized phonons is similar to EY. However, in this case, it is made more efficient by specifically inducing high-frequency polarized phonons.

### 2.3.5 Microscopic SOC Mediated Spin-Flips

In the time-dependent density functional theory (TD-DFT) calculations presented in Chapter 4, only one unit-cell of the lattice can be calculated due to limitations in available computational power. This means that spatial effects like electron-phonon scattering or magnon generation cannot be modeled. In the TD-DFT, the main mechanism for ultrafast demagnetization are sub 100-fs SOC mediated spin-flips with a microscopic origin. This mechanism is explained more in Section 4.3.1 and is based on the work of Elliott *et al.* [56] and Krieger *et al.* [57].

## 2.4 Conclusion

In this chapter, I began with an overview of the two most important concepts for understanding magnetic materials: the exchange interaction and spin-orbit coupling. I then explained the two major theoretical frameworks used to describe ferromagnetism: the Heisenberg and Stoner models. This led to a discussion of magnetic anisotropy, which defines the energy landscape of magnetic materials. I examined the two regions of periodic table which give rise to ferromagnetism: the transition metals and the rare Earth metals. The last part of this chapter gave an overview of the vast array of competing theories in the field of ultrafast magnetism. These concepts will be important in Chapters 4 and 5, which examine ultrafast magnetism in specific materials.

## Chapter 3

### Experimental Techniques

This chapter is divided into three parts. The first part is a discussion of magneto-optical techniques which are utilized for the measurements in Chapters 4 and 5. The second part of this chapter is a discussion of the physics of high harmonic generation. High harmonic generation (HHG) is used to generate extreme ultraviolet (EUV) probing energies for the magneto-optical measurements. The final section is a discussion of the design of the X-MATTER beamline where measurements were performed.

#### 3.1 Magneto-Optical Techniques

Magneto-optical techniques exploit the relationship between light and magnetic materials. All magneto-optical spectroscopies arise from the interaction of polarized light with the orbital motion of spin-polarized electrons. Therefore, magneto-optical spectroscopies provide a delicate probe of the interplay between the spin and orbital states which create a material's magnetism.

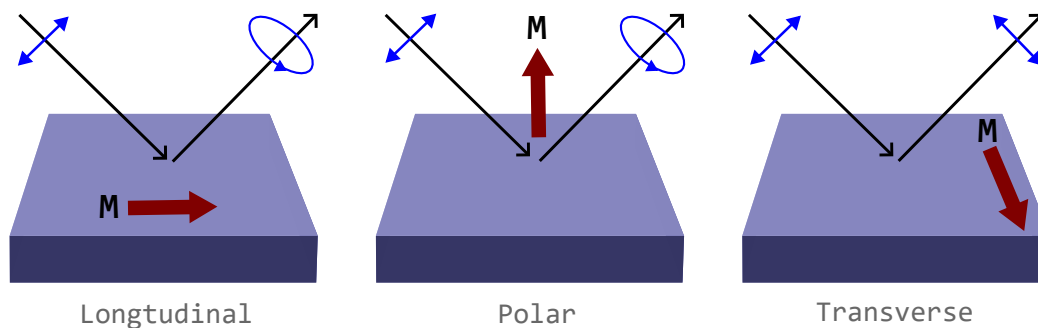
The first magneto-optical effect to be discovered, and perhaps the most famous, is the Faraday effect. The Faraday effect describes the rotation of linearly polarized light under the influence of a magnetic field inside a material. The strength of the rotation of the polarization is proportional to the magnetic field along the direction of propagation. This effect was first discovered by Michael Faraday in 1845 when observing the transmission of light through a piece of lead borosilicate glass in the presence of a magnetic field[69].

The Magneto-Optical Kerr Effect (MOKE) was first discovered by the Scottish physicist John

Kerr in 1876 when he reflected linearly polarized light from the surface of a piece of magnetized iron[69]. MOKE is an effect by which the polarization of light changes when reflected from a magnetic surface. The work of Faraday, Kerr and their contemporaries, in discovering magneto-optical effects, provided an important clue in understanding that light as an electromagnetic phenomenon. Therefore, these discoveries of the 19th Century provided not just a new technique to probe a material's magnetism, but also provided an important contribution to understanding the fundamental nature of light itself[69].

The main advantage of MOKE, over non-optical measurement techniques, is that MOKE provides an ultrafast non-destructive probe of a material's transient magnetism. There are several MOKE geometries. In each of them, linearly polarized light is reflected from a sample's surface. The magnetism of the sample's surface creates either a polarization change or intensity modulation in the reflected beam, Fig. 3.1. This change is measured and directly related to the magnetic properties of the material.

Figure 3.1: **The three most common MOKE geometries.** Longitudinal (LMOKE) and Polar (PMOKE) rely on analyzing the polarization rotation and ellipticity of the reflected beam. Transverse (TMOKE) relies on analyzing an intensity modulation in the reflected beam.



MOKE measurements can be made ultrafast by using short pulses of light to excite and measure the sample. One pulse is used as a pump (to excite transient behavior in the sample), and another is used as a probe, to measure the response after a fixed delay. Generally, different

wavelengths of light should be used for the pump and probe to avoid photo-bleaching effects. Most often, the probe is at a higher energy than the pump. The higher energy photons needed for the probe are commonly generated using either a frequency doubling crystal or through the process of high harmonic generation, Section 3.2. A mirror mounted on a computer controlled stage can be used to change the optical path length of either the pump or probe pulses, and therefore, digitally set the time delay between the pump and probe pulses. With this technique, we can map out a time-dependent response.

TMOKE was discovered much later than PMOKE and LMOKE as it is the least intuitive MOKE geometry. TMOKE was theoretically predicted by C. H. Wind in 1898[70] and while the author, "found no opportunity to undertake any experiments himself in this direction" the technique was tested by Zeeman who "kindly tried to detect the new effect on iron mirrors". TMOKE is preferred for EUV measurements because high quality polarization sensitive optics are hard to design and have very low efficiency in the EUV regime. However, intensity changes can be measured very accurately with an EUV sensitive CCD.

To understand the origin of the TMOKE contrast, consider the permittivity of a material magnetized along the z-axis:

$$\epsilon = \begin{pmatrix} \epsilon_{xx} & \epsilon_{xy} & 0 \\ -\epsilon_{xy} & \epsilon_{yy} & 0 \\ 0 & 0 & \epsilon_{zz} \end{pmatrix}. \quad (3.1)$$

In an isotropic material, the permittivity is the same in all directions, i.e.  $\epsilon_{xx} = \epsilon_{yy} = \epsilon_{zz}$  and the off-diagonal elements are all zero. Magnetic materials are never isotropic because the axis of magnetization breaks symmetry. The off-diagonal element of the dielectric tensor,  $\epsilon_{xy}$ , represent the coupling of the motion of electrons along the x and y-axes due to the magnetization along the z-axis. There are many non-magnetic cases where off-diagonal elements may be non-zero in a

dielectric tensor. For example, if the measurement axes don't line up with the crystallographic axes or the crystal itself is not cubic. However, in the case of equal and opposite off-diagonal terms as depicted in Eq. 3.1, this is a hallmark of magnetism. An effective MOKE measurement scheme must measure a physical property which is fundamentally related to  $\epsilon_{xy}$ . The following passage explores the TMOKE geometry as a way to measure  $\epsilon_{xy}$ .

Based on the Fresnel equations, the reflection coefficients of a material can be calculated. We obtain the reflection coefficient,  $r_p$ , for a  $p$ -polarized incident beam with an incidence angle of  $\theta_i$ . We consider two different in-plane sample magnetizations with opposite directions, both of which are perpendicular to the plane of the incident laser beam. These magnetizations will be referred to as '+' and '-'. In this case, the expression for  $r_p$  is:

$$r_p(\pm) = \frac{n \cos \theta_i - \cos \theta_r}{n \cos \theta_i + \cos \theta_r} \pm \epsilon_{xy} \frac{2n \cos \theta_i \sin \theta_r}{n^2 (n \cos \theta_i + \cos \theta_r)^2}. \quad (3.2)$$

Here, it is assumed that  $\epsilon_{xx} = \epsilon_{yy}$ , and  $n = \sqrt{\epsilon_{xx}}$ .  $\theta_r$  is the angle of refraction. Therefore, from Snell's law,  $\theta_r = \sin^{-1}(\sin \theta_i / n)$ . The expression for  $r_p(\pm)$  can be written in a simplified form:

$$r_p(\pm) = r_p^{(0)} \pm \epsilon_{xy} r_p^{(1)}. \quad (3.3)$$

The reflected intensity,  $I_p = I_0 |r_p|^2$ , where  $I_0$  is incident intensity, is therefore given by:

$$I_{\pm} = I_0 \left| \frac{n \cos \theta_i - \cos \theta_r}{n \cos \theta_i + \cos \theta_r} \pm \epsilon_{xy} \frac{2 \sin \theta_i \cos \theta_i}{n^2 (n \cos \theta_i + \cos \theta_r)^2} \right|^2 \quad (3.4)$$

Expanding  $I_{\pm}$  to first order in  $\epsilon_{xy}$ , and expressing it in the simplified form described above yields:

$$I_{\pm} \approx I_0 (|r_p^{(0)}|^2 \pm 2 \text{Re}(\epsilon_{xy} r_p^{(0)*} r_p^{(1)})). \quad (3.5)$$

The magnetic asymmetry,  $A$ , is defined as follows:

$$A = \frac{I_+ - I_-}{I_+ + I_-}. \quad (3.6)$$

Using the approximation for  $I_{\pm}$  from Eq. 3.5, this becomes:

$$A \approx 2Re \left( \frac{\epsilon_{xy} r_p^{(0)} r_p^{(1)}}{|r_p^{(0)}|^2} \right). \quad (3.7)$$

This can be expanded with the full expressions for  $r_p^{(0)}$  and  $r_p^{(1)}$ :

$$A \approx 2Re \left( \frac{\epsilon_{xy} \sin(2\theta_i)}{n^4 \cos^2 \theta_i - n^2 + \sin^2 \theta_i} \right). \quad (3.8)$$

Therefore, the magnetic asymmetry,  $A$ , is proportional to  $\epsilon_{xy}$  and is independent of  $I_0$ , the initial intensity of the probe. TMOKE contrast is obtained by measuring  $I_+$  and  $I_-$  to obtain the magnetic asymmetry,  $A$ , which is proportional to  $\epsilon_{xy}$ .

### 3.1.1 Resonant Magneto-Optical Techniques

Visible probes are most common for MOKE techniques, due to the affordability, availability and relative ease of use of visible lasers. However, signals measured in the EUV and x-ray regimes have fewer non-magnetic artifacts than visible probes[20] and can measure with element specificity. By making measurements at magnetically active absorption edges (e.g.  $3d$  final states for TMs or  $4f$  final states for REs) there is a large enhancement of the overall MOKE signal and one can attribute magnetic signals to individual elements at their absorption-edges. This gives a unique picture of how the magnetization of individual elements within an alloy or multilayer sample evolve on ultrafast timescales.

Magnetically active absorption edges are measured using probe photon energies which are resonant with the energy differences between core levels and exchange split valence bands. In this thesis, I will address the  $M_{2,3}$ -edges ( $3p \rightarrow 3d$ ) of transition metals using an EUV probe in the range of 40-72 eV. I produce these  $M$ -edge photon energies with a tabletop source using a process known as high harmonic generation (HHG).

Rare-Earth magnets may be probed using the  $M_{4,5}$ -edges ( $3d \rightarrow 4f$ ) or  $N_{4,5}$ -edges ( $4d \rightarrow 4f$ ). However, accessing these edges requires soft x-ray photon energies:  $\sim 100$ -200 eV for the  $N_{4,5}$ -edge,

and  $\sim 1\text{-}2\text{ keV}$  for the  $M_{4,5}$ -edge. With soft x-rays, the  $L_{2,3}$ -edges ( $2p \rightarrow 3d$ ) of transition metals can also be probed,  $\sim 0.7\text{-}0.9\text{ keV}$  for *Fe*, *Co* and *Ni*. Coherent soft x-rays are most commonly produced at large-scale user facilities such as synchrotrons or free electron lasers (XFELs). However, tabletop coherent soft x-rays can be produced through high harmonic generation if a sufficiently long wavelength driving laser is used[71, 72]. See Section 3.2 for a discussion of the importance of driving wavelength in HHG. In this thesis, I will use an 800 nm Ti:Sapphire system to drive HHG. Therefore, I am limited to  $M$ -edge measurements of transition metals.

$L$ -edge measurements of transition metals have many advantages over  $M$ -edge measurements. At the  $M$ -edge, the absorption edges of different elements can strongly overlap. This limits the ability to separate individual elemental contributions to the magneto-optical signal unless a material is chosen whose constituent elements have well separated absorption edges. In Chapter 4, I study multi-element magnets containing both *Mn* and *Co*. Luckily, these elements are relatively well separated at the  $M$ -edge ( $\sim 12\text{ eV}$ ) compared to, for example, *Co* and *Fe* whose edges are separated by only at  $\sim 6\text{ eV}$ . By comparison, at the  $L$ -edge, the *Co* and *Fe* edges are 10 times more separated in energy. Furthermore, the  $L_2$  and  $L_3$  edges are well separated for each element. This is unlike the  $M$ -edge where the  $M_2$  and  $M_3$  edges can strongly overlap.

Separately resolving the  $L_2$  and  $L_3$  edges allows the spin and orbital contributions of a material's magnetism to be disentangled. I will demonstrate this using the example of a magneto-optical technique known as x-ray circular dichroism (XMCD).

XMCD is a very popular technique for obtaining element specific magnetic contrast using resonant x-rays. XMCD has strong analogies to the EUV TMOKE techniques used in this thesis. XMCD is a measurement of the difference in absorption between left and right-circularly polarized photons by a magnetic material. The origins of the dichroism can be thought of as a two-step process: (1) Circularly polarized photons excite specific core-shell electrons. (2) The spin-polarized valence shell acts a spin-selective detector due to the exchange splitting.

Photoexcitation changes the orbital momentum of an electron by  $\pm 1$  based on dipole selection rules. The spin state of the electron, however, is unchanged. Therefore, if the majority valence band

is filled, and only the minority valence band has available states, then only minority electrons can be excited from the core-shell to the valence band.

To demonstrate this, I will examine a  $2p \rightarrow 3d$  excitation in a transition metal, a common XMCD measurement. The  $2p$  core shell is split by spin-orbit coupling into  $2p_{1/2}$  ( $L_2$ -edge) and  $2p_{3/2}$  ( $L_3$ -edge). The energy difference between these split  $2p$  states is rather large, approximately 15 eV. The  $2p_{3/2}$  state contains four electrons, while the  $2p_{1/2}$  state contains only two electrons. Applying the dipole operator to the  $2p_{3/2}$  state for a photoexcitation with a +1 polarization state gives a 62.5% chance of exciting a minority electron and a 37.5% chance of exciting a majority electron. Meanwhile, for the  $L_2$ -edge, a polarization state of +1 has a 75% chance of exciting a minority electron, and a 25% chance of exciting a majority electron. The XMCD signal is obtained by measuring the absorption spectrum with +1 and -1 polarizations and then calculating the difference signal,  $(\mu^- - \mu^+)$ , Fig. 3.2.

The magnitude of the dichroism is dictated by a few factors: proper aligned of the photon spin with the magnetization axis; the quality of the circular polarization achieved; and the degree of spin polarization of the valence shell in the material.

Based on the selection rules, sum rules can be derived for both the spin and orbital moments per atom. The spin sum rule take the following form:

$$m_s = \frac{\mu_B \langle -A + 2B \rangle}{C} \quad (3.9)$$

where  $m_s$  is the spin moment per atom,  $A$  is the intensity of  $L_3$  XMCD spectrum,  $B$  is the intensity of the  $L_2$  XMCD spectrum, and  $C$  is a proportionality constant based on the number of holes and the x-ray absorption intensity. The angle brackets represent the angle-average of every in-plane sample orientation. For a polycrystalline sample, the angle-averaged value is obtained for any single measurement angle.  $A$  and  $B$  are shown in Fig. 3.2(b).  $C$  takes the same value in both the orbital and spin sum rules and can be determined precisely through x-ray absorption spectroscopy (XAS),

Fig. 3.2(b). The orbital sum rule takes the following form:

$$m_o = \frac{-2\mu_B \langle A + B \rangle}{C} \quad (3.10)$$

where  $m_o$  is the orbital moment per atom.

XMCD provides an invaluable tool to determine the magnetization of a sample with element specificity and separate spin and orbital contributions. The XMCD selection rules give an illustrative example of the power of using magneto-optical techniques with high-energy resonant probes.

## 3.2 High Harmonic Generation

High harmonic generation is a process whereby strong non-linear effects between the large electric fields of a focused pulsed laser and the atomic potentials within a target medium can create coherent pulses with energies corresponding to multiples, of five or more, of the original driving laser energy. The target can be a gas, plasma, solid or liquid. In this thesis, I use Nobel gas targets. Nobel gas targets produce the highest energies due to their large ionization energies ( $\sim 15\text{-}20\text{ eV}$ ). By symmetry, in a gas target, only odd harmonics are produced.

### 3.2.1 Three-Step Model

A simple model for understanding high harmonic generation was developed by Kulander, Corkum and Lewenstein from 1991-1994[74, 75, 76]. This model contains three steps: tunnel ionization, acceleration and recombination, Fig. 3.3. This is known as the "three-step" or "simple man's model" and represents a semi-classical approach. Ionization and recombination are treated quantum mechanically while Newtonian physics and electromagnetism are used to describe the electron's acceleration. One limitation of this model is that it assumes that there is only one active electron.

The first step of the three step model is the ionization of an electron via quantum tunneling. The potential well of the parent ion is superimposed with the asymmetrical potential gradient

Figure 3.2: **Schematic of the XMCD effect.** Reprinted from [73] with permission from Elsevier. The x-ray absorption cross-sections are different for the two orthogonal circular polarizations of incident photons. The cross-sections calculation is based on the spin and orbital states of the core shell ( $2p$ ) combined with the spin-polarization of the available final states in the valence shell. Initial and final states are depicted in (a), while (b) shows the corresponding x-ray absorption spectroscopy (XAS) signal and x-ray magnetic circular dichroism (XMCD) intensities.

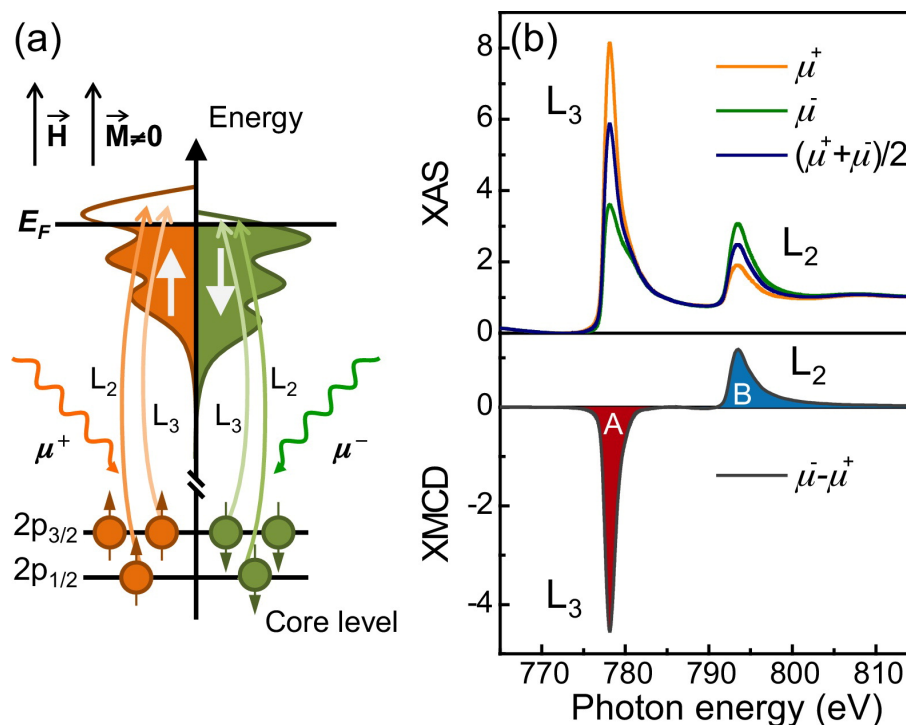
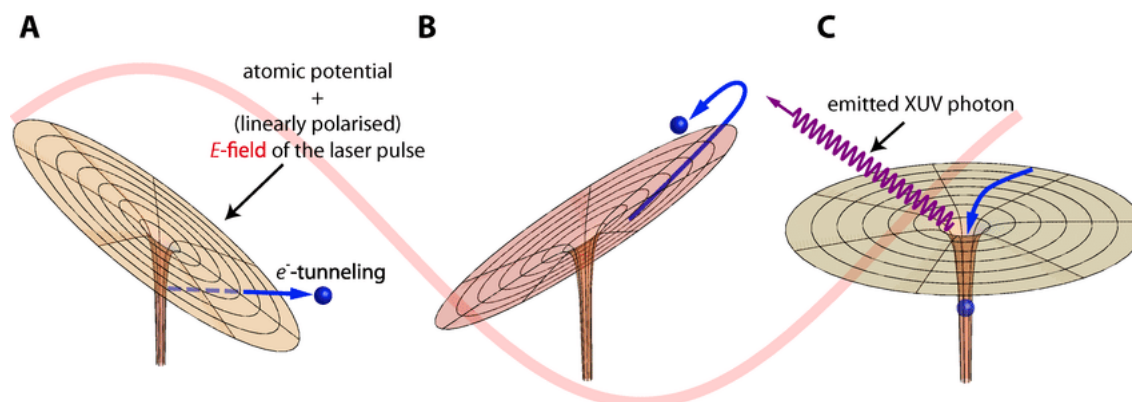


Figure 3.3: **Three-step model of high harmonic generation.** Reproduced from Kern *et al.*[77]. The three steps are: (A) Tunnel Ionization, (B) Acceleration and (C) Recombination.



from the electric field of the driving laser. The ionization rate is time-dependent and ionization is most likely to occur when the electric field of the laser is at a maximum, Fig. 3.3(a). The rate of ionization is described by the fully quantum mechanical Ammosov-Delone-Krainov (ADK) equation[78]. Increasing the laser intensity will increase the ionization rate until a threshold is reached where the gas becomes over ionized. Over ionization reduces the HHG flux. In general, tunnel ionization requires energy densities of  $> 10^{14}W/cm^2$ . Achieving these enormous energy densities generally requires focusing high intensity ultrashort laser pulses.

After the electron is ionized, it is assumed to initially have zero velocity and then its acceleration  $\ddot{x}(t)$  can be described classically:

$$m\ddot{x}(t) = -eE_0\cos(\omega t) \quad (3.11)$$

where  $e$  is the electron charge,  $m$  is the electron mass,  $E_0$  is the amplitude of the electric field of the driving laser, and  $\omega$  is the angular frequency of the field. Electrons can be ionized throughout all phases of the driving laser field oscillation. However, there is only a specific range of phases where the electron trajectories are closed, i.e. they will return to the parent ion and have a possibility to recombine. Solving Eq. 3.11 for electron displacement,  $x$ , one obtains:

$$x(t) = \frac{eE_0}{m\omega} \left( (t - t_i)\sin(\omega t_i) + \frac{1}{\omega}(\cos(\omega t) - \cos(\omega t_i)) \right) \quad (3.12)$$

where  $t_i$  is the time during the laser cycle when the electron is initially ionized. The closed trajectories are those where the electron returns to  $x(t) = 0$  within a single cycle, i.e. the electron will return to its starting location- inside the potential well of the atom. The pondermotive energy,  $U_p$ , is the time-averaged kinetic energy of the electron based on Eq. 3.12. The expression for  $U_p$  is as follows:

$$U_p = \frac{e^2 E_0^2}{4m_e \omega^2} \quad (3.13)$$

By solving Eq. 3.12 for the maximum potential energy one obtains  $E_{k,max} \approx 3.17U_p$ . Therefore, the maximum photon energy ( $\hbar\omega_{cut-off}$ ) for the HHG process is a combination of the maximum

potential energy and the ionization potential of the atom,  $I_p$ :

$$\hbar\omega_{cut-off} \approx 3.17U_p + I_p. \quad (3.14)$$

$I_p$  depends on the choice of gas. For example, Helium has the highest  $I_p$  of the Nobel gases at 24.6 eV. Neon is the second highest at 21.6 eV. The gas choice is important for not only determining the value of the  $I_p$  term, but also for determining the maximum allowable driving laser power where phase-matching is achieved. This will be explored more in the discussion of phase-matching in Section 3.2.2. Gases with higher ionization potentials can be driven harder while still achieving phase-matching. Therefore, they can produce higher energy harmonics. This relationship between ionization potential and the maximal phase-matched driving power is more important in determining the cut-off energy in Eq. 3.14 than the contribution of the  $I_p$  term itself (which differs by only  $\sim 11$  eV from neon to krypton).

Aside from driving the gas medium with higher laser powers,  $U_p$  can also be increased by increasing the length of the driving wavelength. If there is a longer period of time between laser field cycles, the electron has a longer time to accelerate before it recombines. This means that higher energies can be achieved. This can be seen from the dependence of  $U_p$  on  $\omega$  in Eq. 3.13. In this thesis, I use a Ti:Sapphire based laser system due to the excellent properties of Ti:Sapphire for generating high intensity ultrashort laser pulses. The central wavelength from this system is approximately 800 nm.

The three-step model can effectively predict the photon cut-off energy for a single atomic emitter. However, it cannot explain many important aspects of HHG such as the effects of the laser pulse's chirp, polarization, waveform or orbital angular momentum.

The period of the three-step process is  $T/2$  where  $T$  is the period of the driving laser. A period of  $T/2$  corresponds to a frequency of  $2f$ . The lowest achievable frequency is the original frequency itself,  $f$ , and further additions of  $2f$  account for the observed odd harmonics.

### 3.2.2 Phase-Matching

The three-step model presented in the previous section is for a single atomic emitter. However, a full understanding of the HHG process requires the consideration of an entire cloud of atoms interacting with the laser pulse. It is imperative that photons produced via HHG are in phase with each other. This allows them to interfere constructively and produce a bright and coherent EUV pulse. Phase-matching requires that the phase velocity of the EUV beam and the driving laser be equal. Otherwise, the generated and generating beams will become out of sync and destructive interference will ensue.

Several effective geometries have been utilized for high harmonic generation, the most simplistic of which is a gas jet[79]. Hollow cores fibers have been shown to increase the phase-matching efficiency of HHG[80], and are used extensively by our research group. In this thesis, a semi-infinite gas-cell geometry will be utilized[81] which achieves a useful balance between photon flux and ease of use.

The following equation describes the phase mismatch,  $\Delta k$ , between a driving laser and its HHG beam generated in a hollow core fiber filled with gas[80, 82, 83]:

$$\Delta k \approx q \left( \frac{u_{11}^2 \lambda}{4\pi a^2} - P(1 - \eta) \frac{2\pi}{\lambda} (\Delta\delta + n_2) + P\eta n_a r_e \lambda \right) \quad (3.15)$$

for the  $q^{th}$  harmonic, where  $u_{11}$  is the first zero of the Bessel function  $J_0$  ( $\approx 2.4$ ),  $P$  is the pressure,  $\lambda$  is the driving laser wavelength,  $a$  is the diameter of the fiber,  $\eta$  is the ratio of the number of ionized atoms to the number of initial atoms (also known as the ionization fraction),  $n_2$  is the refractive index at the driving wavelength per atmosphere,  $n_a$  is the number density of atoms,  $\Delta\delta$  is the difference in the index of refraction between the driving laser and the harmonics per atmosphere of gas, and  $r_e$  is the classical electron radius. To achieve phase-matching, the three terms in Eq. 3.15 must be balanced. In practice, this means careful selection of the waveguide diameter, the driving laser intensity (which will change the ionization fraction  $\eta$ ) and the driving wavelength ( $\lambda$ ). Furthermore, the gas pressure must be carefully optimized to allow the second and third terms to balance with the first. The first term is called the geometric term as it comes from the waveguide

geometry. The second term comes from neutral atom dispersion and the third term comes from the free electron plasma. Phase-matching is only possible if a critical ionization level is not exceeded, beyond that, no pressure will effectively balance all three terms.

The critical ionization level is calculated by setting the second term equal to the third term and solving for  $\eta$ . This determines the critical ionization because if the second and third terms are equal, then no pressure  $P$  will fix the phase mismatch. The critical ionization level is as follows:

$$\eta_c = \left[ 1 + \frac{n_a r_e \lambda^2}{2\pi \Delta \delta} \right]^{-1}. \quad (3.16)$$

Note that  $n_2$  is small and is most often neglected in the critical ionization calculation.

Lighter noble gases, e.g. *He* and *Ne*, produce the highest energy harmonics. This is because they have the largest ionization potentials and can, therefore, be driven with greater laser intensities without exceeding critical ionization.

One of the biggest advantages of HHG sources for time-resolved measurements (compared to synchrotrons or XFELs) is that the same laser can be used to generate both the pump and probe pulses. This means that there is no timing jitter between the two pulses. Therefore, the time resolution of HHG techniques is generally superior. Furthermore, because HHG produces a comb of different energies, absorption edges of different elements can be probed simultaneously. XFEL and synchrotron measurements generally require separate sequential measurements at different energies. This means that HHG measurements can avoid issues that come with trying to determine a common time-zero between measurements of different elements. For example, HHG TMOKE measurements on *FeNi* alloys identified a delay in demagnetization of *Ni* relative to *Fe*[84]. Conversely, initial XMCD taken at the BESSY II Femtoslicing facility (synchrotron) reported no delay[85]. However, in a follow-up study at BESSY II, where an x-ray-optical-correlator was used as a unique time reference, the delay that was measured with HHG TMOKE was confirmed[86].

### 3.3 Beamline Design

Time-resolved TMOKE measurements were performed at the X-MATTER beamline, Fig. 3.4. The design is described in Johnsen *et al.*[87]. The X-MATTER beamline uses neon based HHG in a semi-infinite gas cell to generate probing photons in an energy range of 40- 72 eV. This energy range is ideal for measuring the *M*-edge of magnetic 3d transition metals. 50 fs,  $\sim 800$  nm pulses with energies of up to 4 mJ, at 5 kHz, are generated using a Ti:Sapphire regenerative amplifier (KMLabs Wyvern-1000) seeded by a Ti:Sapphire oscillator (KMLabs Griffin-5). Pump and probe pulses are separated using a beamsplitter and measurements are made stroboscopically. The pump delay is controlled using a retro-reflecting mirror mounted on a computer controlled delay stage. The sample is magnetized using a projection-field electromagnet. A large portion of the beamline is kept under vacuum (1e-4 Torr or less) to prevent absorption of EUV photons by air, oxidation of the sample, and the formation of ice on EUV CCD detectors cooled to -60 °C. Piezo-actuated mirrors are used to stabilize the beam pointing.

Due to the extremely nonlinear nature of the HHG process, the HHG flux is very susceptible to fluctuations. Small changes in air currents; laser pulse energy or duration; or gas cell pressure can have large effects on the instantaneous HHG flux. The X-MATTER beamline is designed to monitor source noise and cancel it using a post-processing algorithm, Fig. 3.5. With this source noise monitoring scheme, shot-noise limited measurements have been achieved[87]. This has allowed measurements to be made with an unprecedented level of sensitivity.

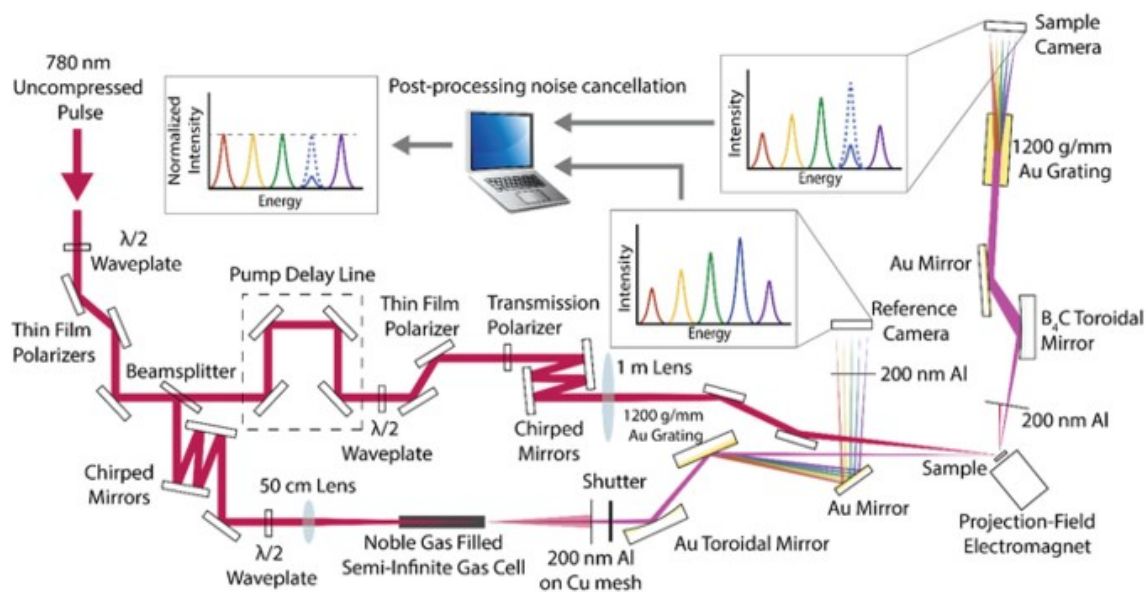
### 3.4 Conclusion

This chapter provided an overview of the physics of magneto-optic techniques with a particular emphasis on their applications for studying ultrafast processes. A brief overview of high harmonic generation is given, a technique that brings coherent EUV and x-ray photons to the tabletop. The X-MATTER beamline utilizes HHG to achieve shot-noise limited EUV TMOKE spectroscopy of magnetic materials with excellent time and energy resolution. Without this cutting-edge equipment,

Figure 3.4: A photo of the X-MATTER beamline.



Figure 3.5: **The layout of optics in the X-MATTER beamline.** Reproduced from [87], with the permission of AIP publishing. Source noise is monitored on the reference camera and digitally canceled using a post-processing algorithm.



the measurements and insights in the coming chapters would not have been possible.

## Chapter 4

### Ultrafast Magnetization Dynamics in Heusler Systems

Developing the next generation of spintronic devices will require a new level of manipulation of complex materials and their spin states at short timescales. However, fully exploiting these capabilities for more energy-efficient nanotechnologies requires a detailed understanding of the physical mechanisms underlying nanoscale spin manipulation[88]. The interaction of ultrafast laser pulses with magnetic materials can induce complex spin dynamics, both during and after the laser pulse[7, 89, 44]. When combined with ultrafast extreme UV and soft X-ray probes, it is possible to detect element-specific spin dynamics in multi-component magnetic systems[90, 91], providing rich new information not accessible using visible light. Initial studies of laser-induced spin manipulation assumed that changes to the magnetic state were a secondary process triggered by an initial hot electron distribution. In this hot electron model, electrons first absorb laser photons during a femtosecond laser excitation pulse. This is followed by electron-phonon mediated spin-flips and other scattering processes to absorb the angular momentum and demagnetize the sample on timescales of approximately 0.5 ps[17] or longer.

More recent studies that probe the instantaneous magnetization of different elements have shown that much faster manipulations of spins are possible using light, on femtosecond and even attosecond timescales. In one finding[63], a new transient magnetic state was observed in laser-excited Ni, where a magnetic phase transition is launched within a laser pulse ( $<20$  fs), provided the electron temperature exceeds the Curie temperature,  $T_C$ . In a second finding[92, 93], light-induced spin transfer within the laser pulse duration was observed between two elements in the same material

(i.e. intersite). This intersite spin transfer behavior was predicted theoretically[94, 95] and observed experimentally in Heusler compounds[92, 95] and ferromagnetic alloys[93, 96]. Nevertheless, several unanswered questions about the underlying microscopic processes remain: what constitutes a clear signature of intersite spin transfer, and how do we distinguish it from other ultrafast effects such as spin-flips, electron redistribution and demagnetization?

The aim of this chapter is to use an energy tuneable HHG probe to understand how the signatures of spin-transfer effects manifest across the  $M$ -edges of the magnetic sublattices. This will allow us to understand the strength and signature of spin-transfer effects, as well as how they can be maximized. In this chapter, I study two Heusler materials which are predicted to have large intersite spin-transfer effects:  $Co_2MnGe$  and  $Co_2MnGa$ . Heuslers are a popular material for spin-transfer studies because they often have multiple magnetic sublattices and can have interesting band structure features such as half-metallicity[95]. The half-metallicity of the  $Co_2MnGe$  and  $Co_2MnGa$  samples strongly impacts the excited spin lifetimes as well as the available pathways for electronic excitations. The Heusler compound  $Co_2MnGe$  was previously measured in our research group by Tengdin *et al.*[92] and a spin-transfer based enhancement of the  $Co$  magnetization was identified. However, at the  $Co$ -edge, only one energy was probed. This provided a somewhat limited insight into the material's dynamics. The previous study on  $Co_2MnGe$  is the motivation for this chapter where we remeasure  $Co_2MnGe$  with unprecedented energy resolution, fluence-dependence and then compare the results with state-of-the-art theory calculations utilizing time-dependent density functional theory (TD-DFT). Furthermore, we perform a detailed study of a very high quality  $Co_2MnGa$  sample to understand the effect of removing an electron from the unit cell as compared to  $Co_2MnGe$ . In the  $Co_2MnGa$  sample, we achieved excellent agreement between theory and experiment providing insight into the underlying ultrafast mechanisms. To help elucidate the comparison of  $Co_2MnGa$  and  $Co_2MnGe$ , we also performed a study of a pure  $Co$  sample. The pure  $Co$  sample has many available pathways for excitation in the minority spin channel- a feature it shares with the two Heuslers samples. However, unlike the Heuslers, it is a pure element, and so it exhibits no intersite spin-transfer effect. Furthermore, unlike the half-metallic Heuslers, pure  $Co$  is fully metallic so we

can expect very different spin-lifetimes in the minority channel.

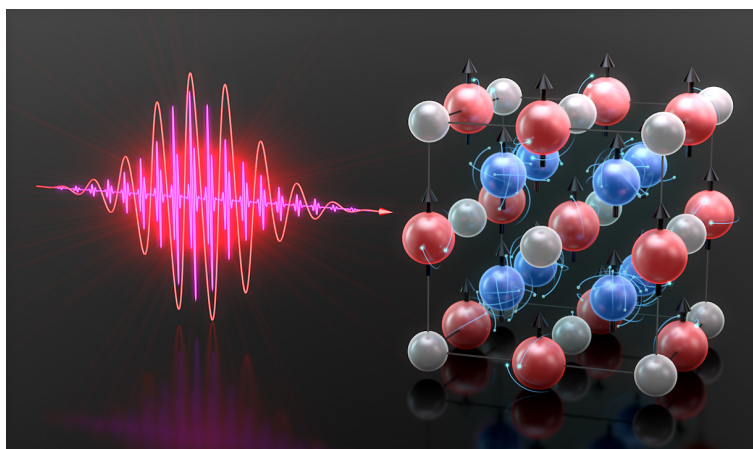
This chapter begins with two introductory sections: the first is an introduction to Heusler materials and the second in an introduction to the optical intersite spin transfer effect (OISTR). Following the introductory sections, the first half of this chapter is an extensive experimental and theoretical study of the Heusler alloy  $Co_2MnGa$ . The content of this section is adapted from Ryan *et al.*[97]. We present the first time- and energy-resolved TMOKE measurements of this material. In this section, we will disentangle the competing effects of intrasite and intersite spin transfers as well as laser-induced demagnetization. We will make the first fluence-dependent measurements of the OISTR effects and present the most extensive energy and time resolved measurements of spin transfer in any material to date. The second half of this chapter is a yet unpublished expansion of the  $Co_2MnGa$  study where the transient MOKE signal of  $Co_2MnGa$  is directly compared to  $Co_2MnGe$  as well as a pure  $Co$  sample. This section also contains extensive energy- and time-resolved measurements as well as fluence-dependent results. We discover an important difference between measuring the spin-transfer signature in conductors vs. half-metals. We also note a region of MOKE enhancement near the zero-crossing in all three materials. This signature may be misinterpreted as an OISTR enhancement but most likely has other origins.

Time-dependent density functional theory (TD-DFT) calculations are presented throughout this chapter to compliment experimental measurements. Extensive details of the theoretical framework used in the TD-DFT calculations appear in our paper published on  $Co_2MnGa$ [97]. The theoretical framework section of the paper was written by Mohamed Elhanoty who performed the TD-DFT calculations for this chapter.

## 4.1 Introduction to Heuslers

Heuslers are a group of ordered magnetic compounds with a chemical formula of  $X_2YZ$  for full Heuslers, or  $XYZ$  for half-Heuslers[98]. This class of compounds is particularly exciting as it supports a wide range of materials with excellent chemical stability, and with electronic and magnetic properties that can be engineered based on the number of valence electrons of the constituent

Figure 4.1: **Graphic of ultrafast laser excitation and high harmonic probing of the spin system in a Heusler compound.** Image designed by Steve Burrows for the press release of Ryan *et al.*[97].



elements[99]. Heusler compounds host a number of remarkable ground states that include topological insulators[100, 101, 102, 103], half-metals[104] and superconductors[105, 106], and are promising candidates for technological applications such as thermoelectric[107, 108, 109, 110] and spintronic devices[111, 112, 113, 114, 115]. The magneto-optical properties of Heuslers have been of great interest for the past 40 years following the measurement of the largest visible Magneto-Optical Kerr Effect (MOKE) signal on MnPtSb in 1983[116]. In addition, half-metallicity (where one spin channel is gapped at the Fermi level while the other is partially filled and hence conducting) was first detected in a Heusler material[117], and recent investigations have identified non-quasiparticle states in a Heusler metal[118]. More specifically for the present investigation, Heuslers have been the focus of many ultrafast magnetism studies. Furthermore, the half-metallicity can lead to unique responses to optical pumping since the available excitation channels are spin selective[119]. The ultrafast MOKE responses of Heuslers and other half-metals were first demonstrated using visible probes[95, 120, 121, 122].

## 4.2 Introduction to OISTR

It was recently predicted that optical spin pumping from one metallic sublattice to a second sublattice can transiently enhance the magnetic moment of the second metallic sublattice within the laser pump pulse[94, 119], in a process often called optical intersite spin transfer (OISTR). Since the origin of the OISTR effect is optical excitation from occupied to unoccupied states, this presents the potential for few-femtosecond optical manipulation of spin states. Moreover, it might be expected that OISTR has a particularly strong signatures in Heusler compounds because of their unique band structure[119].

Experimentally, OISTR was previously investigated using visible MOKE in Heuslers[95], followed by measurements with element-specific extreme ultraviolet (EUV) high harmonic probes in the Heusler compound  $Co_2MnGe$ [92] as well as  $FeNi$  alloys[93]. These initial experiments were followed by  $L$ -edge measurements indicating transient ferromagnetism in an antiferromagnet[123]. However, in all of these studies, the OISTR-like enhancement was only observed at one specific

probing energy, and the corresponding absorption edge was only probed at one[92, 123] or two[93] energies. In other studies, OISTR was inferred from the respective demagnetization rates of *Co* and *Pt* in a *CoPt* alloy[96] or *Ni* in a stack of *Ni/Pt* multilayers[124]. However, in both of these cases no enhancements of the magnetic circular dichroism (MCD) were predicted or observed.

OISTR is not the only effect that can cause a transient enhancement in the magneto-optical signal. When a femtosecond laser pulse excites a material, the electron population is redistributed during and after the pulse. This can lead to shifts and broadening of absorption edges on the same timescales as the laser pump pulse. These effects have been observed in experimental studies of *Ni* at the *M*-edge using circular dichroism[125, 126] and transient absorption spectroscopy[127, 128, 8], as well as theoretical works studying *Ni*[129] with circular dichroism at the *L*-edge. These effects can lead to signatures that appear as transient enhancements in the MOKE or circular dichroism signal at specific probe energies – despite the fact that there is no overall increase in magnetization of the sample[125]. Another study[130] showed vastly different *Co* demagnetization rates above and below the *Co L*-edge in a [*Co/Pd*] multilayer structure which were attributed to energy-dependent spin-flip rates. Thus, it is critical to implement unambiguous measurements and combine with theory in order to capture the true signature of OISTR and distinguish it from local changes in the magneto-optical signal due to charge redistribution or spin-flips. We show below that this can be achieved by measuring the magnetic asymmetry across the full absorption edges on the two magnetic sublattices involved in the intersite spin transfer, and then comparing the measurements to the static and transient asymmetry from TD-DFT.

### 4.3 *Co<sub>2</sub>MnGa*

Here we address the challenges of detecting OISTR signatures by combining the element-specificity of extreme ultraviolet (EUV) high harmonic probes with time-dependent density functional theory (TD-DFT) and detect a definitive signature of light-induced intersite transfer of spin polarization in a Heusler compound *Co<sub>2</sub>MnGa*. This material can be grown in a highly-crystalline phase with a half-metallic bandgap (Fig. 4.2(c)) and thus might be expected to support a strong optical

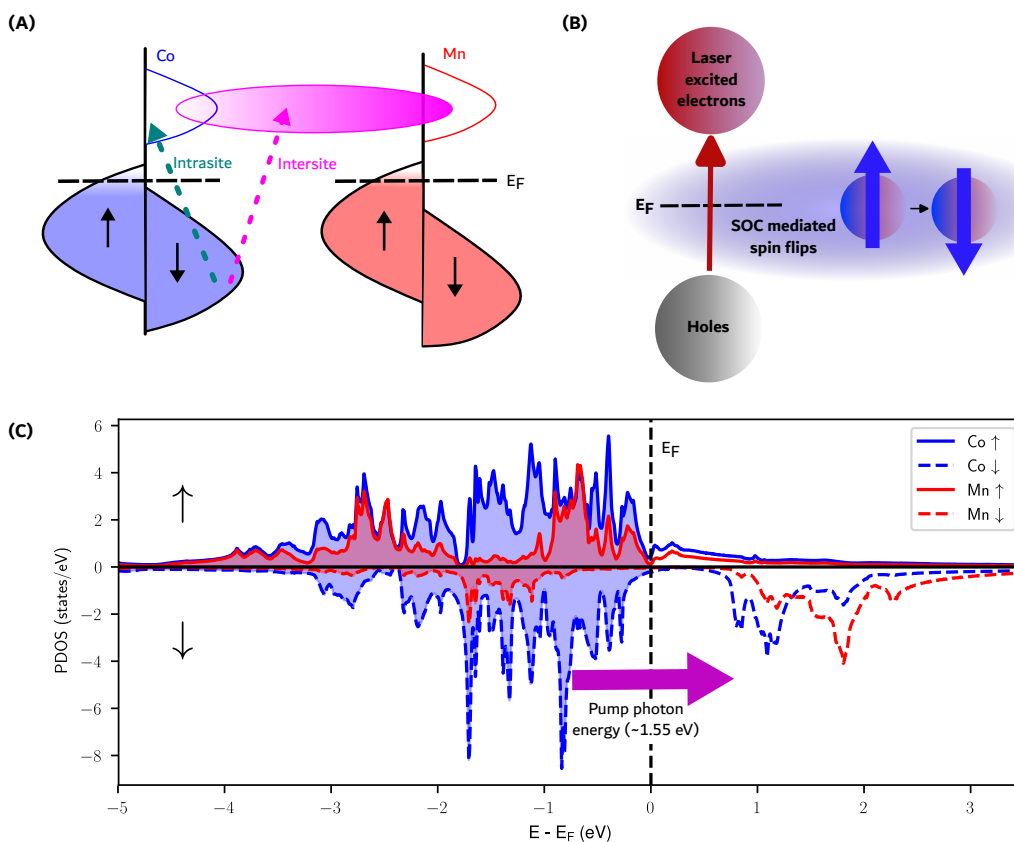
intersite spin transfer effect[119]. We observe very strong enhancements of the magneto-optical signal across the entire  $M$ -edge due to light-induced spin transfer - a behavior never observed in any material to date. To identify specific excitation pathways, one needs to distinguish how same-site spin transfer, intersite transfer and ultrafast spin-flips mediated by spin-orbit coupling respectively change the magnetic moments of  $Mn$  and  $Co$ , and how these processes manifest themselves in the transient EUV magneto-optic signal. To achieve this goal, we scan the energy of an EUV probe in order to measure the spin dynamics across the entire  $M$ -edges of the two magnetic sublattices involved. Then, by comparing experimental observations with theory based on TD-DFT, we uncover the relative dominance of same-site  $Co - Co$  spin transfer (Fig. 4.2(a)), intersite  $Co - Mn$  transfer (Fig. 4.2(a)), and ultrafast spin-flips mediated by spin-orbit coupling (Fig. 4.2(b)). Moreover, the contributions from these different processes to the light-induced spin manipulation change as a function of time and laser intensity. Although theoretical studies have predicted the fluence dependence of intersite spin transfer[94, 131], no experimental studies have been published to date. By changing the pump fluence and probe energy, we show that one can both identify and tune the competing microscopic mechanisms underlying light-induced spin manipulation on ultrafast timescales ( $<100$  fs). The combination of detailed theoretical insight, excellent sample quality, and an extensive experimental data has allowed us to demonstrate side-by-side theoretical and experimental comparisons of ultrafast spin dynamics in complex magnetic alloys.

### 4.3.1 Results for $Co_2MnGa$

Measurements were made using the X-MATTER beamline[87] in Boulder on a 20 nm-thick epitaxial  $Co_2MnGa$  film (see Ryan *et al.*[97] for sample growth techniques). A 40-55 fs,  $\sim 800$  nm laser pump pulse is used to excite the sample. The resulting dynamics were probed using extreme ultraviolet (EUV) light generated through high harmonic generation (HHG), with a pulse duration of  $\sim 25$  fs. The transverse magneto-optical Kerr effect (TMOKE) is used to probe the magnetic asymmetry. See Fig. 4.2 in the supplementary figures (Section 4.3.4) for a schematic.

In Fig. 4.3, we present the full energy resolved  $Co_2MnGa$  asymmetry in both experiment

Figure 4.2: **The three excitation types included in the theoretical calculations, and the ground state density of states.** (A) Optical excitations within the same species (intrasite, green dotted line) which are predominantly  $Co - Co$  minority band excitations, as well as excitations between different species (intersite, pink dotted line). The pink shaded area indicates a final state composed of a hybridized band with predominantly  $Mn$  character. (B) A spin-flip mediated by spin-orbit coupling (SOC) that is induced by the laser-excited non-equilibrium charge distribution. Such spin-flips contribute to demagnetization. (C) Calculated  $d$ -shell density of states and their population (PDOS) with spin and element specificity. PDOS in an occupation weighted projected density of states as outlined in the Materials and Methods section. The black dotted line is the Fermi Energy ( $E_F$ ). The y-axis is divided into two, with the positive axis containing majority spin states and the negative axis containing minority spin states (signified with black arrows, representing spin direction). The energy of the pump laser's photons is represented with a pink arrow.  $Ga$  atoms contribute very few states near the Fermi energy (not shown).

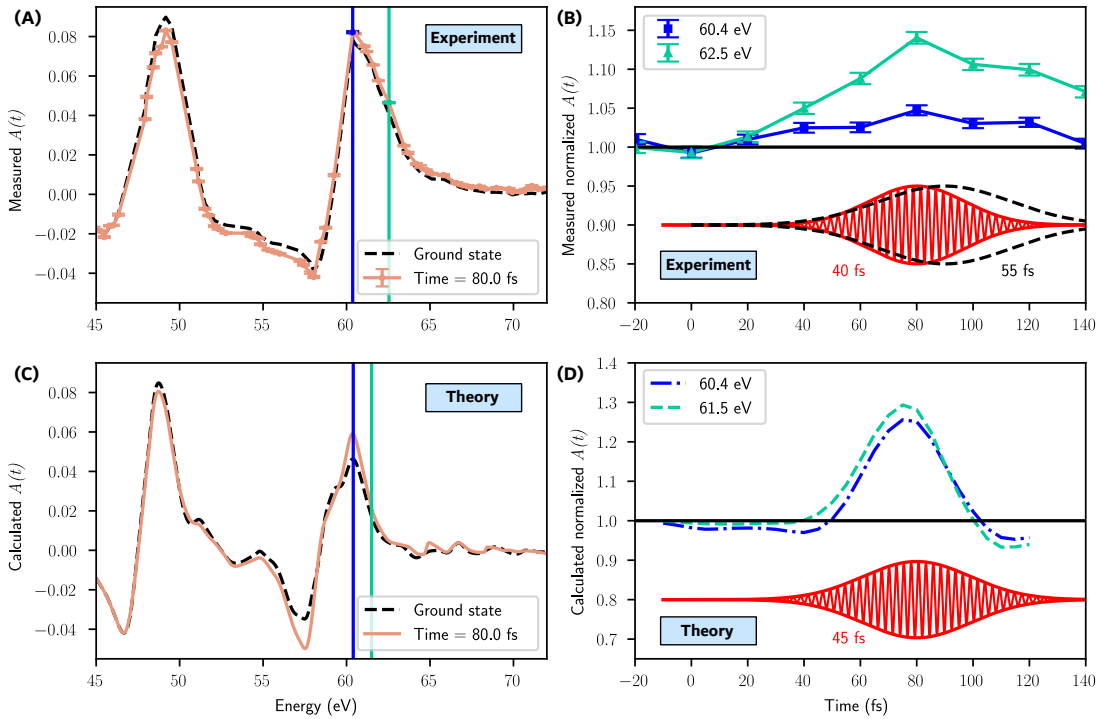


and theory. An incident fluence of  $3.4 \text{ mJ/cm}^2$  is used corresponding to an absorbed fluence of  $2.2 \text{ mJ/cm}^2$ . This absorbed fluence value ( $2.2 \text{ mJ/cm}^2$ ) was used in the TD-DFT calculations. We measure and model the changes following laser excitation to determine how excitations manifest themselves across the *Mn* and *Co* *M*-edges. These results are shown in Figs. 4.3(b) and (c), where we plot the experimental and theoretical asymmetries in the ground state as well as at  $80 \text{ fs}$  following laser excitation.

The magnetic asymmetry at the *Mn* *M*-edge peak resonance ( $\sim 47\text{-}51 \text{ eV}$ ) shows a transient reduction in the TMOKE signal, as shown in Fig. 4.3(a). Experimental data which include more time points for *Mn* energies are available in the supplementary figures Section 4.3.4, Fig. 4.7. Given the density of states of *Co*<sub>2</sub>*MnGa* (Fig. 4.2(c)), and our excitation photon energy of  $\sim 1.55 \text{ eV}$ , we attribute the transient reduction of the *Mn* TMOKE signal to ultrafast demagnetization processes as well as the transfer of minority band electrons from *Co*, both of which reduce the spin polarization of *Mn*. The transient reduction at the *Mn*-edge at  $80 \text{ fs}$  is also reproduced in the calculations shown in Fig. 4.3(c), where it can be seen that the experiment and theory agree very well, both for the static ground state as well as for the driven system. The calculations based on TD-DFT demonstrate ultrafast demagnetization by spin-flips driven by the spin-orbit coupling (SOC)[56]. SOC mixes the spin states so that spin is no longer a pure quantum number[132]. Unlike dipole excitations, spin-flip transitions do not conserve the total magnetization of the sample and will have a net demagnetizing effect.

The TMOKE asymmetry signal is strongest when the probe is resonant with the energy difference between the  $3p$  core states and the Fermi energy. For this reason, the signals at the *Co* and *Mn* peaks predominantly arise from excitations to valence states which are in the close vicinity of the Fermi energy. Across the *Co*-edge ( $\sim 57\text{-}72 \text{ eV}$ ), we observe a transient enhancement. However, the size of the enhancement depends strongly on the probing EUV photon energy, as shown in Fig. 4.3(b). The pump-induced changes at two different energies (at the *M*-edge, and above the edge) display maximal enhancements of approximately 5% and 14%, respectively. The changes in the TD-DFT calculated asymmetry at similar energy regions reveal a similar trend, as shown in Fig.

Figure 4.3: **Experimental and theoretical magnetic asymmetries.** (A) The experimentally measured asymmetry in the ground state and at 80 fs following a  $2.2 \text{ mJ/cm}^2$  laser excitation. (B) The measured transient asymmetry signals at selected energies (marked with colored vertical lines in A) normalized by their ground state values. A depiction of the experimental pump pulse appears below the data with an arbitrary vertical scaling. The experimental pulse is represented as an oscillating electric field with a full width half maximum (FWHM) that was measured to range from 40-55 fs. (C) The theoretically calculated asymmetry in the ground state and at 80 fs. (D) The simulated transient asymmetry signals at selected energies (marked with colored vertical lines in C) normalized by their ground state values. To simulate the measurement probe, the theoretical dynamics were convolved with the intensity profile corresponding to a 25 fs FWHM Gaussian electric field envelope. The unconvolved data appear in the supplementary figures (Fig. 4.13). The theoretically modeled pump electric field, 45 fs FWHM, appears below the data with an arbitrary vertical scaling.

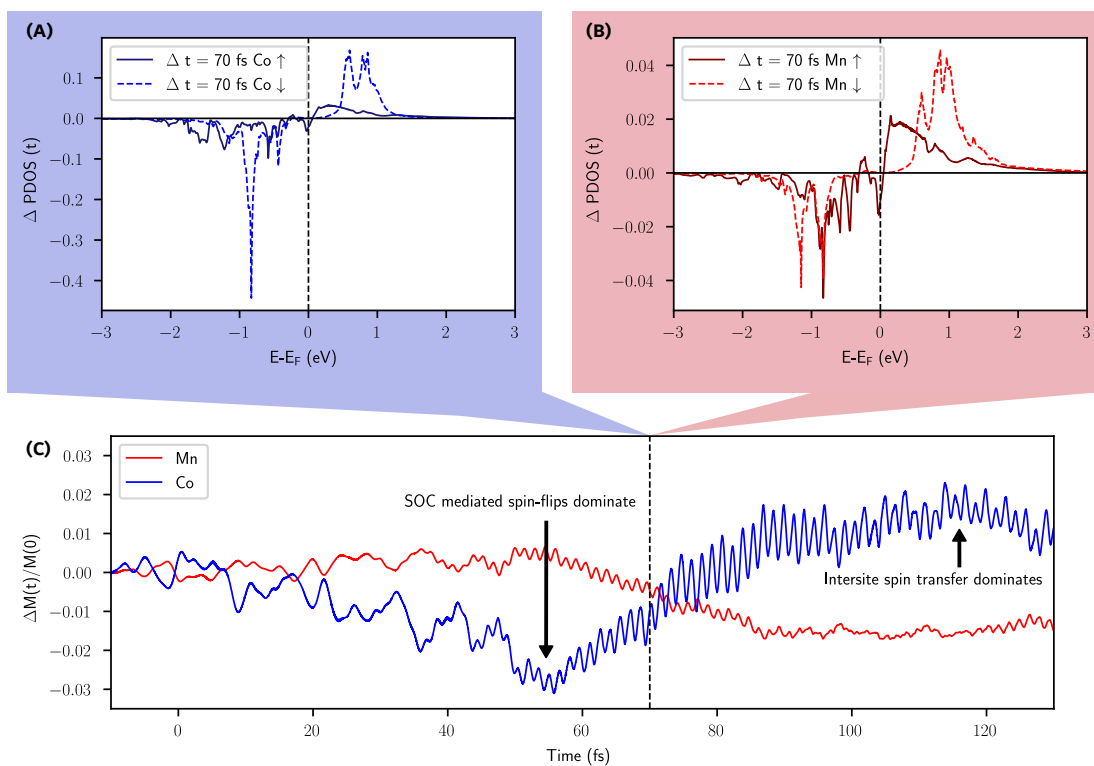


4.3(d). Indeed, the experimental and theoretical data that can be compared in Figs. 4.3(b) and (d) demonstrate very similar features, both when it comes to the time- and energy dependence of the transient optical asymmetry, as well as the general shape of the measured and calculated data. The different strengths of enhancements at different probing energies can be understood by considering that there is strong optical pumping that moves spin-polarized electrons in *Co* from lower to higher energy bands. The transient *Co* signal at any given energy is sensitive to this redistribution of the electron population, despite the fact that the overall spin polarization of *Co* is unchanged by these intraspecies (same-site) optical excitations. Furthermore, the strength of the demagnetizing spin-flips is also energy-dependent. The strongest spin-flip excitation occurs near the peak of the signal (60.4 eV) as will be discussed in more detail below.

We note that although Fig. 4.3(d) depicts theoretical transient enhancements close to 30% at 61.5 eV, the calculated change in the *Co* moment is only 2.5%, as shown in Fig. 4.4(c). It is clear that the small change in the *Co* magnetic moment is not the only process influencing the energy-dependent transient EUV TMOKE signals. It is noteworthy that the present investigation is the first to measure an OISTR effect across two entire absorption edges (*Co* and *Mn*), which allows for a much deeper analysis compared to studies with a limited number of energy probes[92, 93, 123]. This allows us to conclude that the measured transient enhancement of the magnetic asymmetry signal is extremely energy-dependent and can be large at specific probing energies. For example, near the zero-crossing of the *Co* asymmetry (59.3 eV), the magnitude of the signal is very sensitive to changes in the asymmetry shape, and an enhancement of greater than 100% is observed. Similarly, probing at 71.5 eV where the energy is far above the *Co* peak and the absolute signal is small, one may observe transient enhancements in the signal of over 2000%, see Fig. 4.8 in the supplementary figures (Section 4.3.4).

The pump pulse controls the OISTR effect[131] by modifying the electron population around the Fermi energy. This modification spans an energy range of approximately twice the pump photon energy (or  $\sim 3.1$  eV). To understand the potential OISTR effects within the sample, we analyze the available states above and below the Fermi energy. Fig. 4.2(c) displays the ground state density

Figure 4.4: **Theory calculations for pump induced excitations of *Co* and *Mn*.** (A) The energy-dependent and spin-specific change in the *Co* occupation 70 *fs* after laser excitation. The calculation of the occupation weighted projected density of states (PDOS) is explained in the theoretical framework section of Ryan *et al.*[97]. A negative value signifies a depletion of electrons compared with the ground state and a positive value signifies an increase. (B) The same treatment is applied to *Mn*. Note the difference in scale for the *Co* and *Mn* PDOS. (C) The transient change in the total magnetic moments of *Co* and *Mn* following laser excitation. This is calculated by integrating the change in spin polarization across all energies shown in subfigures A and B. Initially, the response of *Co* is dominated by spin orbit mediated spin-flips. This is followed by a dominance of intersite spin transfer.



of states (DOS) of  $Co_2MnGa$ , where one can identify the insulating gap in the spin down channel that gives rise to the half-metallic character. Below the Fermi energy,  $3d$ -shell minority spins in  $Co$  provide more occupied electronic states available for pump excitation than states in  $Mn$ . In contrast,  $Mn$  has more available unoccupied states just above the Fermi energy. The probabilities of individual transitions come from the dipole transitions accessible by the pump laser, as analyzed in detail in Ref. [92]. The TD-DFT calculations access these excitations by solving the time-dependent Kohn-Sham Hamiltonian, see theoretical framework section in Ryan *et al.*[97]. Based on the excitations and depletions shown in Figs. 4.4(a) and (b), that are analyzed in detail below, we infer that excitations from  $Co$  minority states to  $Mn$  minority states are more probable than other types of interspecies excitations.

Moving minority spins from  $Co$  to  $Mn$  leads to an enhancement of the  $Co$  magnetization accompanied by a simultaneous reduction in the  $Mn$  magnetization. This is consistent with the asymmetry changes measured and modeled in Figs. 4.3(a) and (c) as well as the changes in magnetic moment simulated in Fig. 4.4(c).

The origin of the transient changes in the theoretical and experimental magnetic asymmetry curves can be understood through the changes in the occupation of the  $3d$  states as depicted in Fig. 4.4. In Figs. 4.4(a) and (b), we show a snapshot of the changes in the energy resolved majority and minority spin occupations for the  $3d$  states at  $70 fs$  for  $Co$  and  $Mn$ , respectively. This figure should be interpreted as follows: a negative signal below the Fermi level indicates a depletion of electron states at the corresponding energy, while a positive signal above the Fermi level indicates the occupation of electron states that were empty in the ground state. As the figure shows, some of the occupied majority and minority spin states below the Fermi level become depleted. In addition, the previously empty states in the minority and majority spin channels above the ground state Fermi energy become partially filled.

Several processes contribute to the behavior seen in Fig. 4.4:  $Co - Co$  spin pumping during the pump pulse,  $Co - Mn$  spin pumping during the pump pulse, and spin-flip excitations which exist both during and after the pulse excitation. The largest occupation increases and depletions are

seen in the *Co* minority channel. From this we infer that *Co* – *Co* minority spin pumping is strong. The quantity of *Mn* – *Mn* and *Mn* – *Co* transitions is low due to a lack of available initial and final states with an appropriate energy separation that would be accessible to the laser pump pulse, as shown in Fig. 4.2(c). By integrating the total change in spin polarization across all energies (Figs. 4.4(a) and (b)) we obtain the net change in moment for each element (Fig. 4.4(c)). The magnetic moment of *Co* is maximally increased by 2.5% while the *Mn* moment simultaneously decreases by 2%. The theory predicts a transient reduction in the total number of *Co* minority spins accompanied by an increase in *Mn* minority spins. Therefore, we infer that the main OISTR pathway in this material is *Co* to *Mn* minority spin pumping. The calculated ground state moments for this sample are  $2.72 \mu_B$  per *Mn* atom,  $0.77 \mu_B$  per *Co* atom,  $0.06 \mu_B$  per *Ga* atom and an interstitial moment (not associated with any specific element) of  $-0.04 \mu_B$  per unit cell. We note that while there are twice as many *Co* atoms as *Mn* atoms, the *Mn* atoms carry a magnetic moment more than three times as large as *Co*. This means that although the calculated percentage enhancement in *Co* is larger than the corresponding percentage decrease in *Mn*, the sample exhibits a net demagnetization.

To separate the fingerprints of the SOC-mediated spin-flips and spin transfer processes in the simulated dynamics, we make use of the time-varying amplitude of the simulated laser pulse. As the strength of the laser pulse changes, the signatures of each process appear in specific time and energy windows within the TMOKE spectra. To demonstrate this, we plot the theoretical asymmetry curves at 40 *fs*, 80 *fs*, and 100 *fs*, see supplementary figures (Section 4.3.4) Fig. 4.9.

At early times (e.g., the first 50 *fs*), while the incident electric field from the pump laser is still weak, the dynamics are dominated by SOC-mediated spin-flips. The laser excites electrons from regions located around the atomic nuclei (i.e. muffin-tin regions) to the interstitial region between atoms. In the interstitial regions, electrons are more delocalized, and spin-orbit effects are weaker[56]. The excitation of electrons from the muffin tin regions to the interstitial regions creates a non-equilibrium distribution of electrons. This non-equilibrium distribution induces spin-flips in the regions with the strongest spin-orbit coupling, i.e. electrons near the Fermi energy in the muffin tin region[56, 57]. Because this effect is strongest close to the Fermi energy, the spin-flips manifest

themselves as a reduction in the intensity of the asymmetry signal, seen most strongly at the *Co* and *Mn* peaks ( $\sim 60.4$  eV and  $\sim 49$  eV). The spin-flip signature in the asymmetry peaks is apparent in times between 0 – 50 fs, see supplementary figures (Section 4.3.4) Fig. 4.9. These spin-flips account for the reduction in *Co* magnetic moment seen in Fig. 4.4(c) on the same timescale.

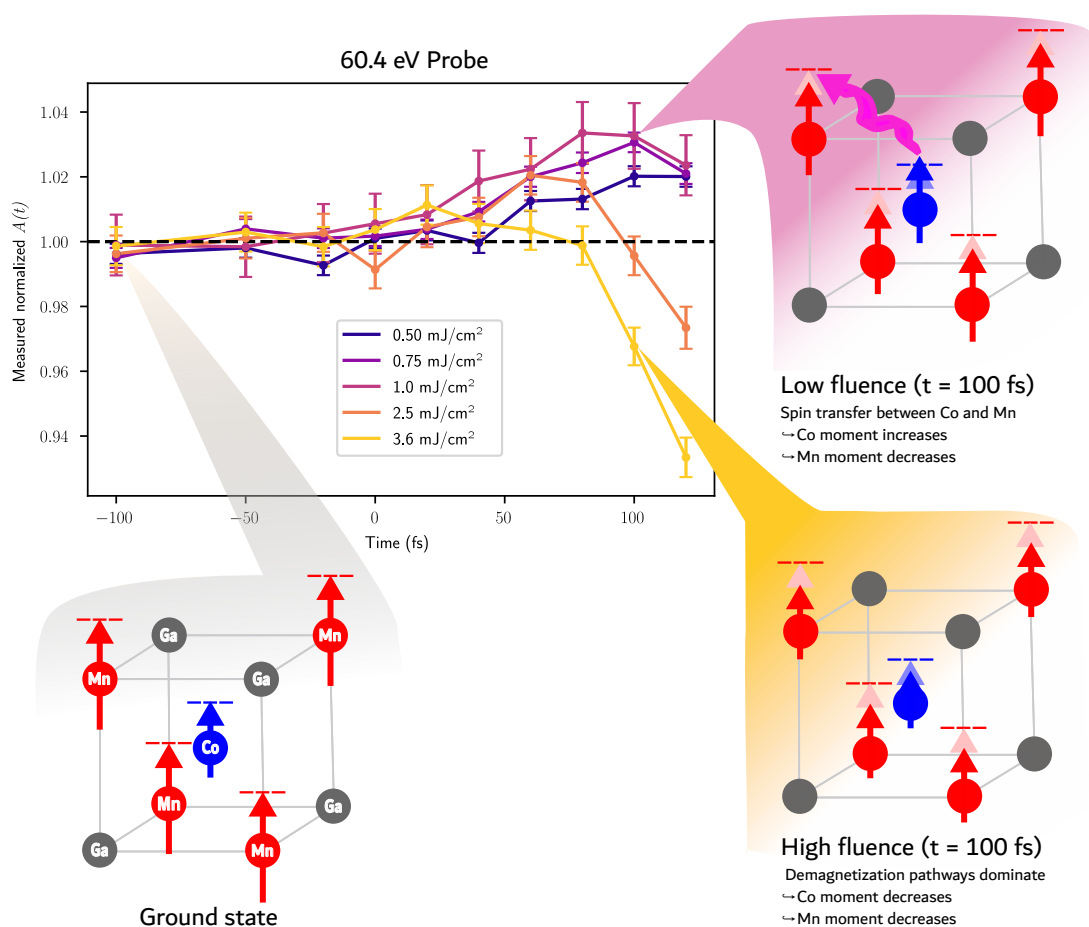
At subsequent times (50-80 fs), as the incident electric field of the pulse grows, spin transfers start to out compete the spin-flips. The spin transfers manifest themselves as an enhancement of the asymmetry across the entire *Co*-edge, and a small reduction of asymmetry at the *Mn*-edge, see supplementary figures (Section 4.3.4) Fig. 4.9. The small size of the reduction at the *Mn* peak is consistent with the small OISTR induced moment change (2.0%) as depicted in Fig. 4.4(c). Optical excitations in the spin minority channel of *Mn* are mostly suppressed due to the optical gap, as shown in Fig. 4.2(a). After the maximum of the pump laser has passed, e.g. after 80 fs (see supplementary figures (Section 4.3.4) Fig. 4.12), the calculated TMOKE spectra show a relaxation of the electrons that were excited by spin transfers, and we therefore see a decay in the asymmetry at the *Co*-edge. After the pump pulse excitation ends, spin-flips dominate once again.

The dominance of spin-flips at early timescales that is predicted by theory (shown in Fig. 4.4(c)) appears only very weakly in the experimental data of Fig. 4.3(b). This is attributed to a smearing of the response by the 25 fs EUV probe pulse. Indeed, when the theoretical data is convolved with the EUV probe pulse (as shown in Fig. 4.3(d)), we also do not observe strongly negative signals at early timescales. However, for the unconvolved data which appears in the supplementary figures (Section 4.3.4), Fig. 4.13, negative values at early times are clearly observed.

At the *Co* asymmetry peak, there is strong competition between optical excitations, OISTR, and spin-flip effects. The MOKE signal enhancement at the resonance peak is diminished in comparison with the off-resonance regions where the OISTR and optical excitations dominate, as shown in Figs. 4.3(b) and (d). This competition is experimentally exemplified in Fig. 4.5 where we show the fluence dependence at the *Co* peak (60.4 eV). These results show the first experimentally measured fluence dependence of OISTR.

Theoretical predictions[131] indicate that the strength of the OISTR effect should be propor-

Figure 4.5: **The fluence dependence of the MOKE asymmetry signal measured at the *Co* peak.** The *Co* peak is probed using 60.4 eV photons. The magnitude of the transient enhancement increases with increasing fluence up to 1.0  $mJ/cm^2$ . Above 1.0  $mJ/cm^2$  it is diminished due to competition between demagnetization pathways and OISTR effects. The listed fluences are the absorbed fluences.



tional to the fluence of the pump laser. At low fluences ( $<1.0 \text{ mJ/cm}^2$ ) at the *Co* peak, the transient enhancement of the TMOKE signal increases as the fluence increases (see Fig. 4.5). However, as the pump fluence is increased above  $1.0 \text{ mJ/cm}^2$ , the transient enhancement becomes smaller and the peak occurs at earlier times. We attribute this to the increasing dominance of demagnetization mechanisms at higher fluences – which begin to compete with, and overcome the OISTR effects. This is in contrast to the pre-edge and post-edge regions where optical excitations dominate over spin-flips, see supplementary figures (Section 4.3.4) Fig. 4.10. However, the TD-DFT calculations predict that the enhancement should continue increasing with fluence, see supplementary figures (Section 4.3.4) Fig. 4.11. For example, with an  $8.4 \text{ mJ/cm}^2$  pump fluence, an OISTR enhancement of the *Co* moment of 10% is predicted, compared to only 2.5% for a fluence of  $2.2 \text{ mJ/cm}^2$ . Thus, the theoretical model used here underestimates the strength of the demagnetizing effects at the peak. This could be due to the fact that the theory only includes spin-flips and cannot model other demagnetizing effects such as magnon generation, electron-phonon coupling or superdiffusive spin currents, all of which would increase in strength with increasing pump-fluence.

### 4.3.2 Discussion of *Co<sub>2</sub>MnGa*

An ongoing topic of debate is whether the interspecies excitations involved in OISTR are dipole allowed. We note that selection rules in solids are quite complex, as they are determined by crystal symmetries and often involve states belonging to hybridized bands that exhibit a mixed site- and angular momentum character[133]. Furthermore, published calculations of the optical properties of Heuslers do not exclude transitions between bands predominantly associated with differing species[134, 135, 136]. Moreover, in each of these cases, transitions between hybridized bands[134, 135], or bands from predominantly different species[136], are needed to recreate important features in the characteristic optical response of the material.

Due to limitations on computational power, the TD-DFT framework only simulates one unit cell of *Co<sub>2</sub>MnGa*. Therefore, spatial effects such as magnon generation, electron-phonon interactions and superdiffusive spin currents cannot be included. The only demagnetization pathway that can

be simulated is individual spin-flips mediated by spin-orbit coupling. For this reason, as discussed above, the theoretical calculations underestimate the amount of demagnetization in the sample, especially on the 100 *fs*-1 *ps* timescales where magnon generation becomes prevalent[15, 50, 137].

The transient enhancement of the TMOKE signal at the *Co* peak was quenched at lower fluences than expected. However, at other energies across the *Co*-edge this was not the case, see supplementary figures (Section 4.3.4) Fig. 4.10. We attribute this to strong demagnetization pathways at the Fermi energy, which are not included in the TD-DFT calculations. Further evidence of this is the fact that the *Mn* demagnetization signal is also underestimated by theory at all probe energies and pump fluences. The experimental data shown in Fig. 4.3 show clear and extensive qualitative agreement with the theoretical results that go well beyond what has previously been reported in the literature on this topic. Nevertheless, as noted above, there are a few areas of disagreement. For example, the pre- and post-edge regions of *Mn* differ in shape. We note that the TD-DFT simulations are, for practical reasons, limited by a few key assumptions. As mentioned above, we only had the computational power to treat one unit cell, and therefore sample imperfections are not considered. The sample is high quality, and grown in the  $L2_1$  phase. Sample growth techniques are given in Ryan *et al.*[97]. However, there are many factors that could influence the behavior of a real sample such as interfacial and thin film effects, as well as potential strain from the growth and capping layer. Furthermore, an exact form of the exchange-correlation functional is not known and must be approximated. To account for these approximations in the exchange-correlation functional, the ground state and transient TD-DFT asymmetry spectra are shifted with a rigid blue shift of 0.8 *eV* and the intensity is scaled with a factor of 1.25 to benchmark the ground state theoretical asymmetry with the experimental measurements.

The time evolution and response functions were calculated using an adiabatic approach. This means that the history and memory dependence of the dynamics were ignored. Therefore, the theoretical dynamics (Fig. 4.3(d)) are faster and more intense than the experimental dynamics (Fig. 4.3(b)). Depth dependent effects within the sample may also contribute to a slower experimental signal. Furthermore, the experimental pump pulse duration spans from 40 to 55 *fs* FWHM compared

with the theoretically simulated value of 45 *fs* FWHM. This is because the experimental pulse duration of the laser changes as we tune the central wavelength in order to scan the EUV photon energy across the *M*-edges.

Most importantly, we have shown here that a simplistic interpretation of the pump-induced changes in the magnetic asymmetry as a change in the magnetic moment is not correct, since same-species optical excitations lead to energy-dependent changes in the asymmetry curve. Fig. 4.3 shows that the transient enhancement of the TMOKE signal at the *Co*-edge (both theoretically and experimentally) varies strongly with probing energy. For example, a 5% transient enhancement is measured at 60.4 *eV* (on resonance) compared with a 14% enhancement measured at 62.5 *eV* (above edge), as shown in Fig. 4.3(b).

*Co<sub>2</sub>MnGa* has been of particular interest in recent experimental and theoretical studies[138, 139, 140, 141, 142, 143] due to its topologically non-trivial band structure. Specifically, *Co<sub>2</sub>MnGa* exhibits topological Weyl fermion lines and drumhead surface states[138]. There has been a recent discussion of the need for ultrafast studies of topological materials[144]. Measuring transient behaviors could help to characterize and control nodal structures. However, due to the large energy of the exciting laser photons in the experiments presented here ( $\sim 1.55$  *eV*), we do not have an effective scheme to sensitively measure behavior at Weyl points. In the future, a pump with a lower photon energy could confine more excited electrons within the Weyl points. This could give more insight into the effects of topology and surface states on ultrafast dynamics. Although the topological effects in *Co<sub>2</sub>MnGa* are not addressed in the theoretical analysis in this paper, this work will serve as an important foundation for future ultrafast studies examining the topological nature of this material, and similar systems.

### 4.3.3 Conclusion

In conclusion, by implementing ultrafast EUV TMOKE at many probing energies across the density of states of *Co<sub>2</sub>MnGa* and comparing with TD-DFT, we have established a unified experimental and theoretical framework for understanding complex light-induced spin dynamics on

very short timescales ( $<100$  fs). A prominent finding of this investigation is that the pump-induced change of the asymmetry of the EUV TMOKE signal can vary substantially from the changes of the magnetic moment. In addition, we have distinguished intrasite, intersite and spin-flip contributions to the transient TMOKE signal and their implications on the interpretation of the transient signal. We have also made the first fluence-dependent measurements of spin transfer effects and observe that the resonant enhancements of  $Co$  are maximized at surprisingly low fluences ( $1.0$  mJ/cm<sup>2</sup>). The differing fluence- and energy-dependent behaviors across the  $Co$ -edge demonstrate that experiments claiming to observe OISTR need to probe across the entire edge to disentangle the contribution of different microscopic processes to the magnetic asymmetry. Our extensive experiment and theory datasets have allowed us to identify key regions of theoretical and experimental agreement along with areas for future improvement. The theoretical simulations and experimental measurements jointly demonstrate large energy-dependent spin transfer signals. Thus, this work sets a high standard for theoretical and experimental agreements for ultrafast spin dynamics in alloys and provides insight into competing microscopic mechanisms.

#### 4.3.4 Supplemental Figures

This section contains Figs. 4.6 to 4.13 which supplement the findings of Section 4.3.

Figure 4.6: **Experimental design.** The magnetized sample is excited with a near-IR pump pulse followed by an EUV probe pulse after a time delay  $\Delta t$ . The EUV probe contains a comb of energies produced by high harmonic generation. The harmonic comb is spectrally dispersed using a diffraction grating then detected with a CCD camera. Different harmonic energies are resonant with the  $M$ -edges of  $Mn$  and  $Co$ . TMOKE measurements are made by comparing the intensity of light reflected from the sample with two different sample magnetization directions (up and down) as shown in the figure.

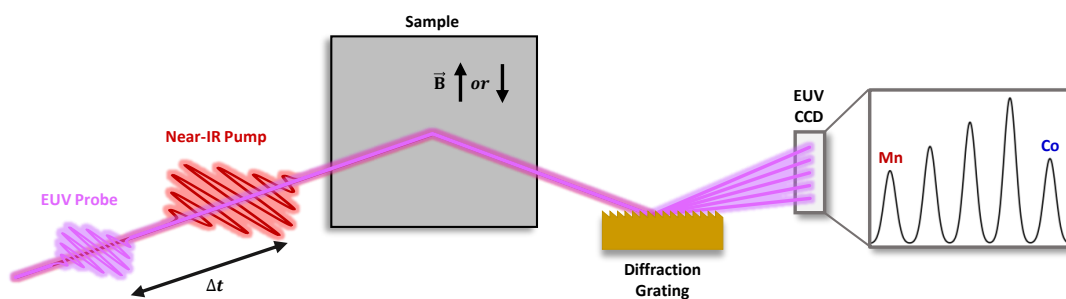


Figure 4.7: **Energy-dependent transient magnetic asymmetry with probing energies from 44.9 eV to 58.0 eV.** The absorbed pump fluence is  $2.2 \text{ mJ/cm}^2$ . The peak of the *Mn* asymmetry occurs at 49.2 eV. The probing energy region from 51.5 eV to 55.0 eV lies between the *Co* and *Mn* edges. Signals at these probing energies see a combination of high energy *Mn* states as well as low energy *Co* states. We do not draw any conclusions from the enhancements seen in this region due to their strongly mixed nature.

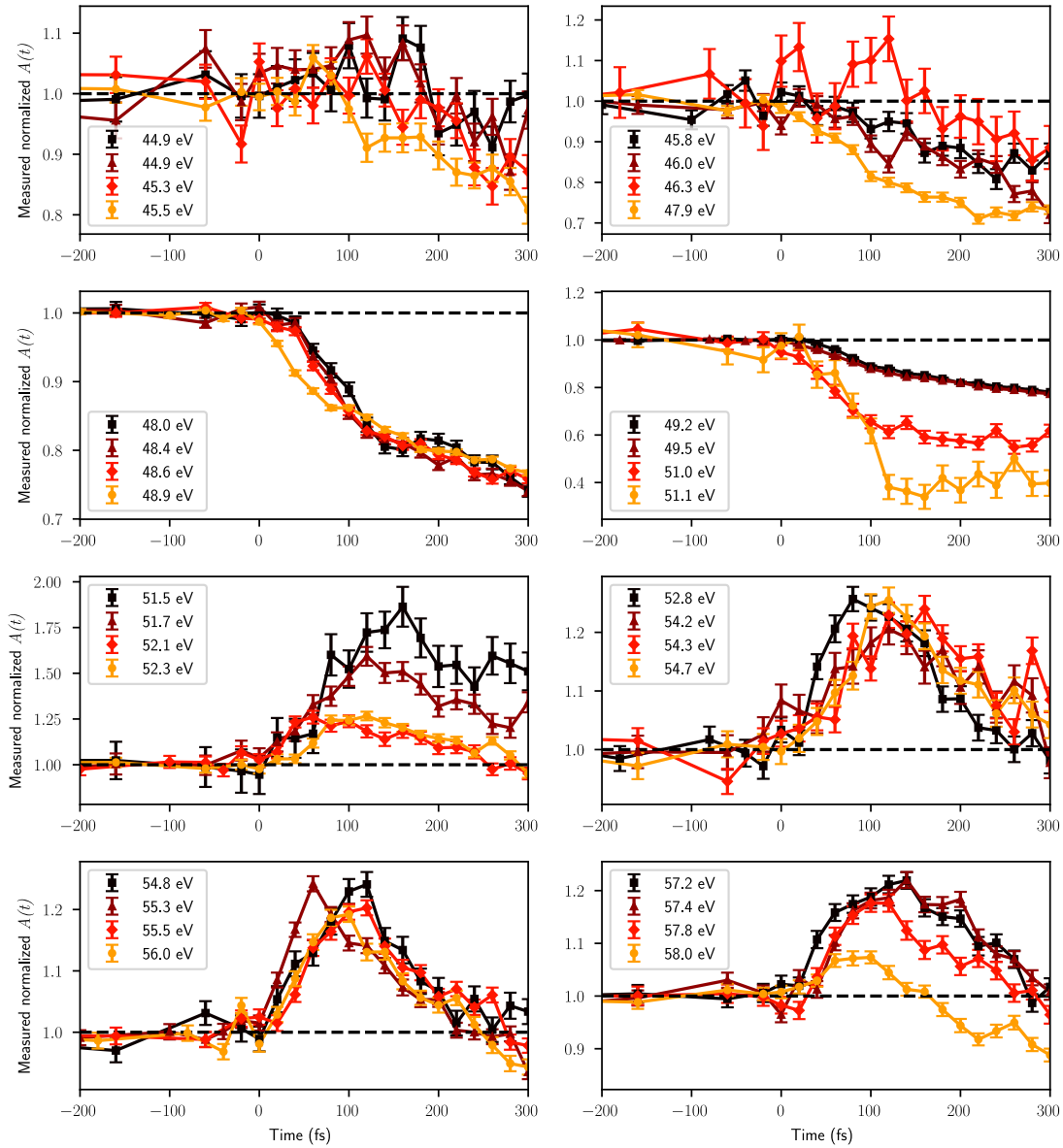


Figure 4.8: **Energy-dependent transient magnetic asymmetry with probing energies from 58.5 eV to 72.7 eV.** The absorbed pump fluence is  $2.2 \text{ mJ/cm}^2$ . The peak of the *Co* asymmetry occurs at 60.4 eV.

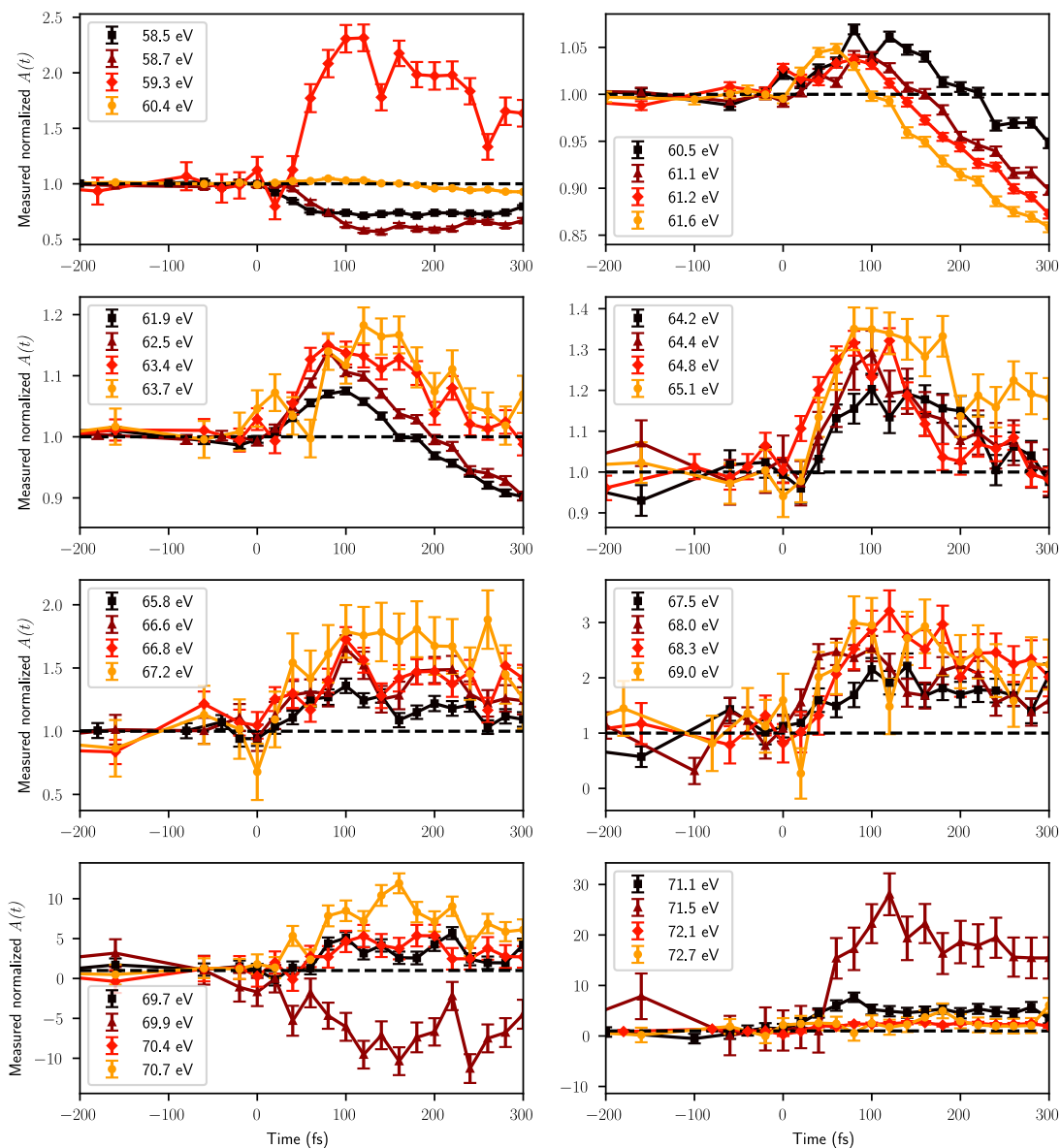


Figure 4.9: **Theoretical asymmetry curves at 0 fs, 40 fs, 80 fs and 100 fs following laser excitation from a 2.2 mJ/cm<sup>2</sup> pump pulse** (A) The asymmetry at 40 fs plotted across both the *Co* and *Mn* edges and (B) zoomed in on the *Co*-edge. At 40 fs, we see a reduction in asymmetry at the *Mn* and *Co* resonant peaks due to spin-flips. (C) The asymmetry at 80 fs and 100 fs and (B) zoomed in at the *Co*-edge. At 80 fs, we see enhancements across the *Co*-edge due to spin transfers. At 100 fs, the spin transfer excitations have mostly decayed and spin-flips begin to dominate once again.

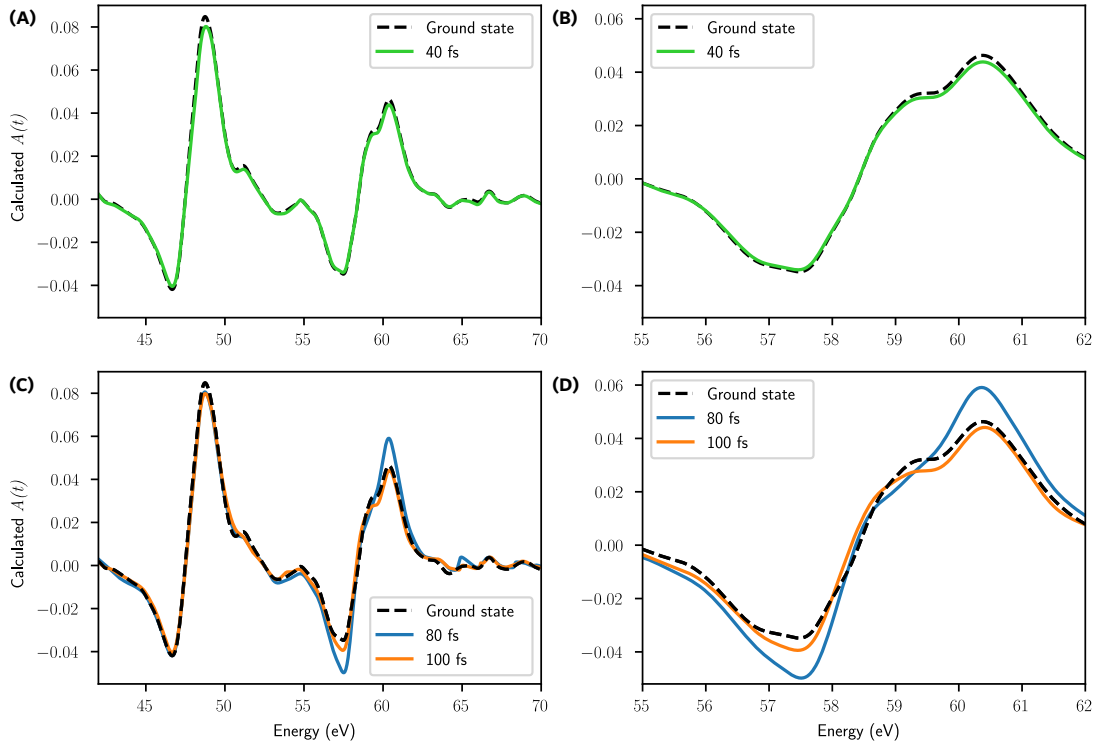


Figure 4.10: **Fluence-dependent transient magnetic asymmetry measurements with five different probing energies from 47.9 eV to 63.6 eV.** The fluences given in the legend correspond to absorbed fluence values. Around the *Mn*-edge, (i.e. 47.9 eV and 51.0 eV), demagnetization dominates at all fluences. Above and below the *Co*-edge at 63.6 eV and 57.2 eV, spin transfer dominates and the signal is enhanced. At the *Co*-edge, 60.4 eV, there is fluence-dependent competition between spin transfer and ultrafast demagnetization.

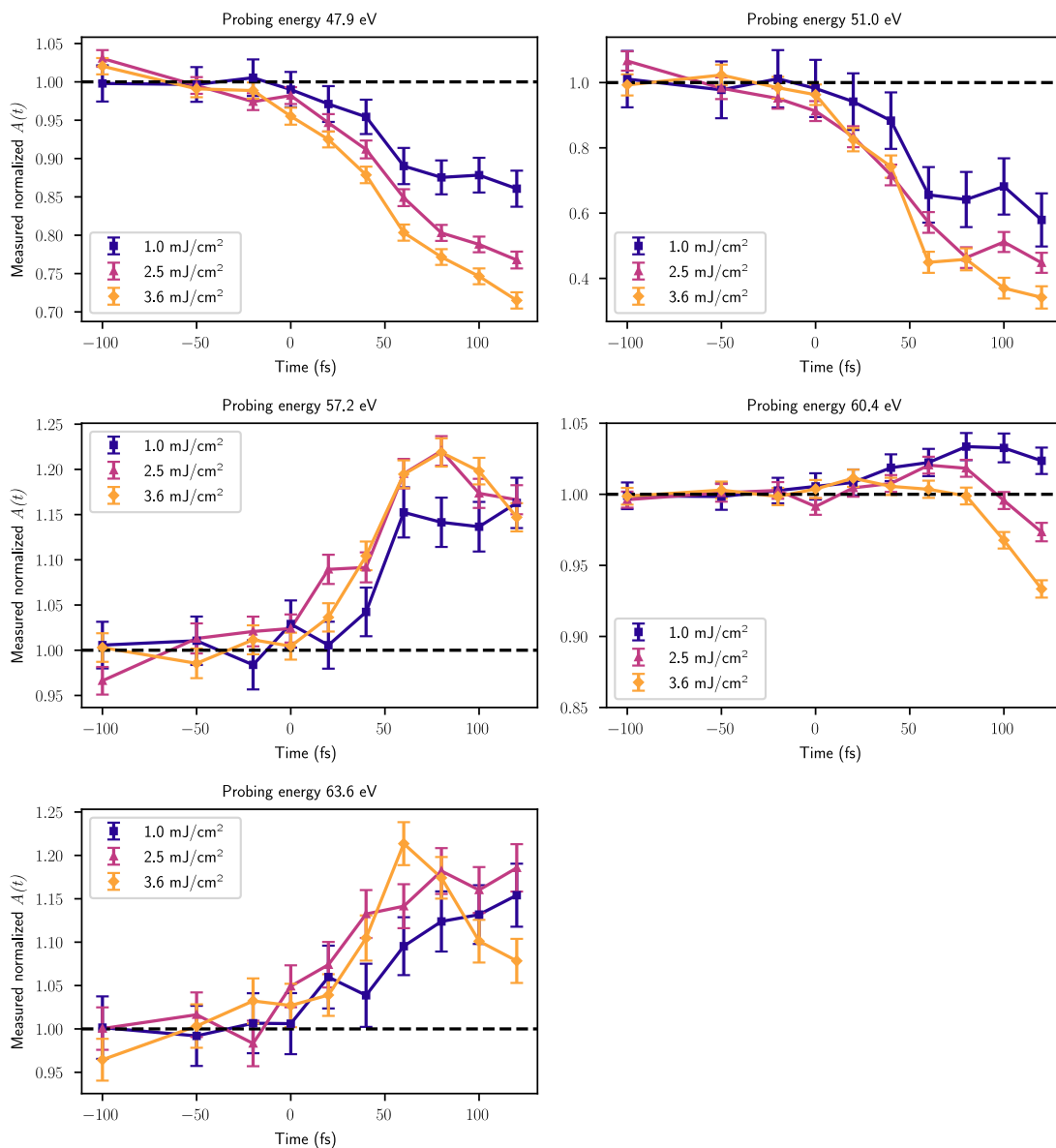


Figure 4.11: **The simulated transient changes in magnetic moment of *Co* and *Mn* with a pump fluence of  $8.4 \text{ mJ/cm}^2$**  Here, a large calculated OISTR effect of 10% for *Co* is depicted for an  $8.4 \text{ mJ/cm}^2$  pump fluence. In comparison, the *Co* moment only increases by  $\sim 2.5\%$  for  $2.2 \text{ mJ/cm}^2$  pumping. However, we note that the simulation does not include all effects that would contribute to demagnetization of *Co* such as: magnon generation, electron-phonon interactions, and superdiffusive spin currents. For this reason, we expect that this is an overestimation of the strength of the *Co* moment increase.

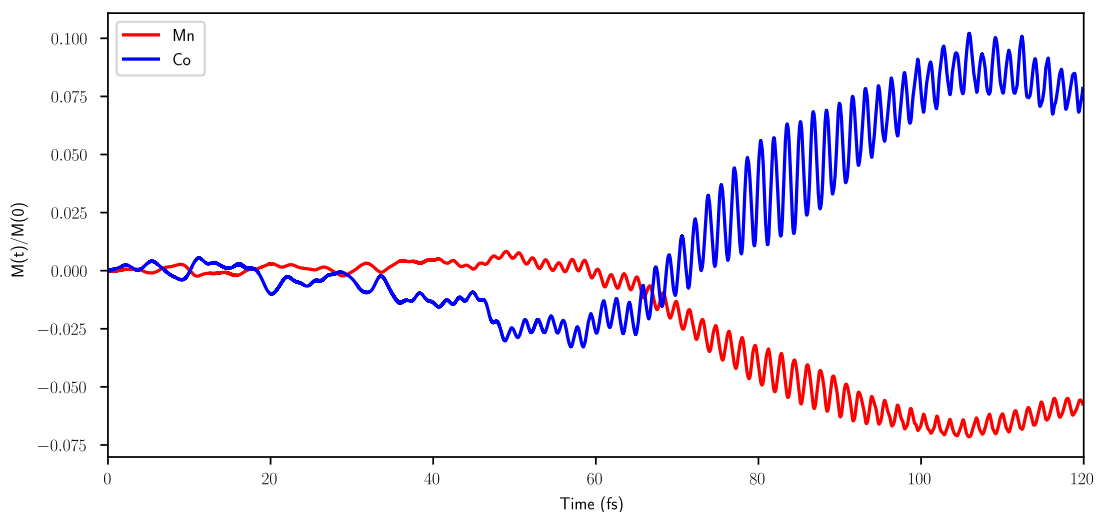


Figure 4.12: **The theoretical definition of  $t = 0$  relative to the time-dependent amplitude of the simulated incident pump pulse.** The theoretical time zero was chosen to maximize agreement with the experimentally determined time zero.

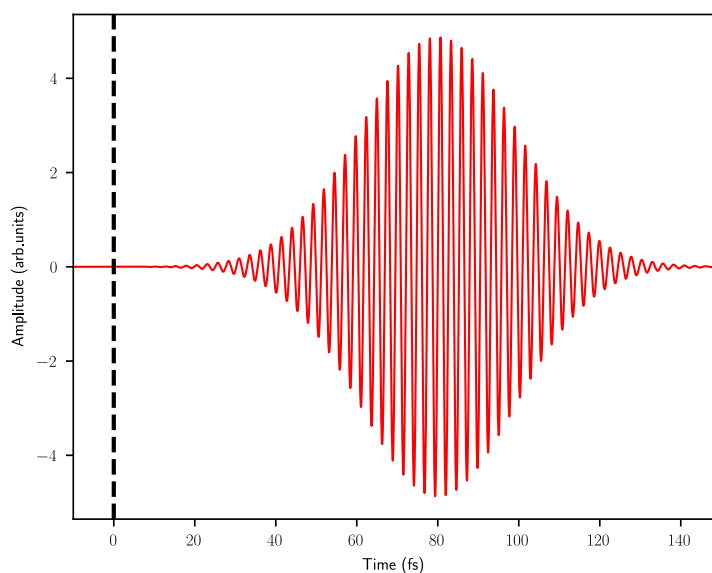
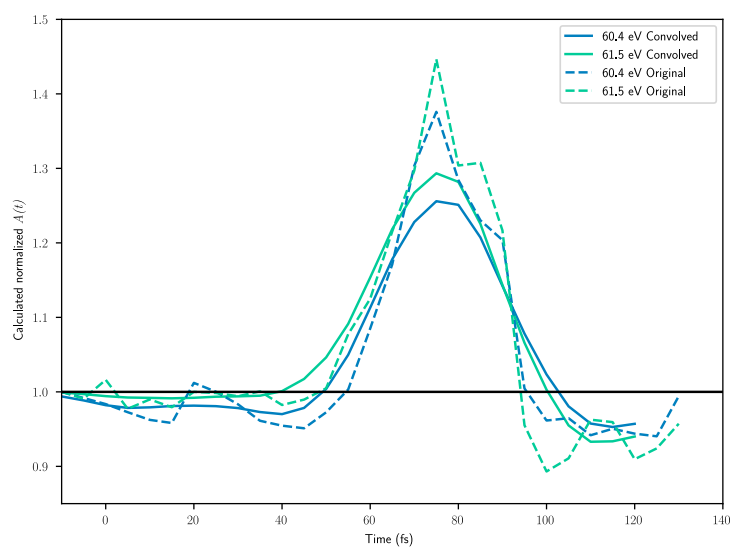


Figure 4.13: **The calculated theoretical magnetic asymmetry dynamics with and without convolving with a measurement probe.** Dashed lines: the instantaneous magnetic asymmetry calculated for two different probing energies: 60.4 eV and 61.5 eV in steps of 5 fs. Solid lines: the same theoretical data convolved with a 25 fs FWHM probe pulse as described in the main text, Fig. 4.3(d).



#### 4.4 Comparison with $Co_2MnGe$ and $Co$

Historically, the strength of the optically-induced spin transfer effect (OISTR) has predominantly been examined in terms of the initial and final states available for pump excitation between magnetic species within an alloy. By comparing two very similar Heusler alloys,  $Co_2MnGa$  and  $Co_2MnGe$ , we find that this description is too simplistic. Time-dependent density functional theory makes very similar predictions for the ground state magnetic asymmetries as well as the dynamic responses of these two alloys. However, we find experimentally that the shape of their asymmetries and the strength of their OISTR signatures differ greatly. Surprisingly,  $Co_2MnGa$  demonstrates strong laser-induced MOKE signal enhancements across the entire  $Co$ -edge while this behavior is theoretically predicted but not observed in measurements of  $Co_2MnGe$ . We compare the two  $Co$ -based Heusler alloys to a pure  $Co$  sample. In the pure  $Co$  sample, TD-DFT predicts strong intrasite spin-transfer based on the density of states. However, experimentally, transient enhancements in the  $Co$  MOKE signal are only detected in a small energy window just above the asymmetry signal's zero-crossing. This small window of enhanced MOKE was also identified in previous studies of  $Ni$ [19, 125] and  $NiFe$  alloys[145], indicating a wider trend. We attribute the near zero-crossing enhancement to a transient red-shifting of the absorption edge. We attribute the lack of spin-transfer based MOKE enhancements in the  $Co$  sample to the very short excited spin lifetimes in this material. The  $Co$  sample has a conductive minority band compared to half-metallic  $Co_2MnGe$  and  $Co_2MnGa$  which both have an insulating gap in their minority bands. Therefore, we can expect the lifetimes of excited minority spins to be much shorter in  $Co$  as compared to the two Heusler materials. We find that the prevalence of spin-transfer related MOKE enhancements depends on an intricate relationship between spin-polarization, spin-lifetimes, crystalline disorder and the density of states.

We discuss two very similar Heusler compounds:  $Co_2MnGa$  and  $Co_2MnGe$ .  $Ga$  and  $Ge$  are neighboring elements on the periodic table. Heusler materials show a very strong Slater-Pauling relationship[99]. Therefore, the addition of an extra valence electron in the unit cell of  $Co_2MnGe$  as

compared to  $Co_2MnGa$  gives  $Co_2MnGe$  an increased magnetic moment per unit cell of  $4.94 \mu_B$  as compared to  $4.06 \mu_B$  for  $Co_2MnGa$ [99]. Heuslers have generated a lot of recent research interest as they have excellent chemical stability, a wide range of tuneable ground state properties and the ability to host topological states as well as having promising applications in spintronics[112]. Our study of spin transfer in  $Co_2MnGa$  (as described in the previous section and in Ryan *et al.*[97]) identified strong energy-dependent OISTR signatures in the MOKE signal.  $Co_2MnGe$  was one of the first materials used to investigate the OISTR effect with element-specificity by Tengdin *et al.*[92] in 2020. Therefore, we will build on these two works by measuring  $Co_2MnGe$  with improved energy-resolution and fluence-dependence to determine whether the large and strongly energy-dependent signatures measured in  $Co_2MnGa$  are also present in the  $Co_2MnGe$ . We also measure pure  $Co$  to compare the MOKE signatures from a material where intersite spin transfers aren't possible but same-site spin transfers are predicted to be strong.

In the densities of states (DOS) shown in Fig. 4.14 it can be seen that both  $Co_2MnGa$  (Fig. 4.14.(a)) and  $Co_2MnGe$  (Fig. 4.14(b)) are half-metallic, i.e. they have an insulating gap in their minority spin channel. Furthermore, within the energy range of the electronic excitations that could be induced by the pump laser (1.54-1.60 eV excitations) there is a strong excitation pathway in both Heuslers where electrons from  $Co$  minority states below the Fermi energy could be excited into  $Mn$  minority states above the Fermi energy. This  $Co$ - $Mn$  spin-transfer effect will transiently increase the  $Co$  magnetization while reducing the  $Mn$  magnetization.

The experimental aim is to measure the transient MOKE signal across the  $M$ -edges of the three samples, and identifying which parts of the signal show transient enhancements. Then, we will investigate each of these regions and determine whether the transient enhancements in the MOKE signal originate from intersite transfers (i.e. OISTRs), same-site spin transfers, or other magneto-optical effects. This expansive analysis across multiple fluences and probe energy regimes for three related magnetic materials will allow us to identify deeper trends in ultrafast magnetism.

#### 4.4.1 Results

As described in Section 4.3.1, a 40-55  $fs$ ,  $\sim 800$   $nm$  pump pulse excites the sample and the dynamics are probed with EUV TMOKE using a probe pulse with a duration of  $\sim 25$   $fs$ .

Four samples are utilized in this study: (a) a 20  $nm$   $Co_2MnGa$  sample grown in the  $L2_1$  with a 3  $nm$  Si cap, (b) two 10  $nm$   $Co_2MnGe$  samples, one grown in the  $A2$  phase and one grown in the  $B2$  phase, both with a 2.8  $nm$  Ta capping layer (oxidized) and (c) a polycrystalline 15  $nm$   $Co$  sample with a 5  $nm$   $Si_3N_4$  capping layer. A description of the  $Co_2MnGa$  growth methods are given in Ryan *et al.*[97]. A description of the  $Co_2MnGe$  growth methods are given in Shaw *et al.*[146]. The  $A2$  phase of  $Co_2MnGe$  has no half-metallic bandgap. However, the bandgap is present in the more ordered  $B2$  and  $L2_1$  phases[146]. The TD-DFT could only simulate one-unit cell and so the effects of crystalline disorder were not taken into consideration in the calculations. Therefore, both the  $Co_2MnGa$  and  $Co_2MnGe$  were simulated for the  $L2_1$  phase and the  $Co$  sample was simulated as a fully ordered HCP crystal. The specific details of the implementation of TD-DFT utilized are described in Ryan *et al.*[97].

$Co_2MnGe$  has a half-metallic minority bandgap of approximately 0.54  $eV$ [147] as seen in Fig. 4.14(b). Due to the extra electron in elemental  $Ge$  compared to elemental  $Ga$ , the  $Co_2MnGe$  sample has a Fermi energy that appears “shifted” to higher energies compared to  $Co_2MnGa$  in the density of states, Fig. 4.14. In the minority band of  $Co_2MnGa$ , the energies of the bonding and antibonding  $d$ -orbitals almost overlap with the Fermi energy[148], Fig. 4.14(a). Therefore, the half-metallic gap in this material is commonly referred to as a pseudogap. Despite this, for both  $Co_2MnGe$  and  $Co_2MnGa$ , almost perfect spin polarization is attainable at the Fermi energy[149]. The pure  $Co$  sample (Fig. 4.14(c)) is not half-metallic and therefore has available states at the Fermi energy in both the spin-up channel and the spin-down channel.

Previous studies of  $Co_2MnGe$ [146], and isoelectronic  $Co_2MnSi$ [150], have shown that the  $B2$  phase shares a very similar DOS to the  $L2_1$  phases. The disorder of the  $B2$  phase acts to globally smooth features seen in the DOS of the  $L2_1$  phase. Additionally, in the  $B2$  phase, there is a small

narrowing of the minority bandgap as compared to the  $L2_1$  phase. However, the overall electronic structure is very similar between these two phases[146, 150]. Furthermore, the magnetic damping is similar between the  $B2$  and  $L2_1$  phases of  $Co_2MnGe$ : 0.0009 for the  $B2$  phase and 0.0005 for the  $L2_1$  phase[146]. The total magnetic moment of the two phases is also extremely similar, agreeing to within 0.01%[146]. With these strong similarities between the  $B2$  and  $L2_1$  phases, we should expect similar laser-induced dynamics. For this reason, conclusions drawn from TD-DFT simulations of an  $L2_1$  unit cell should still be relevant for understanding the  $B2$  phase of  $Co_2MnGe$ .

The band structure of the  $Co_2MnGe$   $A2$  phase (full intersite disorder) is very different to that of the  $L2_1$  phase. There is no half-metallic gap because  $Co$  anti-site disorder locally destroys the half-metallicity and reduces the spin polarization at the Fermi level[146, 151]. Furthermore, the overall shape of the DOS has quite different features[92, 146]. The magnetic damping for the  $A2$  phase is 0.0075[146] which is an order of magnitude larger than the magnetic damping for the  $B2$  or  $L2_1$  phases. Despite the differences in the damping rate between the  $B2$  and  $A2$  phases, a study by Tengdin *et al.*[92] showed that the  $A2$  and  $B2$  phases of  $Co_2MnGe$  exhibit near identical demagnetization rates. This indicates that the  $Co_2MnGe$  demagnetization rate is not well predicted by either the level of disorder or the size of the minority bandgap, despite these parameters previously being used to explain the demagnetization rate of  $Co_2MnSi$ [120]. Tengdin *et al.*[92] measured a dynamic MOKE enhancement at the  $Co$ -edge of the  $B2$  phase of  $Co_2MnGe$  caused by intersite spin-transfer. However, this enhancement was not present when Tengdin *et al.* measured at the same energy in the  $A2$  phase.

In all three materials ( $Co_2MnGa$ ,  $Co_2MnGe$ , and pure  $Co$ ), there is a large number of available states above the Fermi energy in the  $Co$  spin-down band. Therefore, we expect many excitations in the spin-down channel associated with  $Co$ . This is confirmed by the TD-DFT calculations which show an increased population of these states following laser excitation.

Fig. 4.15 shows the measured and calculated ground state asymmetries for the three materials. Fig. 4.15(a) shows good qualitative agreement between the theoretical and experimental asymmetry curves of  $Co_2MnGa$ , as discussed in our previous study[97] and Section 4.3.1.

Figure 4.14: **The calculated spin-resolved projected density of states (PDOS).** The PDOS is separated by elemental contributions for the  $L2_1$  phases of (a)  $Co_2MnGa$  (b)  $Co_2MnGe$ , and (c) the HCP phase of pure Co. A pump excitation of approximately  $1.55\text{ eV}$  excites electrons across the half-metallic gaps of  $Co_2MnGa$  and  $Co_2MnGe$ .

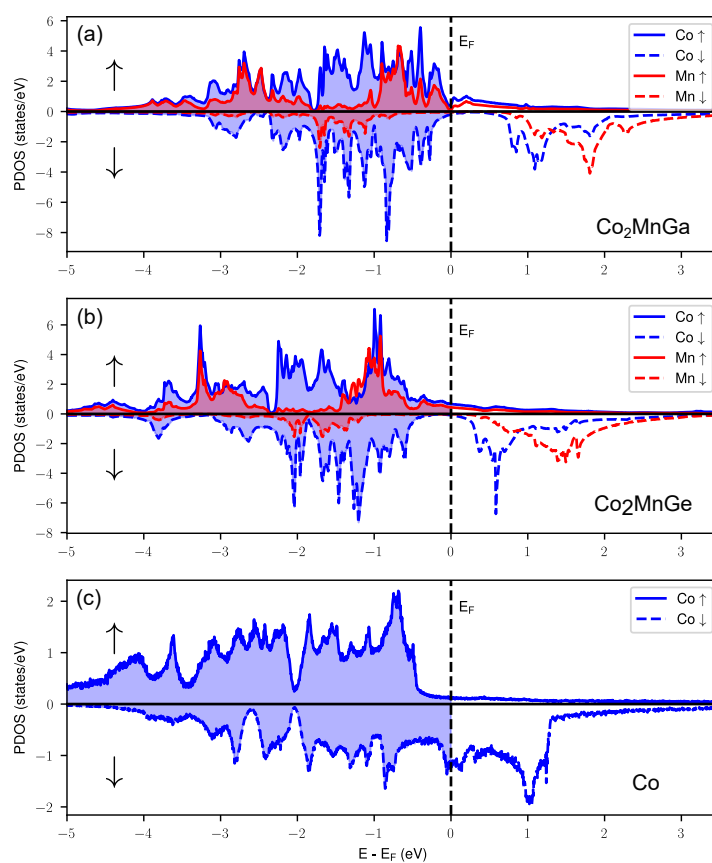
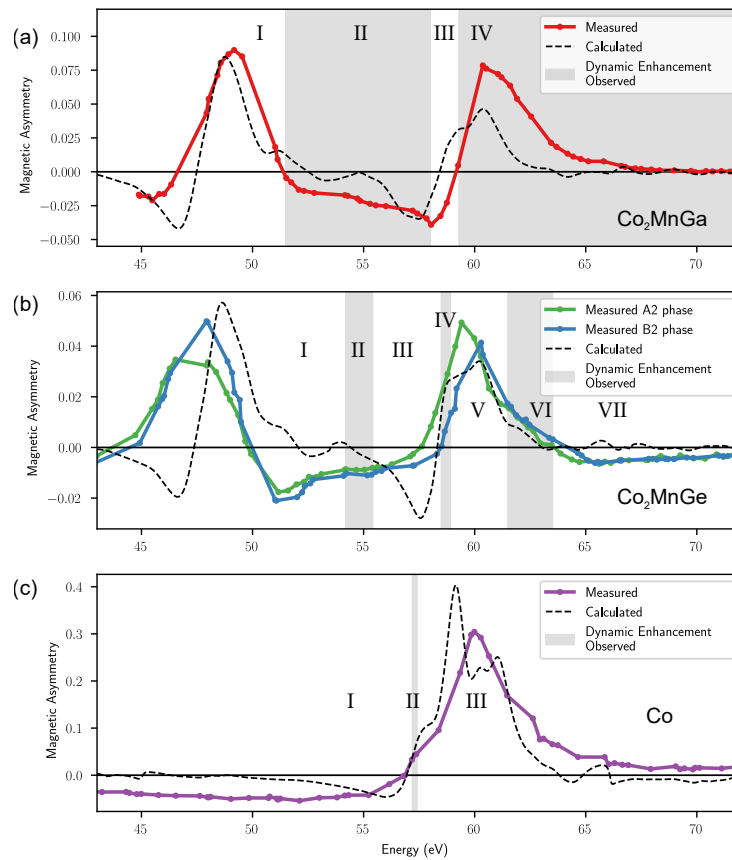


Figure 4.15: **The measured and calculated ground state asymmetries.** Gray bars indicate regions where the measured asymmetry exhibits a transient enhancement following laser pumping with an incident fluence of  $3.4 \text{ mJ/cm}^2$ . The corresponding absorbed fluences are  $2.5 \text{ mJ/cm}^2$  for both  $Co$  and  $Co_2MnGe$ , and  $2.2 \text{ mJ/cm}^2$  for  $Co_2MnGa$ . Regions are marked with Roman numerals. (a) The measured and calculated ground state asymmetry for a  $Co_2MnGa$   $L2_1$  crystal. Enhancements of the magnetic asymmetry in  $Co_2MnGa$  are seen at a large range of energies both above and below the  $Co$  resonant peak as shown by the gray bars. (b) The measured ground state for the  $A2$  and  $B2$  crystal phases of  $Co_2MnGe$ . The calculated asymmetry assumes no crystalline disorder ( $L2_1$ ). The gray bars indicate regions where a transient enhancement was measured for the (more ordered)  $B2$  phase. (c) The measured asymmetry from the polycrystalline pure  $Co$  sample and the calculated asymmetry for an ordered HCP  $Co$  lattice.



However, in Fig. 4.15(b) the shape of the measured ground state asymmetry of  $Co_2MnGe$  differs from what is predicted by DFT. In particular, the central energy region from  $51\text{ eV} - 57\text{ eV}$  exhibits a very different shape in the calculated asymmetry compared to the measured asymmetry. In the measured signal, this energy region has a positive slope. However, in the theoretical asymmetry the slope is negative. Furthermore, for the highest energies (region VII) the measured asymmetry is negative. Meanwhile, the theoretical asymmetry is positive (excluding some small negative oscillations).

The most obvious explanation for why the  $Co_2MnGe$  asymmetry differs from the theoretical calculations is that the  $Co_2MnGe$  sample is more disordered (being in the  $B2$  phase). By comparison, the fully ordered  $L2_1$  phase of the  $Co_2MnGa$  sample shows better agreement with theory. However, this hypothesis does not hold up well under further scrutiny. The  $B2$  and  $L2_1$  phases have very similar densities of states, magnetic moments, and Gilbert damping[146]. Meanwhile, the  $A2$  phase has a very different DOS (no half-metallic gap), an order of magnitude higher Gilbert damping, and very different magnetic moments per atomic site[146]. Despite this, the shape of the  $A2$  phase asymmetry is very similar to  $B2$  phase asymmetry, Fig. 4.16(b). The main difference between the measurements of the  $A2$  and  $B2$  phase asymmetries is the relative heights of the  $Co$  and  $Mn$  peaks, Fig. 4.16(b). This difference is expected based on the calculated magnetic moments per atomic site of the  $A2$  and  $B2$  phases. The magnetic moment for  $Co$  is approximately 25% higher for the  $B2$  phase compared to the  $A2$  phase, but 60% lower for  $Mn$ [146]. In comparison, the differences in the calculated moments for  $Mn$  and  $Co$  between the  $B2$  and  $L2_1$  phases are less than 2%[146]. Therefore, if the difference between the theoretical asymmetry curve and the measured  $B2$  asymmetry curve is due to disorder, we should expect a much larger difference in the asymmetry curves between the  $A2$  and  $B2$  phases (other than just a change in the relative heights of the peaks).

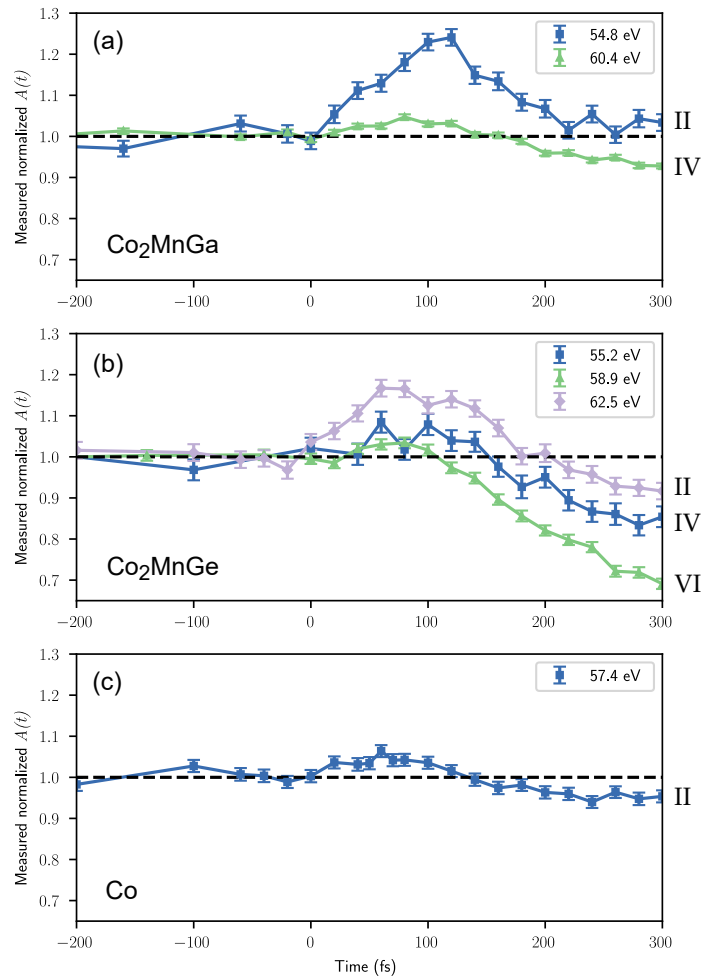
In Fig. 4.15, every region where a transient enhancement in the MOKE signal was measured is highlighted in gray. Transient enhancements measured in the MOKE signal have previously been used as a signature of the OISTR effect[92, 93]. However, enhancements have also been measured in pure elements in specific energy regimes[19, 125, 145]. Therefore, we must disentangle the origins of

these enhancement signatures by comparing the behavior of the three samples alongside simulations from TD-DFT. This will allow us to determine the strength of the spin-transfer effects in each of the three materials.

We note that in all three samples, we see specific behaviors occurring around the zero-crossing below the *Co* peak (i.e. in the 55-60 eV range). For each of the three samples, we see a region of transient MOKE enhancement just above the zero-crossing and a region of transient decrease just below the zero-crossing. In the case of *Co<sub>2</sub>MnGa*, this manifests as an isolated region of “no enhancement” just below the zero-crossing as shown in Fig. 4.15(a) region III. For the *Co<sub>2</sub>MnGe* and pure *Co* samples, this leads to isolated regions of enhancements above the zero-crossings in Figs. 4.15(b) region IV and (c) region II, respectively. In the pure *Co* sample, region II (above zero-crossing) is the only region of enhancement. A typical signal from region II (at a probe energy of 57.4 eV) is depicted in Fig. 4.16(c). In all three samples, the enhancement in this energy regime can be explained by a red-shifting of the zero-crossing. In the vicinity of the zero-crossing, the asymmetry curve is steep and the absolute magnitude of the MOKE signal is small. If the zero-crossing shifts to lower energies (i.e. redshifts), then the absolute magnitude of positive valued asymmetries will be increased, and the absolute magnitude of negative valued asymmetries will be reduced.

Several previous works have identified red-shifting of the magneto-optical signal following laser excitation and have explained the possible mechanisms[8, 125, 126, 127, 129, 128]. Previous studies have shown transient enhancements measured in pure *Ni* in the regime just above the zero-crossing[19, 125, 145]. Similarly, multiple OISTR studies have identified a transient enhancement of *Ni* in an *FeNi* alloy but only at energies just above the zero-crossing[145, 93]. Furthermore, one such study[145] found that when the angle of incidence of the probe was changed this shifted the zero-crossing energy from below the probe energy to above the probe energy. At angles where the zero-crossing was above the probe energy, enhancements were replaced with very fast reductions in asymmetry. This agrees with the measurements in this study. For example, for *Co<sub>2</sub>MnGe*, in Fig. 4.22, we see a very rapid decrease in the MOKE signal at 58.3 eV (below zero-crossing) and a very rapid enhancement in the MOKE signal at 58.5 eV (above zero-crossing). One study measured

Figure 4.16: **Examples of transient MOKE signals from the regions of enhancement that were highlighted in gray in Fig. 4.15.** Roman numerals correspond to regions marked in Fig. 4.15. The incident laser fluence was  $3.4 \text{ mJ/cm}^2$ . The corresponding absorbed fluences were  $2.5 \text{ mJ/cm}^2$  for both  $Co$  and  $Co_2MnGe$ , and  $2.2 \text{ mJ/cm}^2$  for  $Co_2MnGa$ . (a) The transient asymmetry signal of  $Co_2MnGa$  with two different probing energies from the two distinct regions of the enhancement. (b) The transient enhancements of the asymmetry signal for the  $B2$  phase of  $Co_2MnGe$  from three distinct regions. (c) Enhancements in  $Co$  were only observed in a very narrow region of energies near the zero-crossing. One such signal from this region is depicted.



the OISTR effect in the conductor *CoPt*. In this case, the zero-crossing regime wasn't specifically probed, and no transient enhancements were detected[96]. In the *CoPt* study, the OISTR effect was inferred based on demagnetization rates[96]. In fact, the half-metallic Heuslers *Co<sub>2</sub>MnGe* and *Co<sub>2</sub>MnGe*[92, 97] appear to be the only alloys where energy-resolved spin-transfer based MOKE enhancements have been measured away from the zero-crossing. This leads us to the conclusion that half-metals may be uniquely capable of sustaining excited OISTR electrons long enough to induce a measurable enhancement in the MOKE signal. Minority spins excited above a half-metallic gap are “trapped” by the insulating gap. Meanwhile, in conductors, we expect optically excited electrons to rapidly scatter back to lower energy states. Transient MOKE enhancements with visible probes (non-element specific) have also been seen for half-Heuslers[95].

Outside of the zero-crossing region, the *Co<sub>2</sub>MnGa* sample shows enhancements across every energy associated with *Co*, Fig. 4.15(a). This experimental observation agrees with predictions from TD-DFT which also show an enhancement across the *Co*-edge, Fig. 4.18. The *Co* enhancement comes from the transfer of minority *Co* spins to *Mn*, i.e. an OISTR effect between *Co* and *Mn*. Fig. 4.4 shows typical dynamic MOKE signals taken from the “regions of enhancement” marked in gray bars in Fig. 4.15. In *Co<sub>2</sub>MnGa* (Fig. 4.16(a)) there is a small enhancement at the *Co* signal peak (60.4 eV) i.e. region IV. There is a much larger enhancement in the MOKE signal in region II. Region II is mixed between high energy *Mn* character and low energy *Co* character unlike region IV which is predominated by *Co* contributions.

The broad range of regions of enhancement observed in *Co<sub>2</sub>MnGa* was not observed for the *Co<sub>2</sub>MnGe* B2 phase sample, Fig. 4.15(b). In *Co<sub>2</sub>MnGe*, enhancements were also predicted across the entire *Co*-edge from TD-DFT. However, enhancements were only seen in a narrower selection of energies. The largest region of enhancement in *Co<sub>2</sub>MnGe* was region VI which corresponds to positive asymmetries above the *Co* peak. There is no enhancement in adjacent region VII (where the signal is negative), or at the *Co* peak itself, region V. There is an additional narrow regime of enhancement at around 55 eV, region II. Region II is between *Mn* and *Co* and most likely contain a mixture of contributions from each. Region IV is the regime of near zero-crossing enhancements as

discussed above.

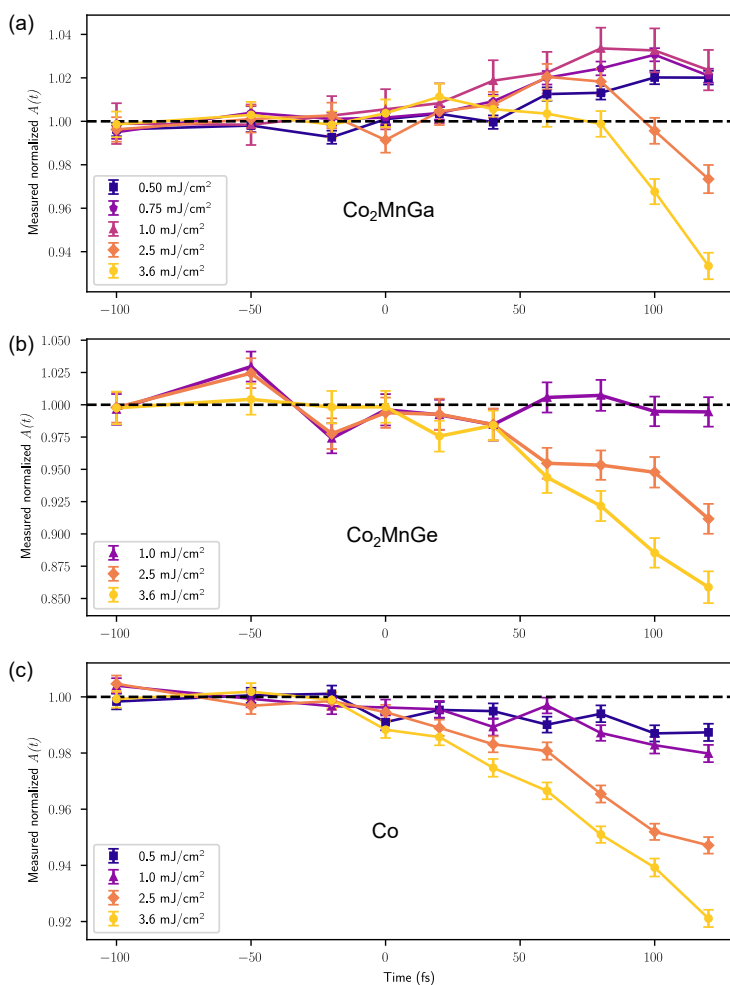
Typical signals for each of the regions of enhancement in  $Co_2MnGe$  are given in Fig. 4.16(b). One possible explanation for the  $Co$ -edge MOKE enhancements being weaker in  $Co_2MnGe$  compared to  $Co_2MnGa$  may be due to increased spin-orbit coupling (SOC) in  $Co_2MnGe$ . Spin-orbit coupling mixes spin-up and spin-down bands and makes scattering between them more probable. SOC reduces the lifetime of excited minority spins as it allows spins in the minority band to be scattered into the majority band. Increased SOC based scattering could prevent laser excitations from inducing a strong population build-up above the Fermi energy. It is predicted that  $Co_2MnGe$  has approximately twice the orbital moment per unit cell of  $Co_2MnGa$ [152]. Furthermore, the additional valence electron in the  $Co_2MnGe$  (relative to  $Co_2MnGa$ ) pushes the Fermi energy higher and this means that the available states in the minority band are closer to the Fermi energy where spin-orbit coupling effects are stronger[56]. In the TD-DFT calculations of  $Co_2MnGa$ , spin-transfer based MOKE enhancements weren't as strong at the  $Co$  peak compared to other regions. This was attributed to increased SOC based spin-flips at the  $Co$  peak due to its proximity to the Fermi energy. This is discussed in Section 4.3.1. Therefore, with available states in  $Co_2MnGe$  being closer to the Fermi energy, we might expect that demagnetizing effects could fully overwhelm spin-transfer based enhancements to the point where no enhancements are detected at the  $Co$  peak.

To verify that we were not in the wrong fluence regime for detecting enhancements we measured at several different fluences as shown in Fig. 4.17. For each sample, fluence-dependent data was taken with the harmonic comb tuned on resonance with the  $Co$  peak (60.4 eV for  $Co_2MnGa$  and 60.3 eV for both  $Co_2MnGe$  and pure  $Co$ ). For all three samples, as the fluence was increased, the demagnetization increased, Fig. 4.17.

Enhancements at the  $Co$ -peak of  $Co_2MnGa$  saturate at around  $1.0 \text{ mJ/cm}^2$ , Fig. 4.17(a), as described in our recent study of  $Co_2MnGa$ [97].

No enhancements are detected at the  $Co$  peak for any of the measured fluences on either the  $Co_2MnGe$  sample or the pure  $Co$  sample, Figs. 4.17(b) and (c). At an absorbed fluence of  $1.0 \text{ mJ/cm}^2$ , almost no change is measured in the  $Co_2MnGe$  MOKE signal following laser pumping.

Figure 4.17: **Fluence dependence at the peak of the  $Co$  signal for the three samples.** The fluences given in the legend correspond to absorbed fluence values. (a) The  $Co$  peak ( $60.4\text{ eV}$ ) shows a transient enhancement in  $Co_2MnGa$ . This enhancement is quenched at higher fluences. (b) At the  $Co$  peak in the  $B2$  phase of  $Co_2MnGe$  ( $60.3\text{ eV}$ ), there are no perceptible dynamics with  $1.0\text{ mJ/cm}^2$  pump fluence. However, as the fluence is increased, the demagnetization increases. No enhancements are seen at any fluence. (c) In the pure  $Co$  sample, the demagnetization increases with increasing fluence but no enhancements are seen at the peak asymmetry peak ( $60.3\text{ eV}$ ) at any fluences.



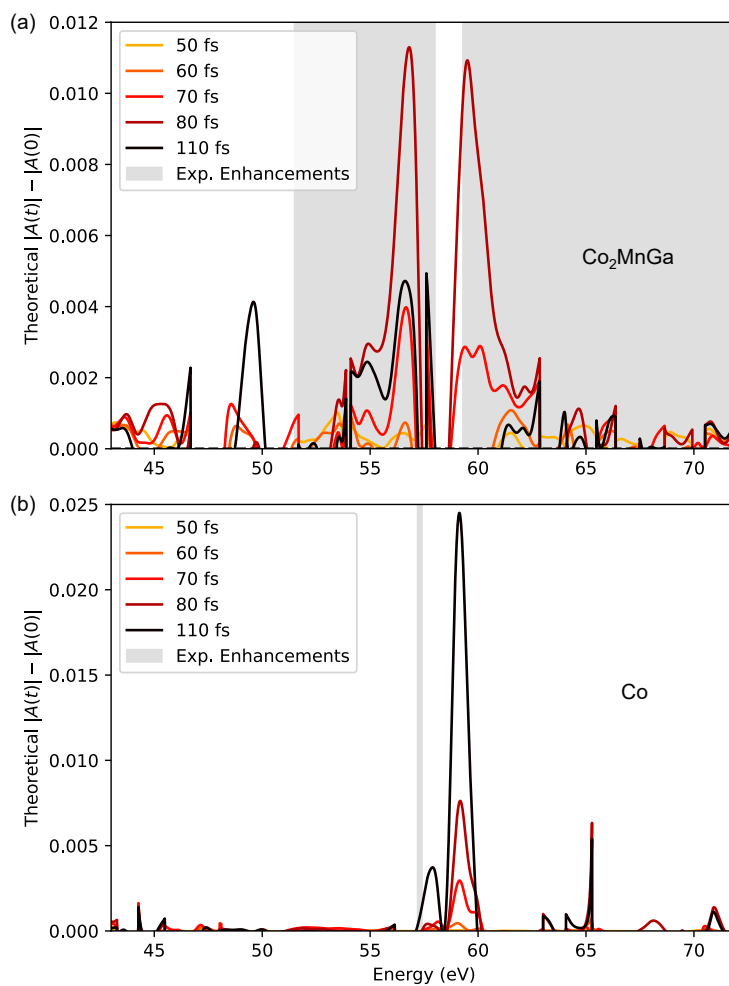
However, this relatively static MOKE signal may contain competing effects from the spin-transfer and demagnetization pathways. While  $Co_2MnGe$  exhibits less demagnetization than  $Co$  at  $1.0 \text{ mJ/cm}^2$ , it exhibits a much larger percentage demagnetization at a fluence of  $3.6 \text{ mJ/cm}^2$ . This is evidence that there could be competing effects in the  $Co_2MnGe$  signal which gives a more complex fluence dependence compared to the pure  $Co$  sample in which the percentage demagnetization follows a more linear trend with increasing fluence.  $Co_2MnGe$  has a Curie temperature,  $T_C$ , of  $905 \text{ K}$ [153] which is higher than that of  $Co_2MnGa$  at  $694 \text{ K}$ [153] but not as high as bulk  $Co$  at  $1403 \text{ K}$ [154].

The theoretical regions of enhancement of  $Co_2MnGa$  and  $Co$  are shown in Fig. 4.18. In Fig. 4.18(a) there is good agreement between the experimental regions of enhancement (depicted with gray bars) and the theoretical time-dependent enhancements (depicted with solid lines). Fig. 4.18(b) shows a broad range of energies above the zero-crossing where there are theoretical predictions of transient enhancements of the pure  $Co$  MOKE signal. However, the experimental range of enhancements (shown with a gray bar) is much more restricted. The TD-DFT generally underpredicts the strength of demagnetizing and scattering effects, as described in more detail in Section 4.3.2. Therefore, the enhancements predicted for certain energy regions of  $Co_2MnGe$  and  $Co$  due to spin-transfers were often not present in the measurements.

#### 4.4.2 Discussion

We have demonstrated that, much like  $Co_2MnGa$ , the strength of the MOKE enhancements in  $Co_2MnGe$  have a strong energy-dependence. Furthermore, in  $Co_2MnGe$ , no enhancements are seen at the  $Co$  peak itself. This leads us to dispute some of the claims in the original  $Co_2MnGe$  spin transfer study[92], specifically the claim that the  $Co$  moment grows by 10%. The measured % MOKE enhancement is very different for each probed energy. The absorbed pump fluence used in the  $Co_2MnGe$  measurements and TD-DFT calculations was  $2.5 \text{ mJ/cm}^2$  (which is similar to the value used in the original paper of  $2.4 \text{ mJ/cm}^2$ ). The calculated % increase in the  $Co$  moment from TD-DFT is only a few percent. Furthermore, the TD-DFT predict of the  $Co$  moment increase is most likely an overestimation since TD-DFT underestimates the strength of demagnetizing effects.

Figure 4.18: **The absolute enhancements in the theoretical asymmetries.** Enhancements are given for two samples: (a)  $Co_2MnGa$  and (b) pure  $Co$ .



We note that the sample used for the  $Co_2MnGe$  measurements was part of the same sample series as the one used by Tengdin *et al.*[92] and should have similar characteristics[146]. Furthermore, data from the  $Co_2MnGe$  without any energy shifting of the driving laser was in good agreement with the original work as demonstrated in our X-MATTER beamline design paper[87].

The pure  $Co$  sample showed a MOKE enhancement in the energy region just below the  $Co$  peak, near the zero-crossing. This was in agreement with similar observations from  $M$ -edge studies of  $Ni$  and  $FeNi$  samples. No enhancements were seen elsewhere  $Co$  sample despite predictions of strong same-site transfers in the spin down channel of  $Co$ . We postulate that spin-transfer based MOKE enhancements may not be measurable in conductors with the pump and probe durations used in this study. In metallic samples, excited electrons can rapidly scatter to lower energy states. However, in half-metallic samples such as  $Co_2MnGa$  and  $Co_2MnGe$ , excited minority spin lifetimes are extended by the insulating gap. The extended lifetimes give an opportunity for a measurable spin-transfer signal to build throughout the pulse duration.

It is observed that enhancements near the zero-crossing, due to spectral red-shifting, are common across many materials. This was observed for the three materials in this study as well as being replicated in many other ultrafast studies. This signature may be misinterpreted as a spin-transfer effect.

#### 4.4.3 Conclusion

In conclusion, by taking comprehensive energy tuned EUV TMOKE data on the three samples,  $Co_2MnGa$ ,  $Co_2MnGe$  and pure  $Co$ , and comparing the measurements with TD-DFT calculations, we are able to identify key energy regions of transient MOKE enhancements which we attribute to spin transfers as well as red-shifting effects. MOKE enhancements in  $Co_2MnGe$  were less pronounced than in those in  $Co_2MnGa$  which we attribute to increased SOC strength in the  $Co_2MnGe$  sample. While intersite spin-transfer effects are not possible in pure  $Co$ , strong intrasite spin-transfers were expected in the minority channel. However, enhancements in pure  $Co$  were not observed outside of the zero-crossing regime. We hypothesize that excited spin-lifetimes in conductors are too short for

spin-transfer based enhancements to be measurable for a 10's of femtoseconds duration of the pump and probe pulses.

#### 4.4.4 Supplemental Figures

This section contains Figs. 4.19-4.23 which supplement the findings of Section 4.4. For the pure *Co* sample, fluence-dependent curves at additional probing energies (aside from those at the *Co*-peak shown in Fig. 4.17) aren't given, unlike the other two samples. This is because the data quality at other energies was not sufficient to distinguish meaningful trends. Fluence-dependent curves for *Co<sub>2</sub>MnGa* appear earlier in this chapter in the Fig. 4.10. Fluence-dependent curves for *Co<sub>2</sub>MnGe* are given in this section in Fig. 4.23.

Figure 4.19: **Energy-dependent  $Co$  dynamics from to 42.4 eV to 59.3 eV.** The incident laser fluence was  $3.4 \text{ mJ/cm}^2$  corresponding to an absorbed fluences of  $2.5 \text{ mJ/cm}^2$ .

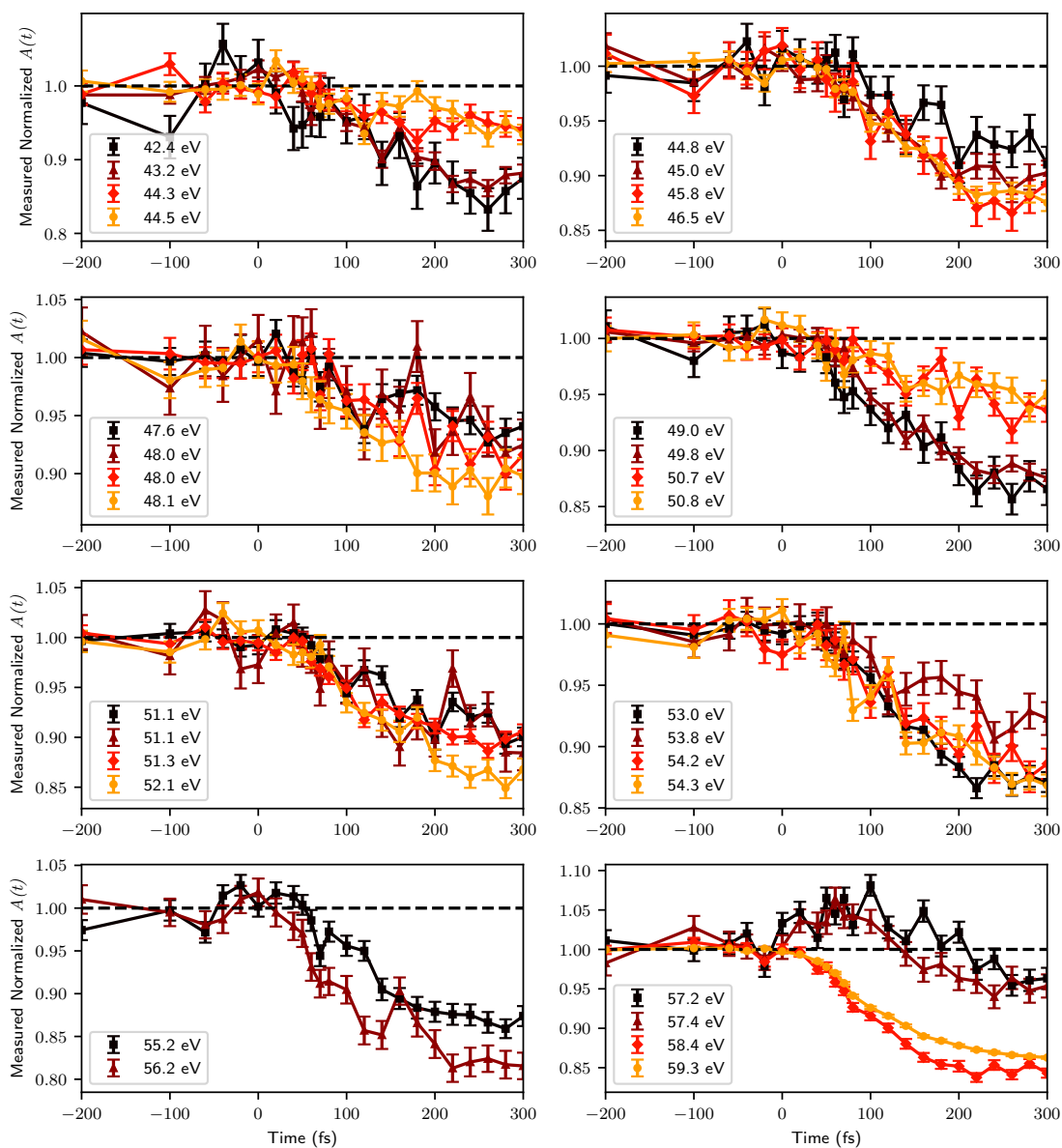


Figure 4.20: **Energy-dependent  $Co$  dynamics from to 59.8 eV to 72.6 eV.** The incident laser fluence was  $3.4 \text{ mJ/cm}^2$  corresponding to an absorbed fluences of  $2.5 \text{ mJ/cm}^2$ .

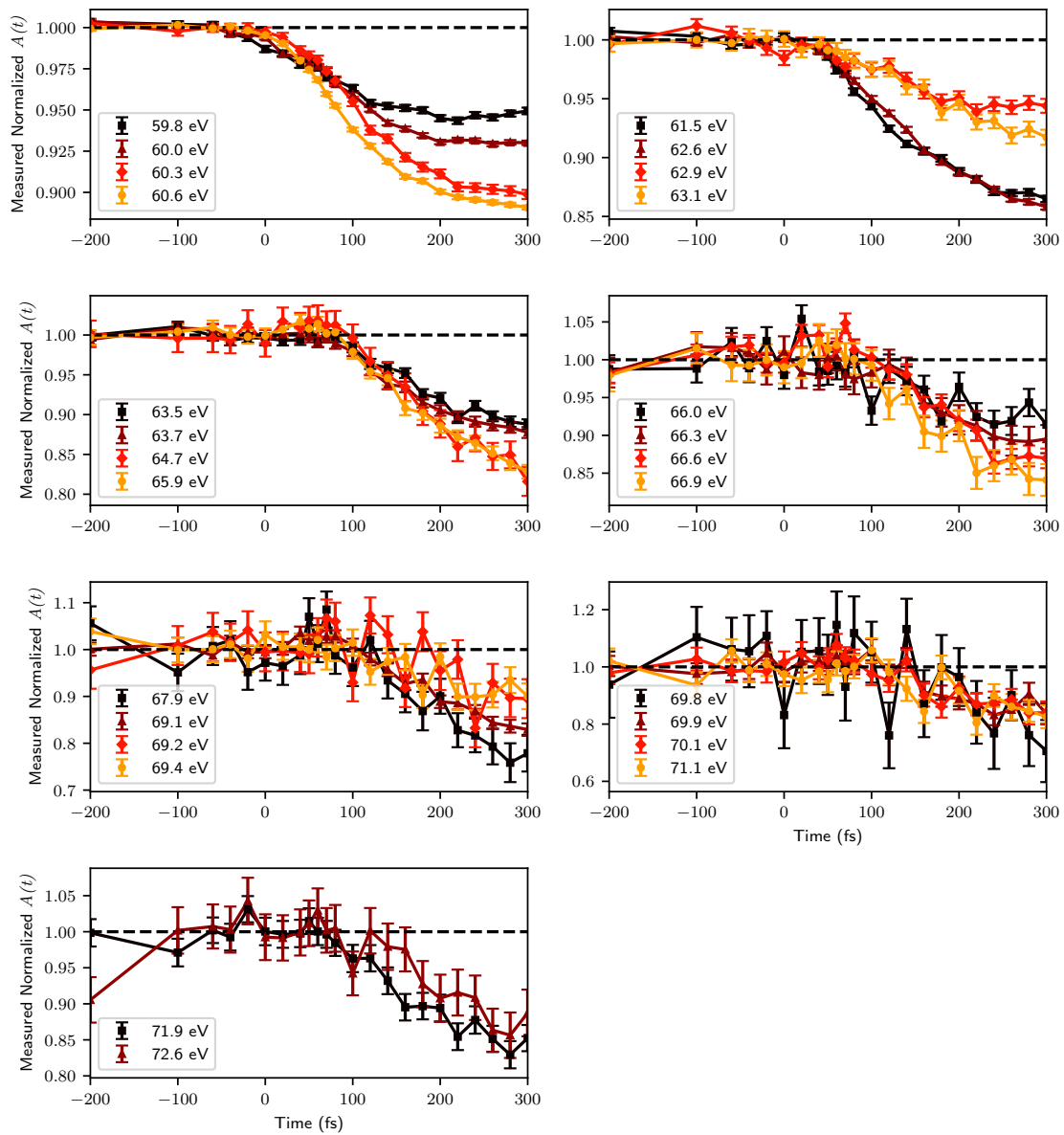


Figure 4.21: **Energy-dependent  $Co_2MnGe$  dynamics from to 42.6 eV to 57.3 eV.** The incident laser fluence was  $3.4 \text{ mJ/cm}^2$  corresponding to an absorbed fluences of  $2.5 \text{ mJ/cm}^2$ .

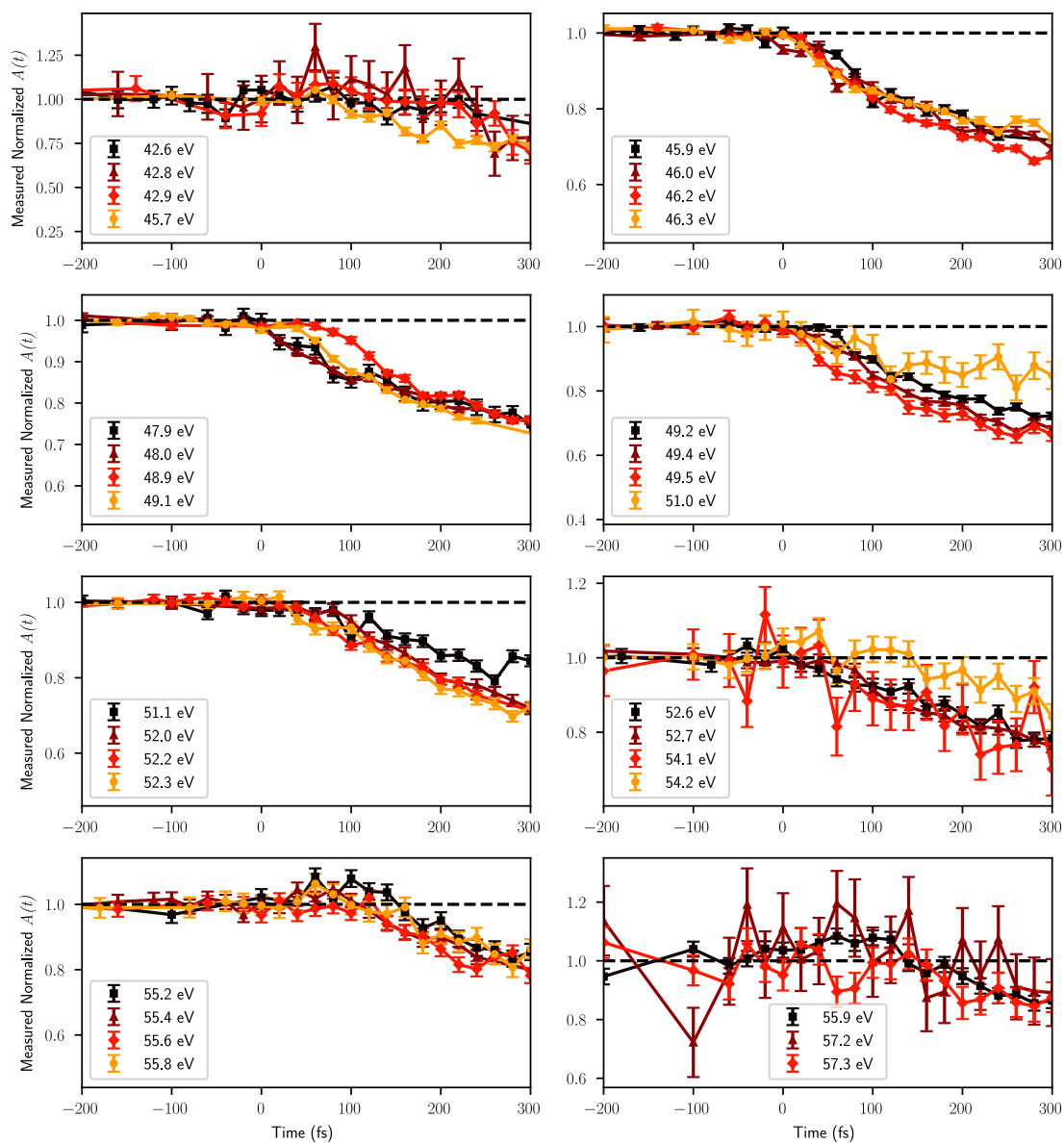


Figure 4.22: **Energy-dependent  $Co_2MnGe$  dynamics from to 58.3 eV to 71.4 eV.** The incident laser fluence was  $3.4 \text{ mJ/cm}^2$  corresponding to an absorbed fluences of  $2.5 \text{ mJ/cm}^2$ .

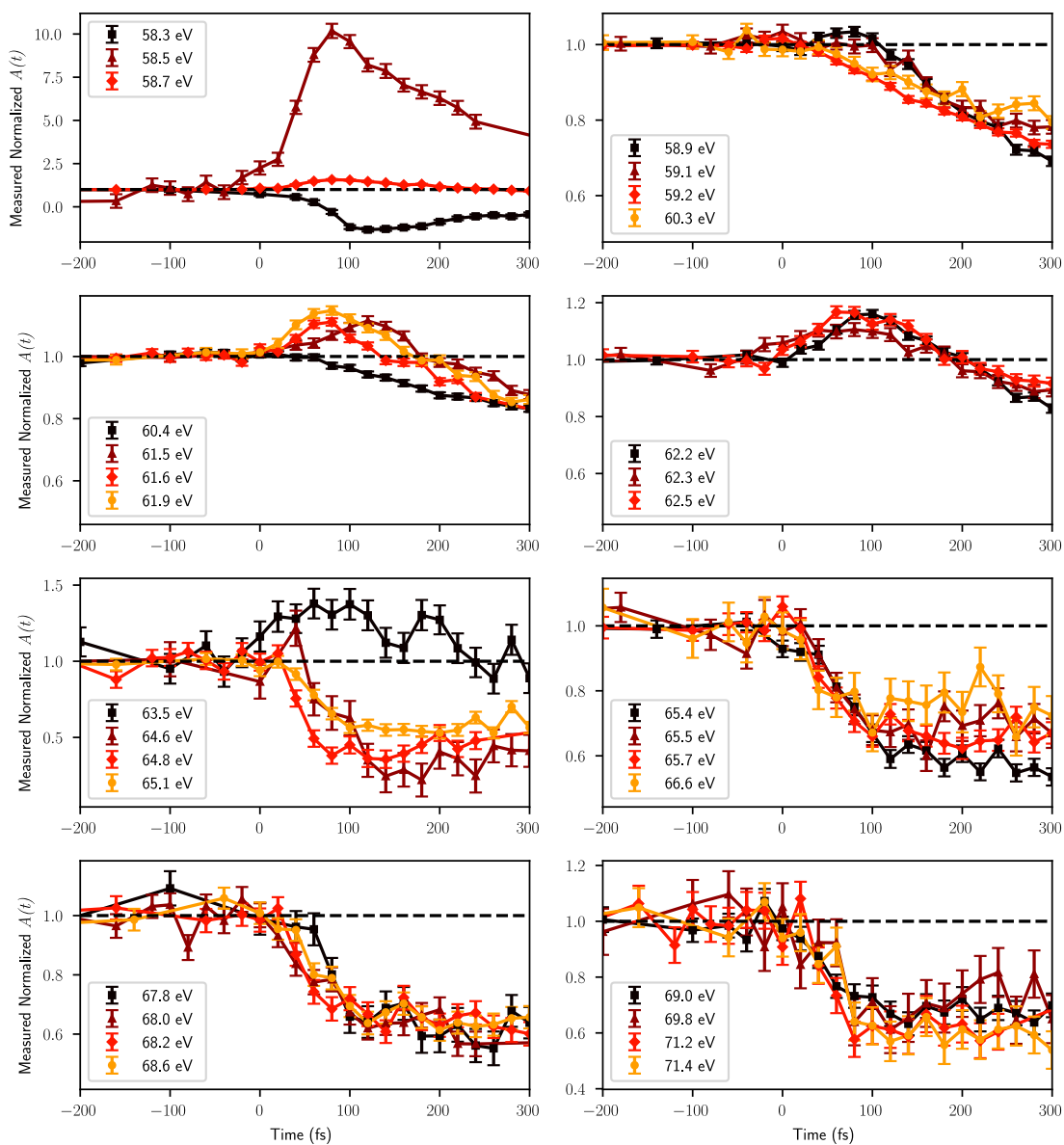
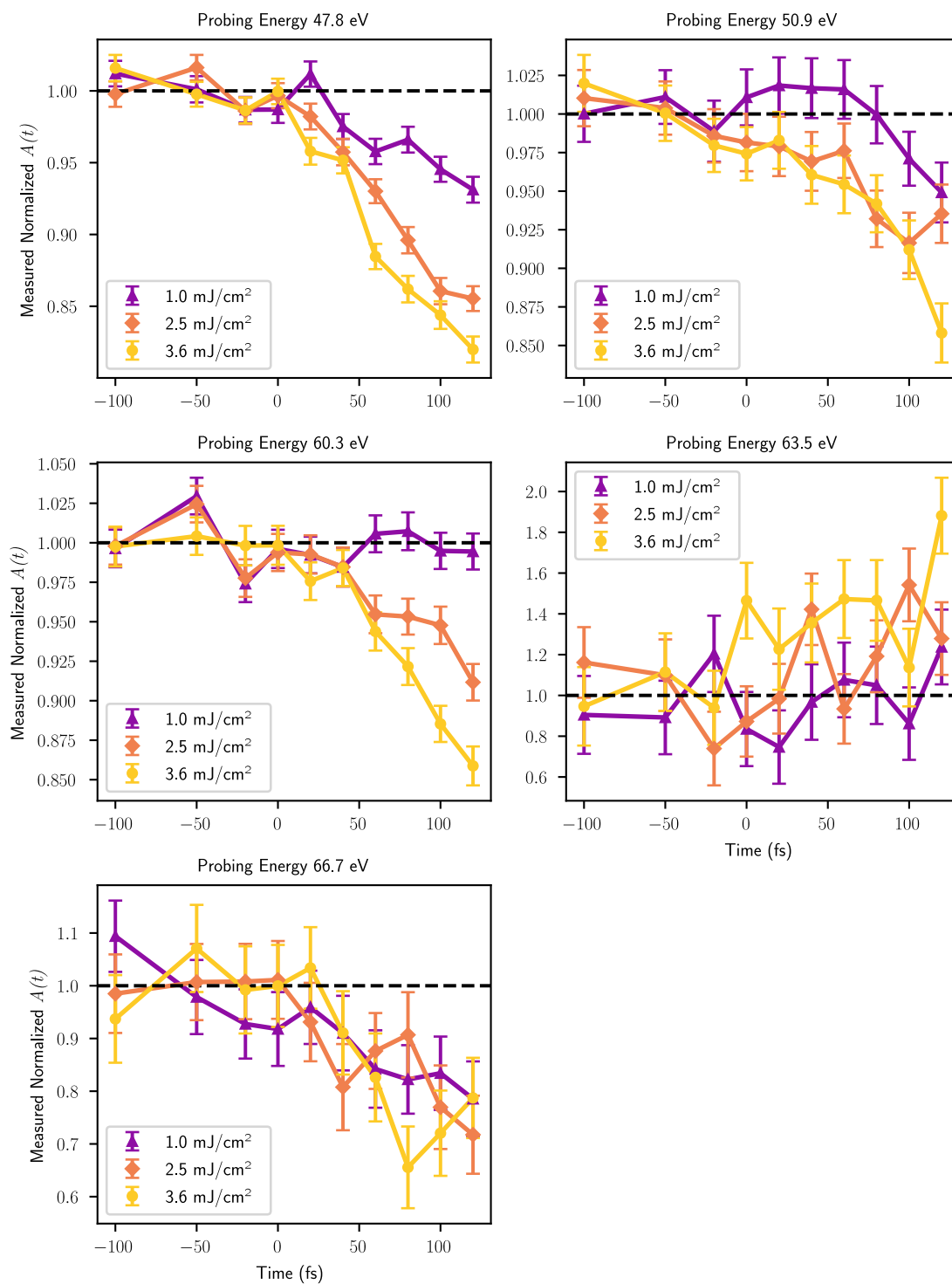


Figure 4.23: **Fluence- and energy-dependent  $Co_2MnGe$  dynamics.** The fluences given in the legend correspond to absorbed fluence values.



## 4.5 Experimental Design

Measurements were made at the X-MATTER beamline[87]. Ultrafast pulses from a regenerative Ti:Sapphire amplifier are split and simultaneously used as a  $\sim 800$  nm pump and EUV probe produced using HHG. The energy of the probe was tuned using a combination of three different methods: firstly, by tuning the central wavelength and bandwidth of the seed pulse into the amplifier; secondly, by applying gain flattening filters to the seed pulse to redshift the resultant amplified pulse; and thirdly, by applying chirp (second order dispersion) to the pulse to preferentially involve certain wavelengths in the high harmonic process. We note that small energy changes in the driving laser result in relatively much larger changes to the probe energy due to the additive nature of HHG. Since we do not have independent control over the pump pulse we must consider how this engineering of the driving laser impacts the pump parameters. The pump pulse compressibility is impacted when we detune from the amplifier's central energy using the three techniques described above. This results in a range of pump pulse durations from 40 fs to 55 fs depending on the required probe energy. Furthermore, the brightest wavelength of the pump exists in a range from 775 nm-805 nm depending on the required probe energy. Since these changes to the pump pulse are minimal, for the purpose of theory and interpretation, we use an 800 nm (1.55 eV) pump with a 45 fs duration for all calculations. However, we note that the experimental range of pump energies from 1.54 eV to 1.60 eV will have some impact on the allowable pump transitions, especially across the bandgap in the minority channel. The experimental time zero was determined by detecting any change in the magneto-optical signal that indicates the onset of the pump pulse. The entire harmonic comb is measured simultaneously by the CCD chip. This means that time-dependent data at both the Mn-edge, Co-edge, as well as all the energies in between, can be considered when determining time zero. A change in the magneto-optical signal (i.e. time zero) is defined as an increase or decrease (relative to the ground state) which falls outside the  $\pm 1$  standard deviation error bars for one or more of the harmonic orders. The theoretical time zero was chosen to maximize correspondence with the experimental data. The definition of the theoretical time zero relative to the pump pulse

is shown in the supplementary figures, Section 4.3.4, (Fig. 4.12). More specific details of the X-MATTER beamline are described in our recent design paper[87], and a brief schematic appears in the supplementary figures, Section 4.3.4, Fig. 4.6.

## 4.6 Future Work

We have recently received heterostructure samples where a  $Co_2MnGa$  layer is magnetically coupled to a thin  $Ni$  layer. These samples were grown by Dr. Edouard Lesne from the Max Planck Institute for Chemical Physics of Solids. This project will build on the work of Turgut *et al.*[16] who studied transient superdiffusive spin currents pumped between thin  $Ni$  and  $Fe$  layers. In Turgut *et al.*'s study, the MOKE signal of the  $Fe$  layer could be transiently enhanced or reduced by injecting a spin current generated by ultrafast excitation in the  $Ni$  layer above. The  $Fe$  MOKE signal either transiently increased or decreased depending on whether the  $Ni$  and  $Fe$  were coupled ferromagnetically or antiferromagnetically. We have designed the samples with different thicknesses of the  $Cu$  spacer layer (1-2  $nms$ ) to induce both ferromagnetic and antiferromagnetic coupling based on the RKKY interaction. The samples consist of  $Co_2MnGa/Cu/Ni/Si$  where  $Si$  is the capping layer. The  $Co_2MnGa$  is 20  $nm$  thick which is the minimum thickness in which the  $L2_1$  phase can be grown. The  $Ni$  layer is 5  $nm$ . The  $Ni$  layer is kept thin to allow the probe to penetrate through to the  $Co_2MnGa$  layer underneath. The purpose of this sample series is to observe laser induced superdiffusive spin currents being pumped from the  $Ni$  layer into the  $Co_2MnGa$  layer. The use of  $Co_2MnGa$  will be especially interesting for this study as its half-metallicity will make it a highly spin-selective acceptor of current. Therefore, the spin transport should be very different when comparing the ferromagnetically coupled heterostructure to the antiferromagnetically coupled heterostructure. Furthermore,  $M$ -edge TMOKE measurements should be able to probe the  $Ni$ ,  $Co$  and  $Mn$ -edges simultaneously to build a very detailed picture of the spin transport dynamics.

## 4.7 Conclusion

This chapter provides a valuable insight into the much debated topic of spin-transfer effects in Heuslers. We present a unified theoretical and experimental demonstration of spin-transfer signatures across the  $M$ -edges of  $Co$ ,  $Co_2MnGa$  and  $Co_2MnGe$ . This is the first study of spin-transfer on  $Co_2MnGa$  and the best energy and time-resolution ever presented for ultrafast measurements of each of the three samples. Furthermore, we have performed the first fluence-dependent measurements of the OISTR effect. Interestingly, the OISTR effects appear to saturate at much lower fluences than those predicted by theory. The  $Co_2MnGa$  sample showed very strong enhancements across the entire  $Co$   $M$ -edge. The enhancement signature was very large compared to what has been measured in previous studies of other alloys. We note that the  $Co_2MnGa$  sample shows an excellent level of agreement between measurements and TD-DFT simulations. Uniting theory and experiment allowed us to disentangle microscopic contributions from both intersite and intrasite spin-transfers as well as spin-flips. Conversely, the agreement between TD-DFT and EUV TMOKE measurements of  $Co$  and  $Co_2MnGe$  were more limited.

We note that the amplitudes of the transient TMOKE enhancements are extremely energy-dependent for all three samples. Therefore, conclusions about the strength of spin-transfers cannot necessarily be drawn from a measurement with a single probing energy. We note a general trend across many studies (including the three materials in this study) where there is a region of enhancement just above the  $M$ -edge zero-crossing. This enhancement is most likely caused by edge-shifting effects and not by spin-transfers. The measured enhancements of  $Co_2MnGe$  and  $Co$  were fewer, and smaller, than what was predicted. The differences were attributed to decreased lifetimes for excited spins in the  $Co$  and  $Co_2MnGe$  samples relative to the  $Co_2MnGa$  sample. We hypothesize that the  $Co_2MnGe$  enhancements were weaker due to the proximity of the excited states to the Fermi energy where SOC is stronger.

## Chapter 5

### Spin Reorientation Transitions

$TbMn_6Sn_6$  (Tb166) is a ferrimagnetic material which exhibits a highly unusual phase transition near room temperature where spins remain collinear while the total magnetic moment rotates from out-of-plane to in-plane. The mechanisms of this phenomenon have been studied in the quasi-static limit and the reorientation has been attributed to the competing anisotropies of  $Tb$  and  $Mn$ , whose magnetic moments have very different temperature dependencies. In this chapter, I present the first study of  $TbMn_6Sn_6$  to measure the spin-reorientation transition on its intrinsic timescales. We identify a range of fluence-dependent behaviors that display competing timescales between the spin-reorientation and the dissipation of thermal energy from the spin bath. By comparing experimental measurements with a theoretical model, the mechanism and timescales are explored.

#### 5.1 Introduction

##### 5.1.1 Introduction to Tb166

There has been a recent increase in interest in the field of ferrimagnetic spintronics[155], as well as ferrimagnetic spin reorientations, due to the potential application in stress-mediated magnetoelectric memory cells (MELRAMs)[156, 157]. A recent study[158] of the Kagome ferrimagnet,  $TbMn_6Sn_6$ , has extensively investigated the nature of its spin reorientation transition at 309 K ( $T_{SR}$ ), Fig. 5.1(c). Kagome refers to the lattice structure of corner-sharing triangles which resembles interwoven stars, Fig. 5.1 (b). Ferrimagnetic refers to the anti-parallel alignment of rare-Earth Terbium atoms and transition metal Manganese atoms within the material. As the temperature

is increased through  $T_{SR}$ , the magnetic moment rotates from out-of-plane to in-plane due to the competing anisotropies of the  $Tb$  and  $Mn$  magnetic sublattices.  $TbMn_6Sn_6$  has also generated recent interest because it may support quantum-limit Chern topological magnetism[159].

In this chapter, through joint measurement and modeling, we will identify the underlying timescales of ultrafast anisotropy-dependent spin reorientation and demagnetization in  $TbMn_6Sn_6$ .

Spin reorientations have been studied for many years: the first phenomenological model of spin reorientations due to temperature-dependent anisotropy was proposed in 1968[160]. The spin reorientation transition is a first-order phase transition where, when the temperature is increased above  $T_{SR}$ , the magnetic moments spontaneously rotate from out-of-plane to in-plane. The ferrimagnetism is governed by an indirect exchange between  $Mn$  moments mediated by anti-aligned  $Tb$  moments. The spin reorientation arises due to the competing anisotropy of the  $Tb$ , which has easy-axis anisotropy, and the  $Mn$  which has easy-plane anisotropy[158]. As the sample is heated towards the Curie temperature,  $T_C$ , the  $Tb$  moment drops off more rapidly than the  $Mn$  moment. This is because the ferromagnetic indirect  $Mn - Mn$  exchange produces a stronger molecular field than the molecular field that is experienced by the  $Tb$  moments. Resultantly, at temperatures in the range of 100 K below the Curie temperature (i.e  $T_{SR}$ ), the  $Mn$  anisotropy out-competes the  $Tb$  anisotropy and this spontaneously pulls the magnetic moment in-plane, while preserving the ferrimagnetic alignment between the  $Tb$  and  $Mn$  spins.

3d transition metals (TMs) have been measured to have very fast, few 100 fs, demagnetization rates[7, 44]. However, 4f rare-Earth magnets (REs) demagnetize at a much slower rate in a two-step process[44, 161]. For example, both  $Gd$  and  $Tb$  initially demagnetize at a rate of 750 fs followed by a much slower secondary demagnetization with a rate of, 40 ps for  $Gd$ , and 8 ps for  $Tb$ [161] respectively. However, demagnetization times of RE moments in RE-TM alloys can be as fast as those of pure TMs[162]. Several studies have investigated the ultrafast demagnetization of multi-element alloys containing both RE and TM magnetic sublattices[162, 163, 67]. It has been proposed that the ferrimagnetic alignment of the magnetic sublattices in RE-TM alloys allows spin angular momentum to be transferred between the 3d and 5d moments leading to a faster demagnetization of both the RE

and the TM[164]. Due to this mechanism, demagnetization times for RE-TM alloys were found to be fastest when the excitation brought the system in the vicinity of the compensation temperature ( $T_{comp}$ ), where the RE and TM moments are equal and opposite, rather than the Curie temperature ( $T_C$ )[162] -where we might expected demagnetization to be maximal. In  $TbMn_6Sn_6$ , there is no compensation temperature. This is because the  $Mn$  sublattice always carries a higher moment[158], due to the 6:1 ratio of  $Mn$  atoms to  $Tb$  atoms (despite  $Tb$  carrying a larger magnet moment per atom). Nevertheless, we may expect demagnetization times for Tb166 to be quite fast compared to pure  $Tb$ .

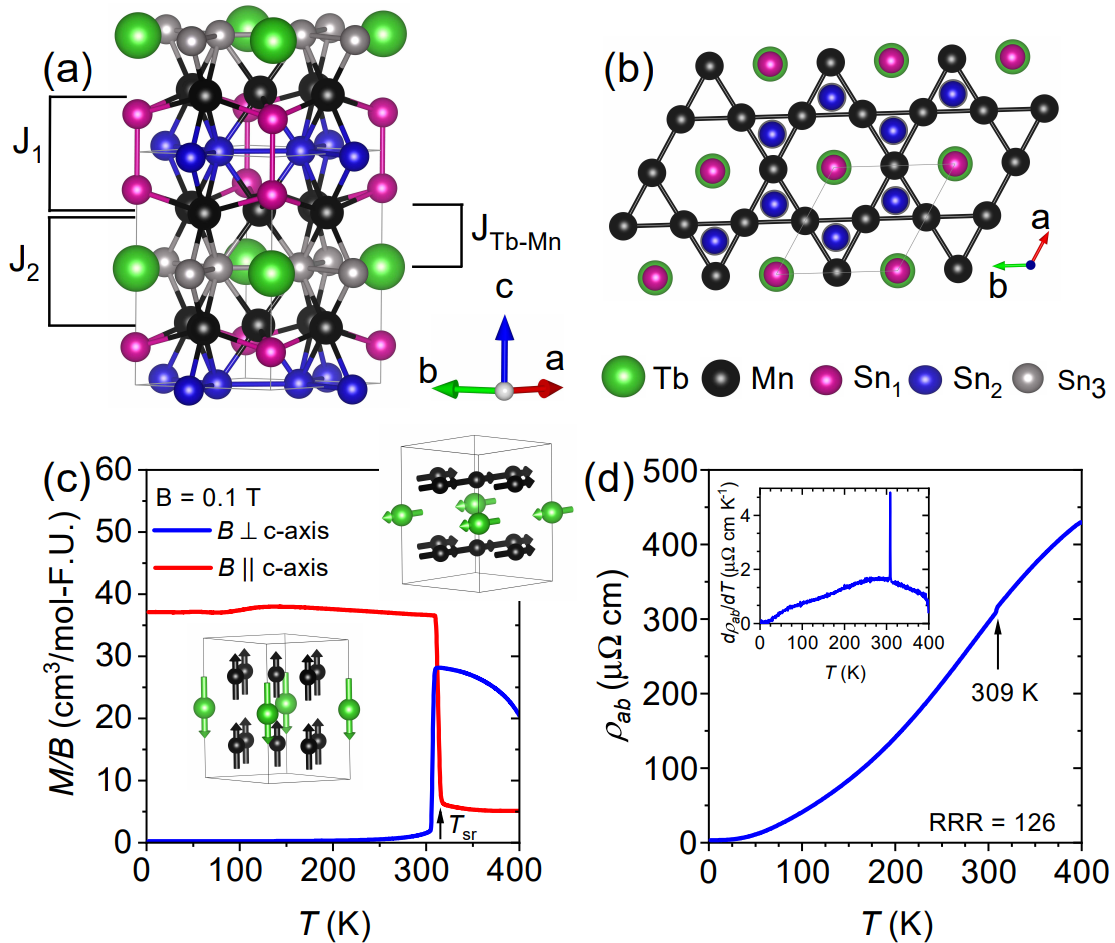
To determine the timescales of spin reorientation and demagnetization, measurements of time-dependent sample magnetism were performed at the X-MATTER beamline[87] in Boulder. A Ti: Sapphire regenerative amplifier was use to drive high harmonic generation (HHG) in a neon gas medium. This produced a comb of harmonic probing energies in the extreme ultraviolet (EUV) range. Energies in the HHG comb were spectrally dispersed using a diffraction grating and the intensities were recorded on a CCD chip. The EUV light resonantly probed the in-plane  $Mn$  moment at the  $M$ -edge (47.2 eV) using the transverse magneto-optical Kerr effect (TMOKE). Dynamics were measured stroboscopically using pump-probe techniques. Sample dynamics were excited using pulses from the Ti: Sapphire laser with a 780 nm central wavelength, 40 fs duration pulses and a 5 kHz repetition rate. The pump spot had  $1/e^2$  radii of 316  $\mu m$  by 535  $\mu m$ . The probe spot had a  $1/e^2$  radius of approximately 40  $\mu m$ .

The magnitude of the in-plane  $Mn$  magnetic moment was determined by calculating the TMOKE magnetic asymmetry which was based on differential intensity measurements with applied fields of  $185 \pm 15$  mT in-plane and a  $p$ -polarized incident beam at near-Brewster.:

$$A(t) = \frac{I_+(t) - I_-(t)}{I_+(t) + I_-(t)} \quad (5.1)$$

where  $A(t)$  is the magnetic asymmetry signal,  $I_+(t)$  is the time-dependent reflectivity of the sample with an applied field of +185 mT and,  $I_-(t)$  is the time-dependent reflectivity of the sample with an

Figure 5.1: **Introduction to  $TbMn_6Sn_6$ .** Figure reproduced from [158]. (a) The crystal structure of  $TbMn_6Sn_6$ .  $J_1$  and  $J_2$  represent exchange constants between different layers of  $Mn$  while  $J_{Tb-Mn}$  is the exchange constant between the  $Mn$  and  $Tb$  layers. (b) The Kagome lattice. This is a top view of the crystal depicted in (a). (c) The sample magnetization,  $M$ , measured along two different axes, normalized by the applied field  $B$  as a function of temperature. The applied field is  $0.1 T$ . The in-plane and out-of-plane signals change rapidly as the sample goes through the spin-reorientation transition. The  $Tb$  and  $Mn$  spin orientations before and after spin-reorientation are shown in the two inset diagrams. (d) The electrical resistivity as a function of temperature. The spin-reorientation appears as a small kink in the resistivity curve at  $309 K$ . The inset shows the temperature derivative of the resistivity. The spin reorientation creates a large spike.



applied field of  $-185 \text{ mT}$ . More details of the magnetic asymmetry measurement and the X-MATTER beamline appear in Section 3.1 and Johnsen *et al.*[87]

Single crystals of  $TbMn_6Sn_6$  were grown by self-flux methods as described by Jones *et al.*[158]. The magnetic asymmetries measured on this sample were, approximately, 10 – 100 times smaller than many typical samples conventionally measured with EUV TMOKE (e.g. Fe, Ni, Co, Py, etc.). These measurements were made possible by the excellent stability of the X-MATTER beamline[87].

### 5.1.2 Introduction to Magnetic Switching and Spin Precession

Magnetization reversal refers to the process by which a sample magnetization,  $\mathbf{M}$ , rotates  $180^\circ$  from one stable orientation along the easy-axis to a stable anti-parallel orientation along the easy axis. This process is of particular relevance to magnetic storage where bits must be written accurately and efficiently to a disk. For example, in the case of perpendicular magnetic recording (PMR), bits within the magnetic platter must be magnetized in the up or down direction using an electromagnetic writing element.

The torque  $\mathbf{T}$  on a magnetic dipole moment  $\mathbf{m}$  in a field  $\mathbf{H}$  is given by:

$$\mathbf{T} = \mathbf{m} \times \mathbf{H} \quad (5.2)$$

One might assume the most efficient way to switch the magnetization is to apply a field  $\mathbf{H}$  anti-parallel to the magnetization direction. However, based on the cross-product in Eq. 5.2, applying  $\mathbf{H}$  anti-parallel to  $\mathbf{m}$  exerts no torque. Therefore, magnetic switching can only occur when a thermal excitation moves  $\mathbf{m}$  and a finite torque can be generated[36]. This problem can also be overcome by applying the field very slightly off-axis. Another important feature of Eq. 5.2, is that the generated torque is perpendicular to both  $\mathbf{H}$  and  $\mathbf{m}$ . This means that the magnetization will not rotate directly to the final state, but rather it will undergo a precessional motion which will decay to the final state only in the presence of damping.

The equation of motion is given by:

$$\frac{d\mathbf{m}}{dt} = \gamma[\mathbf{m} \times \mathbf{H}] = \gamma \mathbf{T} \quad (5.3)$$

where  $\gamma$  is the gyromagnetic ratio, which for an electron has a value equal to  $-eg\mu_0/2m_e$ ,  $e$  is the electric charge of an electron,  $m_e$  is the mass of an electron,  $g$  is the relativistic g-factor and has a value roughly equal to 2, and  $\mu_0$  is the Bohr magneton. This equation of motion gives us the Larmor precession,  $\omega$ :

$$\omega = -\gamma H \quad (5.4)$$

In the situation where the precession is damped, we can utilize the Landau-Lifshitz (LL) equation where:

$$\frac{d\mathbf{m}}{dt} = -\gamma(\mathbf{m} \times \mathbf{H}) - \frac{4\pi\mu_0\lambda}{m^2}(\mathbf{m} \times (\mathbf{m} \times \mathbf{H})) \quad (5.5)$$

where  $\lambda$  is the relaxation frequency which defines the rate of damping and has the units of  $s^{-1}$ . It is helpful to think of this equation in terms of a damping term,  $\alpha$ , whose value can be determined phenomenologically:

$$\alpha = 4\pi\mu_0 \frac{\lambda}{\gamma m} \quad (5.6)$$

Which gives a new form of the LL equation:

$$\frac{d\mathbf{m}}{dt} = -\gamma(\mathbf{m} \times \mathbf{H}) - \frac{\alpha\gamma}{m}(\mathbf{m} \times (\mathbf{m} \times \mathbf{H})) \quad (5.7)$$

Understanding the exact nature of the damping term is still an open question in magnetism research. The damping term could be explained by considering that angular momentum is transferred into induced eddy currents. However, this formulation is poor at describing thin films where eddy currents are suppressed but significant damping still occurs[165]. Other descriptions include the transfer

of angular momentum via the excitation of spin waves or magnons, scattering with impurities and phonons, or spin-orbit coupling based spin-flips. In all cases, the angular momentum of the spin system must be transferred to the lattice in order for the precession to decay.

The Landau-Lifshitz (LL) equation as expressed in Eq. 5.7 makes a specific assumption, that  $\alpha \ll 1$ . Otherwise, the damping will not only act on the precessional motion, but also the motion that was induced by the damping. The full equation without assumptions takes the following form:

$$\frac{d\mathbf{m}}{dt} = -\gamma(\mathbf{m} \times (\mathbf{H} - \frac{\alpha}{\gamma m} \frac{d\mathbf{m}}{dt})) \quad (5.8)$$

This was shown by Gilbert and Kelley and is most often referred to as the Landau-Lifshitz-Gilbert equation (LLG). The LLG equation can be solved analytically for a static field,  $\mathbf{H}$ , applied along the negative  $z$ -direction. To solve, we first separate the equation into Cartesian co-ordinates:

$$\begin{aligned} \frac{dm_x}{dt} &= \omega_0 m_y + \alpha \frac{m_y}{m_s} \frac{dm_z}{dt} - \alpha \frac{m_z}{m_s} \frac{dm_y}{dt} \\ \frac{dm_y}{dt} &= -\omega_0 m_x + \alpha \frac{m_z}{m_s} \frac{dm_x}{dt} - \alpha \frac{m_x}{m_s} \frac{dm_z}{dt} \\ \frac{dm_z}{dt} &= \alpha \frac{m_x}{m_s} \frac{dm_y}{dt} - \alpha \frac{m_y}{m_s} \frac{dm_x}{dt} \end{aligned} \quad (5.9)$$

Solving these coupled equations gives the following result:

$$\begin{aligned} m_x &= m_s \sin\theta e^{i\omega t} \\ m_y &= m_s \sin\theta e^{i\omega t + i\pi/2} \\ m_z &= m_s \cos\theta \end{aligned} \quad (5.10)$$

where  $\theta$  is a function of time and depends on the initial condition of the magnetization orientation,  $\theta_0$ , as described below:

$$\tan \frac{\theta}{2} = \tan \frac{\theta_0}{2} e^{-t/\tau}. \quad (5.11)$$

The angular frequency,  $\omega$ , is an augmented version of the Larmor frequency,  $\omega_0$ :

$$\omega = \frac{\omega_0}{1 + \alpha^2}. \quad (5.12)$$

The time constant,  $\tau$ , is given by the following expression:

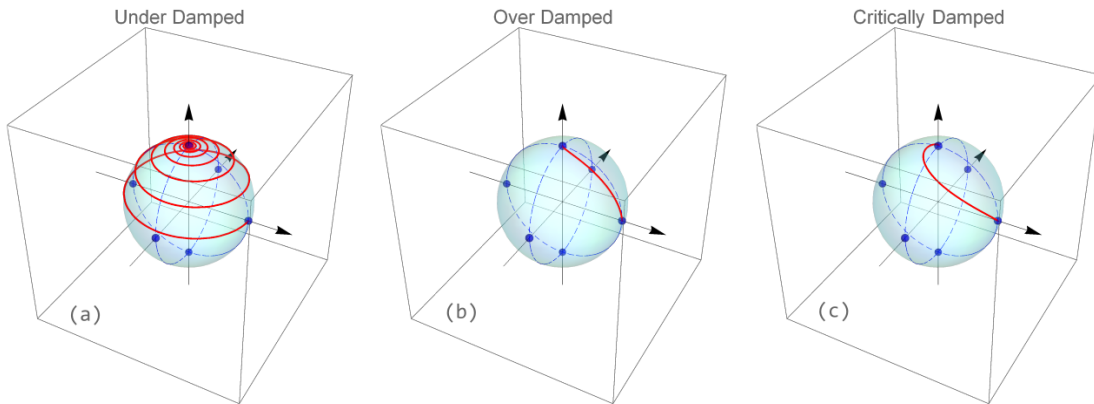
$$\tau = \tau_0(1 + \alpha^2) \quad (5.13)$$

where  $\tau_0$  is given by:

$$\tau_0 = \frac{1}{\alpha\omega_0}. \quad (5.14)$$

Critical damping occurs when  $\alpha=1$ . Based on the solutions given in Eq. 5.10 we plot three different regimes: under damped, over damped, and critically damped, Fig. 5.2. For real ferromagnets,  $\alpha$  typically takes a value between 0.1 and 0.01.

Figure 5.2: **Spin dynamics modeled with an numerical solution to the Landau-Lifshitz-Gilbert equation.**(a) Underdamped, (b) overdamped and (c) critically damped.



In the modeling of Tb166, a numerical solution of the the LL equation will be implemented as the equations are too complex to be solved analytically. We will incorporate a sample shape-dependent demagnetizing field and a time-dependent anisotropy field that changes with sample temperature, as well as a temperature-dependent saturation magnetization.

## 5.2 Results

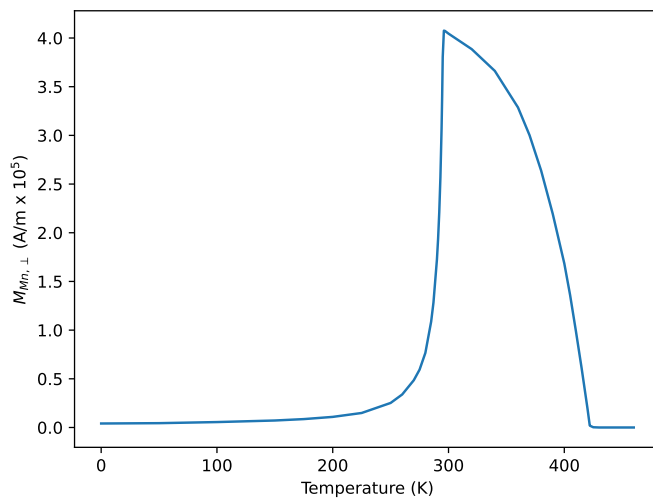
### 5.2.1 In-plane $Mn$ Moment

The relationship between the in-plane  $Mn$  magnetization and temperature is given in Fig. 5.3. The figure was constructed using the temperature-dependent magnitudes of the  $Mn$  and  $Tb$  magnetic moments from 0- 500  $K$  that were determined by neutron scattering[166]. This information was combined with the temperature-dependent anisotropies from Jones *et al.*[158] to calculate the in-plane Mn magnetization with temperature. In this figure, an in-plane applied field of 185  $mT$  in the  $+x$  direction was included to match the experimental conditions. The TMOKE measurement measures the in-plane  $Mn$  magnetization and so this figure gives a guideline for interpreting the TMOKE signals. This figure reveals, if the measured TMOKE signal is zero or near-zero, this would indicate that the sample temperature could either be in the low temperature regime, below  $T_{SR}$ , or the high temperature regime above  $T_C$ . In the first instance, the total moment is still large but points out-of-plane, and in the second instance, the total moment is zero. In the model, the temperature-dependent total moment of the sample is calculated by multiplying the  $Mn$  atomic moment by six (because there are six  $Mn$  atoms per unit cell) and subtracting the  $Tb$  atomic moment (because it is anti-aligned with  $Mn$ ).

### 5.2.2 Sample Temperature

The sample was mounted on a 0.5  $mm$  thick sapphire plate using a conductive silver epoxy (EPO-TEK® H20S). No active heating or cooling systems were applied to the sample. Sample temperatures were recorded using an in-vacuum thermocouple wire mounted on the back of the sapphire sample mounting plate. The sample was magnetized with an applied field of  $185 \pm 15 mT$  using an out-of-vacuum GMW 5201 projection field electromagnet. The electromagnet was water cooled but still reached temperatures exceeding 40  $^{\circ}C$  during use. The sample was heated to above room temperature by thermal radiation from the electromagnet (situated behind the sample) and the pump laser (incident on the front of the sample). For each measurement, we allowed the sample

Figure 5.3: **The calculated in-plane projection of the  $Mn$  moment vs. temperature with an in-plane applied field of  $+185\text{ mT}$ .** Figure produced by combining anisotropy data from Jones *et al.*[158] and magnetic moment data from El-Idrissi *et al.*[166]. The in-plane Mn moment is maximized just above the spin reorientation temperature. The signal is small or zero below  $T_{SR}$  and above  $T_C$ .



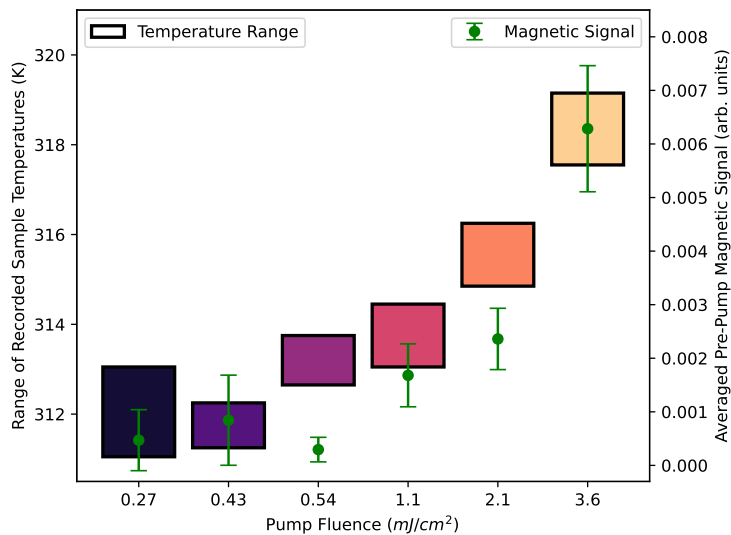
to the thermalize for approximately 1 hr with the same electromagnet currents and laser pump fluences used in the experiment in order for the sample to reach a stable baseline temperature. The electromagnet alone heated the sample to approximately 18  $K$  above room temperature ( $\sim 310 K$ ). The temperature rise induced by the pump laser was highly fluence-dependent. Measured sample temperatures varied from as high as 319  $K$  for the highest fluence ( $3.6 mJ/cm^2$ ) to 311  $K$  for the lowest fluence ( $0.27 mJ/cm^2$ ), Fig. 5.4. There was a small amount of ongoing thermalization that continued to increase the sample temperature throughout the scan after the 1 hr thermalization period. For this reason, we measured the temperature at the beginning (slightly lower temperature) and end of the scan (slightly higher temperature). These high and low temperatures set the upper and lower bounds of the bars in Fig. 5.4. Heating from the EUV probe is negligible.

The real sample temperature may differ slightly from the recorded temperature due to thermal gradients between the sample surface and the back of the sapphire plate where the temperature probe was mounted. Because the spin-reorientation transition is near room temperature, increasing the pump fluence led to a larger in-plane  $Mn$  moment in the pre-time-zero data (i.e. pre-pump excitation). This relationship is depicted in Fig. 5.4.

### 5.2.3 Fluence-dependent Dynamics

Fig. 5.5 shows the time-dependent magnetic asymmetry signal for a range of different pump fluences. A normalization factor was applied to each curve, which is explained in more details in Section 5.4, *Signal Normalization*. Data in Figs. 5.4, 5.5, and 5.6 are measured with a harmonic probing energy of  $46.2 \pm 0.2 eV$ . This harmonic was most resonant with the  $Mn$   $M$ -edge ( $47.2 eV$ ), and therefore, had the strongest TMOKE signal. While measurements at this energy are sensitive to the  $Mn$  behavior specifically, the  $Mn$  and  $Tb$  moments are expected to remain collinear[158]. The next harmonic (at  $49.5 \pm 0.2 eV$ ) was also strongly resonant with  $Mn$ -edge. The  $49.5 eV$  data is not presented (except in Fig. 5.7) as the signal-to-noise ratio was relatively poor due to it being further off-resonance from the  $Mn$   $M$ -edge. However, this harmonic showed similar dynamic behavior, as shown in Fig. 5.7. This indicates that the dynamic behavior is similar across the  $Mn$   $M$ -edge. This

Figure 5.4: **The relationship between the static (pre-pump) magnetic signal and the recorded sample temperature.** The magnetic asymmetry signals at a probe energy of  $46.2 \pm 0.2$  eV (green data points with error bars) were calculated by averaging the pre-pump-excitation data ( $t \leq 0$ ) for each fluence. As there were only 3 or 4 times points where  $t \leq 0$  for each fluence, in the dynamic measurements (Fig. 5.5), a student t-value weighting was multiplied with the standard error to obtain the error bars shown. The temperature ranges (solid color bars) indicate the maximum and minimum temperatures recorded by the temperature probe during the scan.



is to be expected for the 10's of picoseconds timescales in this study where the electronic and spin systems have had time to form a thermal distribution.

Fig. 5.5 shows the dynamic TMOKE asymmetry of  $TbMn_6Sn_6$ . When interpreting Fig. 5.5, it is important to note that there are two distinct temperature regimes where the signal will be zero. Below  $T_{SR}$  the signal is approximately zero. This is because we are only measuring only the in-plane component of the  $Mn$  magnetization and below  $T_{SR}$  the magnetization is out-of-plane. Above  $T_C$ , the signal is also zero because the magnetization vector is zero. To understand the fluence-dependent behavior, the results are divided in Fig. 5.5(a), the low fluence regime and Fig. 5.5(b), the high fluence regime.

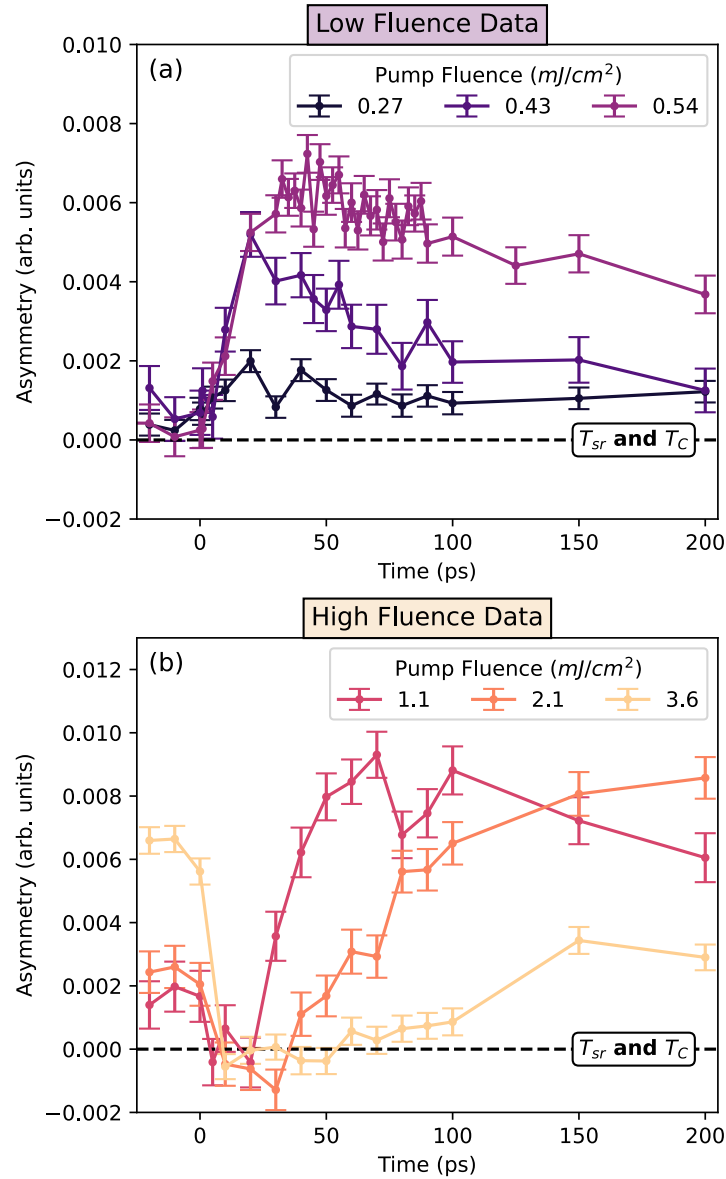
Fig. 5.5(a) depicts the dynamic behavior with low pump fluences. The signal can be broken down into three key steps:

1. Initially (pre-time-zero), the magnetization is mostly out-of-plane. The sample temperature hasn't exceeded  $T_{SR}$ . This means the measured in-plane signal is near zero.
2. Following time-zero (approximately 0-30  $ps$ ), ultrafast excitation from the pump laser partially sends the sample's spin system through the reorientation transition. The signal increases with time as spins rotate in-plane. The height of the TMOKE signal scales with the fluence applied because when the sample is pumped harder, it goes through the spin reorientation transition more completely, i.e. a greater portion of the sample is magnetized in-plane.
3. Finally (approximately 30-200  $ps$ ), the sample cools off as heat is gradually dissipated to unpumped regions of the sample, the epoxy, and the sample mounting plate. The TMOKE signal is gradually reduced as spins cool and start to reorient back out-of-plane.

Fig. 5.5(b) depicts the high fluence data. The high fluence data can be broken down into four key steps:

1. The initial (pre-time-zero) temperature is warmer than for the low fluence data due to the sample thermalizing with a larger incident pump power. Therefore, a larger fraction of the  $Mn$  magnetic moment is initially in-plane. The relationship between pump fluence and initial signal magnitude is exemplified in Fig. 5.4.

Figure 5.5: **Fluence-dependent measured dynamic TMOKE asymmetries of the Tb166 in-plane  $Mn$  moment probed at  $46.2 \pm 0.2$  eV.** The measured magnetic asymmetry with an applied field of  $185 \pm 15$  mT with (a) low pump fluences and (b) the high pump fluences. Below  $T_{SR}$ , and above  $T_C$ , the signal is approximately zero because in both cases there is no in-plane component to the magnetization. This threshold is depicted by the black dotted line.



2. Ultrafast excitation demagnetizes the sample. The temperature of the spin system exceeds the Curie temperature.
3. The sample cools off and re-magnetizes in-plane as it transitions back below the Curie temperature but above  $T_{SR}$ . The largest fluence ( $3.6 \text{ mJ/cm}^2$ ) takes the longest time to recover and the smallest fluence ( $1.1 \text{ mJ/cm}^2$ ) takes the least time to recover.
4. This final step is only present in the  $1.1 \text{ mJ/cm}^2$  data. The sample cools further and as it approaches  $T_{SR}$  it starts to lose its in-plane moment in favor of an out-of-plane moment. The signal decreases.

In the  $3.6 \text{ mJ/cm}^2$  and  $2.1 \text{ mJ/cm}^2$  data, after the initial excitation, the spin temperature remains above  $T_{SR}$  until the end of the scan at  $200 \text{ ps}$ . Since the temperature does not fall below  $T_{SR}$ , there is no reorientation transition. The sample exceeds the Curie temperature following the rapid initial heating. The later dynamics come from the sample re-magnetizing in-plane as it dissipates heat. Therefore, the timescales of recovery come from the rate of heat dissipation from the probed region of the sample. The  $1.1 \text{ mJ/cm}^2$  data is the only fluence where we see signatures of both phase transitions ( $T_{SR}$  and  $T_C$ ). In the first  $20 \text{ ps}$ , the sample exceeds the Curie temperature and is demagnetized. The sample remagnetizes from  $20 \text{ ps}$  to  $60 \text{ ps}$ . However, after  $60 \text{ ps}$ , the signal starts to decrease. This indicates that the temperature in parts of the probed region have cooled below  $T_{SR}$ .

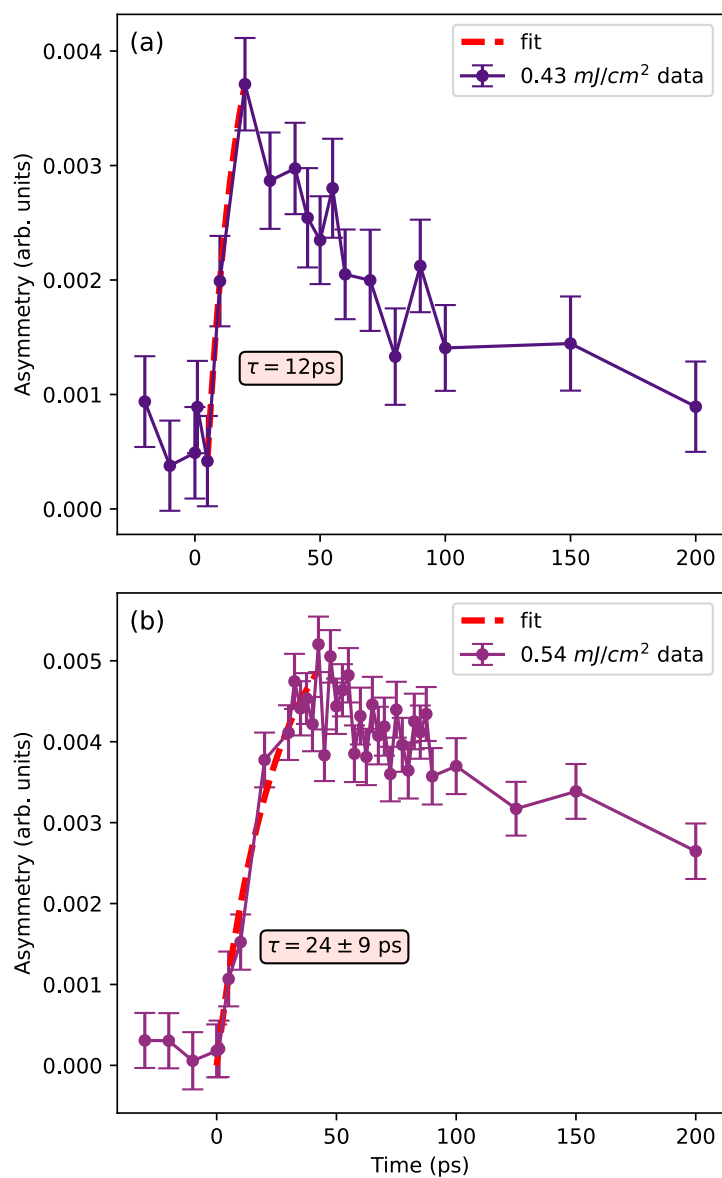
In the  $0.27 \text{ mJ/cm}^2 - 0.54 \text{ mJ/cm}^2$  data, the spin reorientation transition is addressed. The initial rise time is fitted in Fig. 5.6 and represents the spin reorientation response to a rapid anisotropy change through impulsive heating. The slow decay from  $30\text{-}200 \text{ ps}$ , represents the spin temperature relaxing which drives the spin orientation back out-of-plane.

In Fig. 5.6, we fit the low fluence data from Fig. 5.5 (a), with an exponential function of the form:

$$A(t) = C[1 - e^{-\frac{t-t_0}{\tau}}] \quad (5.15)$$

where  $A(t)$  is the measured magnetic asymmetry signal,  $C$  is the amplitude,  $t$  is time,  $t_0$  is an offset

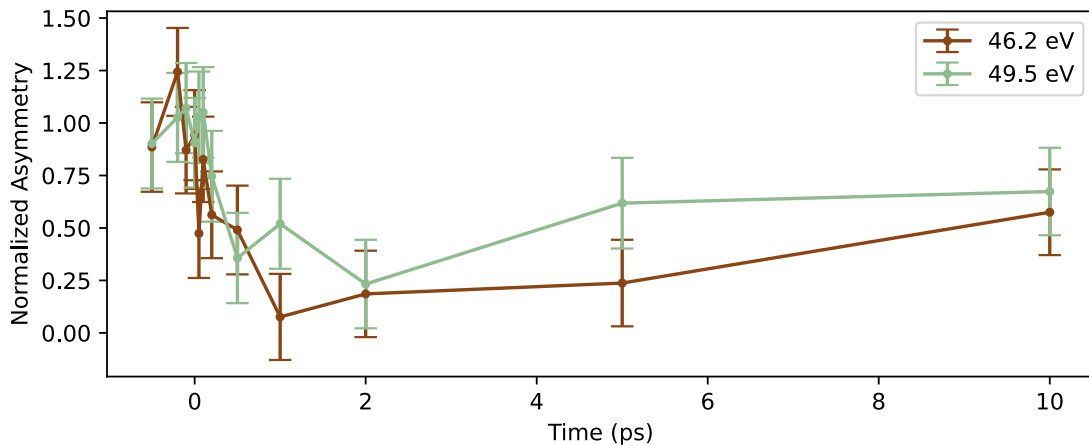
Figure 5.6: **Exponential fit of the experimental spin reorientation.** The rise time of the spin reorientation at (a)  $0.43 \text{ mJ/cm}^2$  and (b)  $0.54 \text{ mJ/cm}^2$  were fitting using Eq. 5.15.



to account for any differences between the time-zero as defined in the figure and the time-zero determined by the fit.  $\tau$  is the time-constant of the exponential fit. For the fitting process, data was truncated to include only the exponential rise (starting from lowest point and continuing to the highest point). Fits were performed using the `'curve_fit'` function from Python's SciPy package. The  $0.27 \text{ mJ/cm}^2$  data was not included as the signal-to-noise ratio was too poor to perform the fit. The  $0.43 \text{ mJ/cm}^2$  data is shown in Fig. 5.6. (a). A time-constant of  $12 \text{ ps}$  was obtained. However, as only three data points were included in the fit, a confidence interval for the fitting parameters could not be established. For the  $0.54 \text{ mJ/cm}^2$  data, the fitted time-constant was  $24 \pm 9 \text{ ps}$ .

Therefore, the spin reorientation timescale is very fast,  $\sim 20 \text{ ps}$ . We attribute this to the very large anisotropy energies present in Tb166. By comparison, ultrafast demagnetization is, perhaps, the fastest magnetic phase transition found in nature. In Fig. 5.7, a measurement of sample demagnetization with a  $1.1 \text{ mJ/cm}^2$  fluence is depicted with additional time resolution in the first  $10 \text{ ps}$ . The average pre-time-zero signal is normalized to one. Two different probing energies near the *Mn M*-edge are given. The timescale for demagnetization is approximately  $1 \text{ ps}$ . This is approximately 20 times faster than the reorientation timescale.

Figure 5.7: **Ultrafast demagnetization of Tb166 with  $1.1 \text{ mJ/cm}^2$  pump fluence.** Dynamic asymmetries from  $-0.5$  to  $10 \text{ ps}$  as measured with harmonic probing energies centered at  $46.2 \pm 0.2 \text{ eV}$  and  $49.5 \pm 0.2 \text{ eV}$ . Demagnetization is an order of magnitude faster than the spin reorientation timescale.



### 5.2.4 Building a Model of Tb166

To model the spin reorientation transition, we will adapt the equations from Section 5.1.2: *Introduction to Magnetic Switching and Spin Precession*. The first step is the construction of a time-dependent effective field,  $\mathbf{H}_{\text{eff}}(t)$ , which will act on the sample's magnetization unit vector,  $m$ , in the LL equation:

$$\mathbf{H}_{\text{eff}}(t) = \mathbf{H}_{\text{appl}} + \mathbf{H}_{\text{demag}}(t) + \mathbf{H}_{\text{anis}}(t) \quad (5.16)$$

where  $\mathbf{H}_{\text{appl}}$  is a constant applied field in the  $+x$  direction with a value of  $185 \text{ mT}$ . The demagnetizing field,  $\mathbf{H}_{\text{demag}}(t)$ , is much weaker than the anisotropy field and does not have a large impact on the dynamics. To calculate an approximate demagnetizing field, we approximate the sample as a cylinder. The height of the sample is  $0.7 \text{ mm}$  and the diameter is  $3.3 \text{ mm}$  at its widest and  $1.9 \text{ mm}$  at its narrowest. I approximate this as a cylinder with a diameter four times its height. I then use an approximation[167] for the demagnetizing factors,  $N_{x,y,z}$ :

$$N_x = N_y = \frac{2n/\sqrt{\pi}}{4n/\sqrt{\pi} + 1}, N_z = \frac{1}{4n/\sqrt{\pi} + 1} \quad (5.17)$$

where the cylinder has a radius,  $r$  and a length  $2nr$ . In this case,  $n = 1/4$ . The demagnetizing field is then:

$$\mathbf{H}_{\text{demag}}(t) = \begin{bmatrix} -0.18M_x(t) \\ -0.18M_y(t) \\ -0.64M_z(t) \end{bmatrix} \quad (5.18)$$

where  $M_{x,y,z}$  are the components of the magnetization projected along different axes. The individual components are time-dependent because they depend on both the magnitude of the saturation magnetization,  $M_s$ , as well as which direction it points, described by the unit vector  $\mathbf{m}(\mathbf{t})$ . The saturation magnetization depends on the temperature of the spin system, which in itself depends on time. Therefore, we write  $M_s$  as:  $M_s(T_{\text{spin}}(t))$ . The Cartesian components of the saturation

magnetization are given by a time-dependent projection,  $m_i(t)$ , of the magnetization unit vector along each axis  $i$ . Therefore, the components  $M_{x,y,z}$  are given by:

$$M_i(t) = m_i(t)M_s(T_{spin}(t)) \quad (5.19)$$

where  $i = x, y, z$ . The saturation magnetization is calculated based on the  $Mn$  and  $Tb$  moments:

$$M_s(T_{spin}) = (6mom_{Mn}(T_{spin}) - mom_{Tb}(T_{spin}))/V. \quad (5.20)$$

The  $Tb$  moment per atom,  $mom_{Tb}(T_{spin})$ , is subtracted due to its ferrimagnetic alignment with  $Mn$ . The  $Mn$  moment per atom,  $mom_{Mn}(T_{spin})$ , is multiplied by 6 as there are 6  $Mn$  atoms per unit cell. This is then divided by the volume of the unit cell,  $V$ , to convert to total magnetization.  $V$  is calculated based on the unit cell vectors given by Jones *et al.*[158], i.e.  $V = a^2c$  where  $a = 5.538 \text{ \AA}$  and  $c = 9.0326 \text{ \AA}$ .

$\mathbf{H}_{\text{anis}}(t)$  is an effective field which represents the torque exerted by the anisotropy field. This term will drive the temperature-dependent dynamics.  $\mathbf{H}_{\text{anis}}(t)$  is derived from the anisotropy energies of  $Mn$  and  $Tb$  and their respective moments. The  $Tb$  anisotropy energy is minimized out-of-plane while the  $Mn$  anisotropy energy is minimized in-plane. By approximating the anisotropy field with a second order expansion, we obtain:

$$\begin{aligned} E_{anis,Tb}(T_{spin}) &= -K_{Tb}(T_{spin})\cos^2(\theta), \\ E_{anis,Mn}(T_{spin}) &= -K_{Mn}(T_{spin})\sin^2(\theta) \end{aligned} \quad (5.21)$$

where  $K_{Tb}(T_{spin})$  and  $K_{Mn}(T_{spin})$  are temperature-dependent anisotropy coefficients extracted from Jones *et al.*[158]. The corresponding effective anisotropy field for each spin system,  $\mathbf{H}_{\text{anis},j}(t)$ , where  $j$  is either  $Tb$  or  $Mn$ , can be calculated by taking the vector gradient of the anisotropy energy, dividing by the volume averaged magnetic moment, and considering only terms that can exert a

torque[168]:

$$\mathbf{H}_{\text{anis},j}(T_{spin}) = -\nabla E_{\text{anis},j}(T_{spin}) / (mom_j(T_{spin})/V). \quad (5.22)$$

where  $mom_j(T_{spin})$  is the species specific, temperature-dependent, magnetic moment per unit cell. For the modeling of Tb166, we took the expression for  $\mathbf{H}_{\text{anis},j}$  and multiplied it by an additional factor of 1/2 (as compared to what is written in Eq. 5.22) to bring the results in keeping with the work of Jones *et al.*[158]. The discrepancy most likely arises from the definition of  $K$ . Values for the temperature-dependent magnetic anisotropy energies,  $E_{\text{anis},j}$ , are extracted from Jones *et al.*[158] and are given based on the total moment, rather than the element specific one. Therefore, in this case, we divide by  $M_s(T_{spin})$  instead of  $(mom_j(T_{spin})/V)$ . The temperature-dependent *Tb* and *Mn* magnetic moments come from neutron scattering data from El-Idrissi *et al.*[166]. This gives a final expression for  $\mathbf{H}_{\text{anis}}(t)$ :

$$\mathbf{H}_{\text{anis}}(t) = \begin{bmatrix} 0 \\ 0 \\ m_z(t) \left( \frac{K_{Tb}(T_{spin}(t))}{M_s(T_{spin}(t))} - \frac{6K_{Mn}(T_{spin}(t))}{M_s(T_{spin}(t))} \right) \end{bmatrix} \quad (5.23)$$

Writing the LL equation in full vector form, we then obtain:

$$\frac{d\mathbf{m}}{dt} = -\gamma \left( \mathbf{m} \times \begin{bmatrix} H_{\text{appl}} - 0.18M_x(t) \\ -0.18M_y(t) \\ H_{\text{anis}}(t) - 0.64M_z(t) \end{bmatrix} - \frac{\alpha\gamma}{m} \left( \mathbf{m} \times \left( \mathbf{m} \times \begin{bmatrix} H_{\text{appl}} - 0.18M_x(t) \\ -0.18M_y(t) \\ H_{\text{anis}}(t) - 0.64M_z(t) \end{bmatrix} \right) \right) \right) \quad (5.24)$$

The temperature of the sample magnetization, i.e. the spin bath temperature, is estimated based on three time-dependent exponential functions:

$$T_{spin}(t) = T_0 + A_1(1 - e^{-t/\tau_{rise}}) - A_2(1 - e^{-t/\tau_{decay1}}) - A_3(1 - e^{-t/\tau_{decay2}}) \quad (5.25)$$

where  $T_0$  is the initial temperature of the sample prior to pump excitation. The amplitude  $A_1$  represents the heating of the spin bath from the pump laser. The first timescale,  $\tau_{rise}$ , comes from the rate of energy transfer from the electrons (which are directly excited by the laser pulse) to the spin bath. This rate of energy transfer to the spin bath is estimated to be 1 ps, based on the rate of ultrafast demagnetization of this sample, as shown in Fig. 5.7. The second term, whose magnitude is given by  $A_2$ , represents the spin-lattice thermalization time. The spin-lattice thermalization reduces the spin bath temperature on a short timescale. Based on typical values for the three temperature model, this is estimated to be 3 ps. On a longer timescale, the spin-bath temperature is further reduced due to thermal diffusion. This is represented in the final term with amplitude  $A_3$ . The experimental TMOKE signals decay on timescales similar to the total scan time, i.e. 200 ps. Therefore,  $\tau_{decay2}$  time is estimated to be 200 ps. While this thermal model is a relatively simplistic interpretation of the evolving temperatures and heat capacities of the system, it is sufficient for recreating some of the characteristic behavior of the sample.

### 5.2.5 Modeling Results

We note that the LL equation, Eq. 5.24, is not valid near the Curie temperature[169]. This is because the LL equation assumes a constant length of the magnetization vector which will not be the case in the vicinity of the Curie point. To some extent, this is overcome by multiplying the final results by the temperature-dependent saturation magnetization based on the temperature profile chosen in Eq. 5.25. Furthermore, near the Curie temperature, the damping constant,  $\alpha$ , is no longer constant and becomes temperature-dependent. For example, transverse damping is enhanced by the thermal dispersion of magnetization[169]. To overcome this, a microscopic Landau-Lifshitz-Bloch (LLB) equation description was developed by Lyberatos and Guslienko[170] with the intention of describing magnetic writing of nanoparticles subject to pulsed laser heating in HAMR hard drives.

This implementation of the LLB equation is beyond the scope of this work. However, we can avoid implementing the LL equation near  $T_C$  by confining the simulations to lower temperature regimes.

The results are divided into low fluence and high fluence regimes. In the low fluence section, we remain at least 100  $K$  below  $T_C$  in all simulations. Furthermore, in all the simulations of Fig. 5.8 where we compare with experimental results directly, only an 8% change in the magnetization vector length was induced by the simulated temperature changes.

For the highest fluence experimental data,  $3.6 \text{ mJ/cm}^2$  and  $2.1 \text{ mJ/cm}^2$ , all measurements after  $t = 0$  are above  $T_{SR}$  so there is no reorientations. In this case, the LL or LLB equations are not required as there is no precessional motion to be modeled. The dynamics in the high fluence section are treated purely in terms of the change in  $M_s$  as a function of changing sample temperature.

The experimental data from a fluence of  $1.1 \text{ mJ/cm}^2$  is more difficult to model because, in this case, the sample passes through  $T_C$  on early timescales then reaches  $T_{SR}$  on longer timescales. Therefore, measurements are in the regime of  $T_C$  and will also require a precessional model for the near  $T_{SR}$  behavior. This data would be best modeled with the LLB equation and so we omit its treatment as it is beyond the scope of this work.

### 5.2.5.1 Low Fluence Modeling

In the model, spin reorientation occurs at a temperature of 302  $K$  with no applied field. This is based on extracting temperature-dependent anisotropies from figures of Jones *et al.*[158] and temperature-dependent spin moments from El-Idrissi *et al.*[166]. This is close to the literature value for spin reorientation of 309  $K$ [158], although the model is slightly on the lower side of the literature value. After including the applied in-plane field of 185  $mT$ , the spin reorientation occurs in the model at even lower temperatures. The in-plane moment exceeds the out-of-plane at temperatures as low as 294  $K$ . In the measured data, with an applied field of 185  $mT$ , the pre-time-zero in-plane moment remains relatively small for all fluences except for the highest,  $3.4 \text{ mJ/cm}^2$ , Fig. 5.5. This implies that the experimental spin-reorientation occurs the range of 315-319  $K$ , e.g. up to 10  $K$  higher than the literature value (even with the applied field of 185  $mT$ ). The measured sample

temperature may not fully agree with the real sample temperature based on the location of the temperature probe. This is discussed in more details in Section 5.2.2. Since the spin-reorientation temperature is lower than expected in the model, and higher than expected in the experiment, we will use a lower initial temperature in the model than the temperatures that were measured in the experiment. By beginning the model at a lower temperature, we can still investigate the dynamics of an ultrafast excitation through  $T_{SR}$ .

The time-dependent LL equation, Eq. 5.24, is solved using MATLAB's *ode45* which is a built-in non-stiff differential equation solver. To obtain the final comparison with experiment, the  $x$ -component of the time-dependent magnetization vector,  $m_x(t)$ , obtained from the time-evolution of Eq. 5.24, is multiplied by the calculated temperature-dependent  $Mn$  magnetization. This aligns the simulation with the experiment since the TMOKE measurement only measures the  $x$ -component of the  $Mn$  moment.

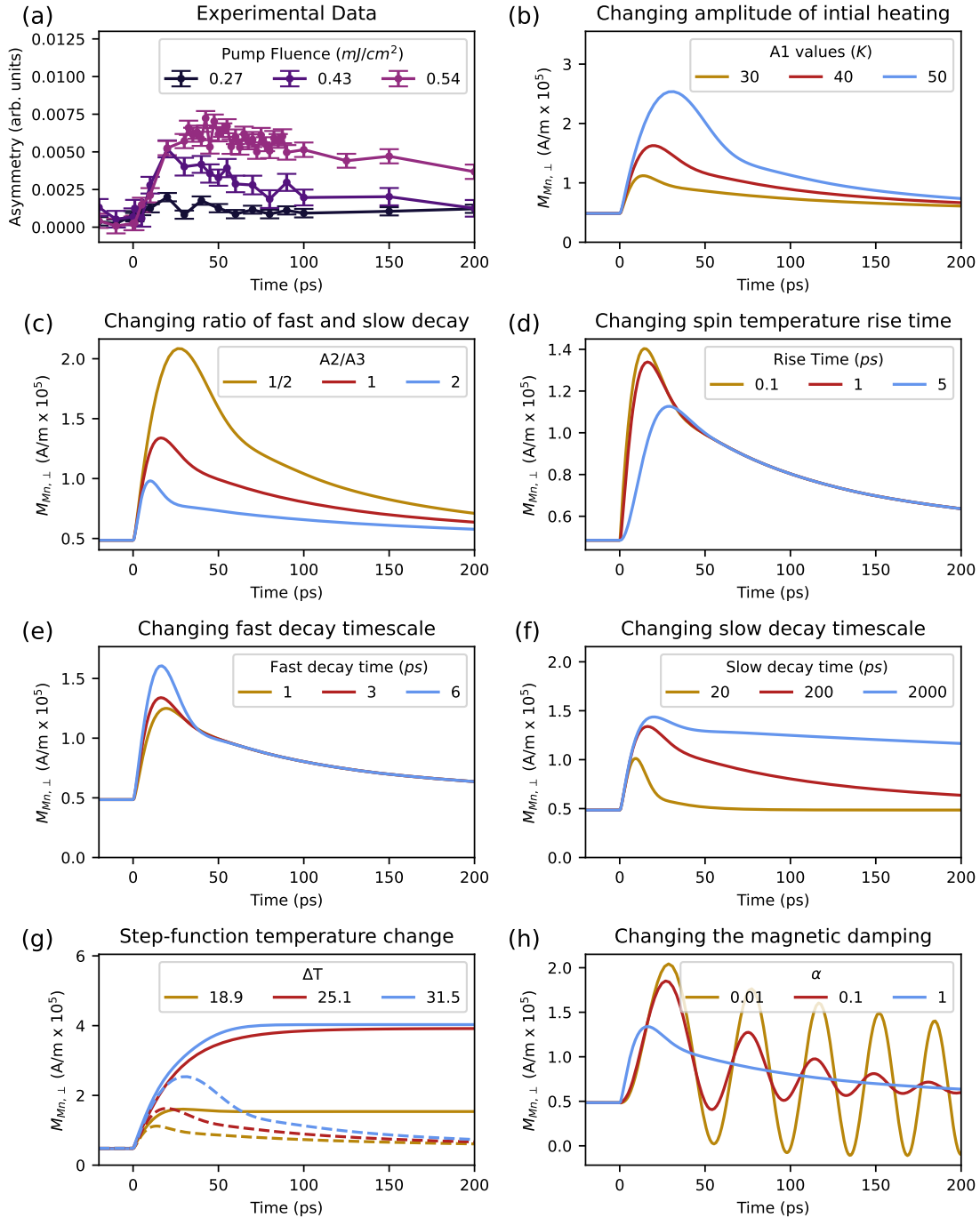
The results of the low fluence simulation are shown in Fig. 5.8. The effect of changing the incident fluence is shown experimentally in Fig. 5.8(a), and in simulation in Fig. 5.8(b). The simulated fluence is determined by the amplitude of the applied spin temperature increase, parameter  $A_1$  in Eq. 5.25. Since the exact shape of the time-dependent spin temperature profile is unknown, Figs. 5.8(c)-(f) simulate different parameters for the applied temperature profile based on Eq. 5.25. The parameters tested include the the ratio of the amplitudes of the fast and slow spin temperature decay,  $A_2$  and  $A_3$ , as well as the timescales themselves. Unless otherwise specified in the subfigure legends of Fig. 5.8, the parameter used were as follows:  $T_0 = 270 K$ ,  $A_1 = 35 K$ ,  $A_2=1/2 A_1$ ,  $A_3 = 1/2 A_1$ ,  $\tau_{rise}=1 ps$ ,  $\tau_{decay1}=3 ps$ ,  $\tau_{decay2}=200 ps$ , and  $\alpha=1$ . There is good agreement between the experimental trends and the shapes of the simulated figures in Fig. 5.8 across a wide range of temperature model parameters. The real temperature profile of the sample may be quite complex. There are many different timescales for heat transport in the sample: spin-electron thermalization, spin-lattice thermalization, sample-epoxy thermalization, epoxy-mount thermalization etc. Furthermore, the heat capacity of each of these systems is not linear in temperature. Nonetheless, the shape and timescale of the low fluence spin reorientation is

effectively reproduced with this simple model.

In the simulations in Fig. 5.8, a critical damping of  $\alpha = 1$  was applied. With a more physical value of  $\alpha$  (e.g. 0.01 to 0.1), as depicted in Fig. 5.8(h), very large oscillations dominate. However, in the experimental data we do not see these large precessions. This lack of clear oscillations in the experimental data can be explained by a non-uniform excitation of the Tb166 spin system. Heat from the incident pump laser pulses causes a thermal gradient in the sample. The top surface is hottest and the temperature decreases through the sample depth. Furthermore, the pump excitation has a Gaussian spatial profile. Therefore, not all probed parts of the sample experience identical excitation amplitudes. This is further compounded by sample inhomogeneities; e.g. surface roughness, strain, and crystalline disorder; which could affect both the strength of the absorption of the pump laser as well as the temperature-dependent response. Therefore, we cannot expect the probe to measure an in-phase bulk precessional motion. By applying a damping factor of  $\alpha = 1$ , we can see the underlying dynamics without the overriding precessional motion. This allows us to compare the model with the experimental results.

In Fig. 5.8(g) the laser-induced temperature change is modeled as a step-function. No exponential increases or decreases were applied, instead an instantaneous  $\Delta T$  was introduced at  $t = 0$ . The purpose of investigating the temperature step-function was to isolate the effects of the model-specific rise times and decays from the system's intrinsic spin-reorientation timescale. The data from subfigure (b) is overlaid on (g) as dotted lines. Due to the competing exponentials in Eq. 5.25, the maximum temperature increases in the model in subfigure (b) are a little lower than the values used for the heating amplitudes, i.e. the  $A_1$  values. For example, an  $A_1$  value of 50 K corresponded to maximal spin-temperature increase of 31.5 K and so forth. Therefore, to aid comparison, we chose the three  $\Delta T$  values for the step-function model so that they give the same maximum temperatures as the three-exponential model in subfigure (b). In the case of  $\Delta T = 18.9$  K, a partial reorientation takes place, as seen in subfigure (g). In the case of  $\Delta T = 25.1$  K or 31.5 K, full reorientations occur. The fitted spin-reorientation rise times of the step-function model agree very well with the experimentally determined values, as seen in Fig. 5.6. By fitting

Figure 5.8: **A low fluence dynamic model of Tb166.** The modeling is based on the temperature profile described by Eq. 5.25. Experimental data is presented for comparison in (a). The effects of changing the model parameters are shown. These are: (b) changing the amplitude of the initial heating  $A_1$ ; (c) changing the ratio of the amplitudes of the fast and slow temperature decays,  $A_2$  and  $A_3$ ; (d) changing the rise time of the spin bath temperature,  $\tau_{rise}$ ; (e) changing the fast decay timescale,  $\tau_{decay1}$ ; and (f) changing the slow decay timescale,  $\tau_{decay2}$ . In (g), a step-function temperature change is used instead of a three-exponential model.  $\Delta T$  values are chosen to match the maximum temperature changes from subfigure (b) and the data from subfigure (b) is overlaid as dotted lines. In (h), the magnetic damping factor,  $\alpha$ , is varied.



the exponential rise of the three  $\Delta T$  curves in (g) using Eq. 5.15 , we obtain exponential rise times of:  $7.7 \pm 0.2 \text{ ps}$ ,  $25.3 \pm 0.1 \text{ ps}$  and  $21.6 \pm 0.2 \text{ ps}$  for  $18.9 \text{ K}$ ,  $25.1 \text{ K}$  and  $31.5 \text{ K}$  respectively. The latter two values fall within the experimentally determined reorientation time for  $0.5 \text{ mJ/cm}^2$  at  $24 \pm 9 \text{ ps}$ . This agreement is rather remarkable when we consider that the only free parameters in the step-function model are the initial and final temperature as well as the damping term  $\alpha$  (which is set to 1). We then fit the rise times of the corresponding three-exponential model results shown in subfigure (b). For the smallest temperature increase (yellow) the timescale is  $8.3 \pm 1 \text{ ps}$ . The corresponding step-function model rise time had a value of  $7.7 \pm 0.2 \text{ ps}$  which falls within these error bars. For the other two curves (red and blue) the three-exponential values are lower than the step-function values. For  $A_1 = 40 \text{ K}$  we obtain  $10.9 \pm 1 \text{ ps}$  and for  $A_1 = 50 \text{ K}$  we obtain  $15.3 \pm 1 \text{ ps}$  (which falls within the error bars for the experimental timescale at  $0.5 \text{ mJ/cm}^2$  of  $24 \pm 9 \text{ ps}$ ). While there are some differences in the rise times between the two models, overall the experimental timescales are very well reproduced.

When we consider the precession of spins in a magnetic field, the intrinsic timescale can be best understood through the energy-time correlation[36]:

$$t \sim h/E. \quad (5.26)$$

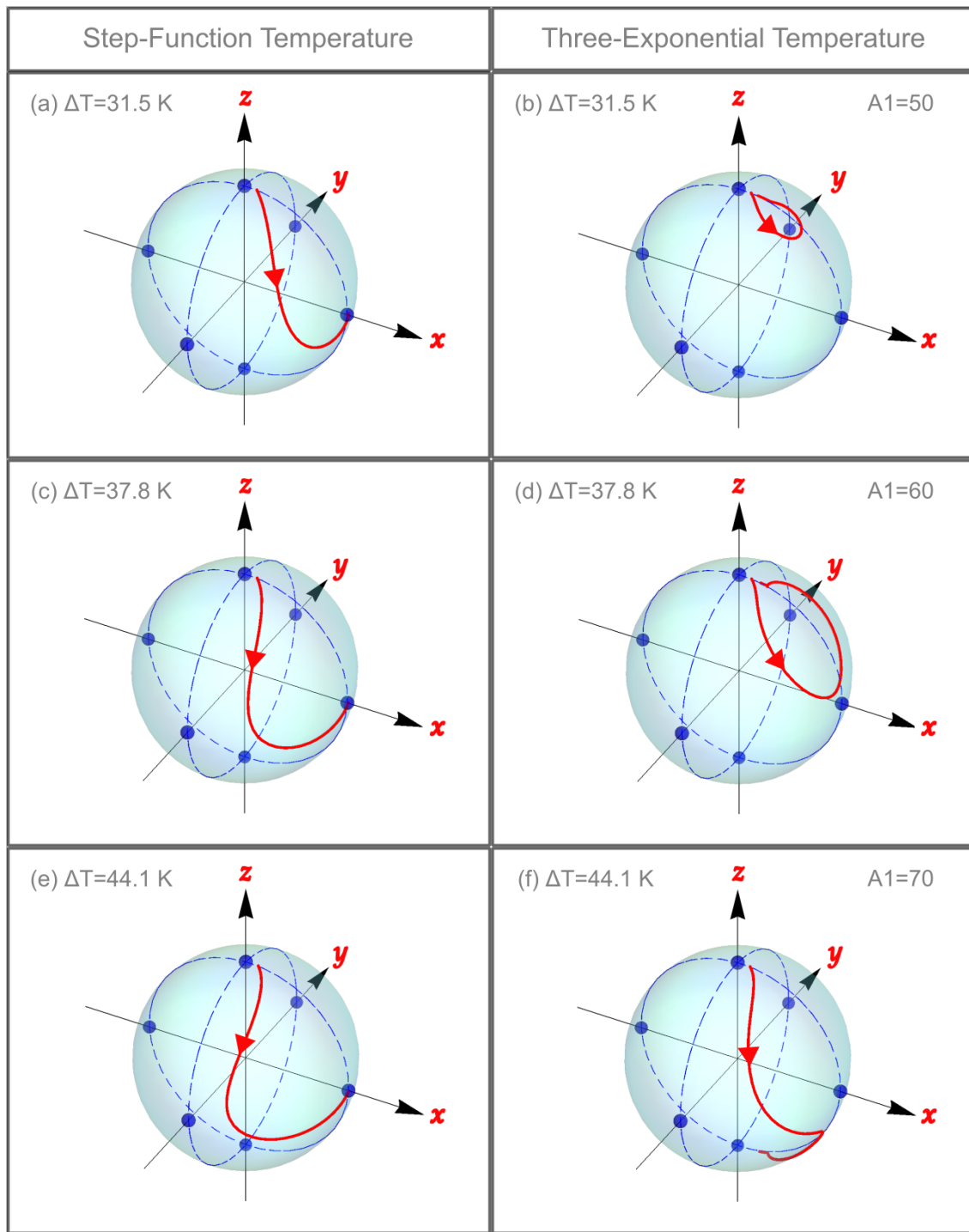
This equation links the cycle time,  $t$ , to its characteristic energy,  $E$ . From this relationship, we derive that for an energy of  $1 \text{ meV}$ , we should expect a cycle time of  $4 \text{ ps}$ . Therefore, for the  $\text{meV}$  energy scale of the Tb166 anisotropy, we should expect an intrinsic  $\text{ps}$  timescales as confirmed experimentally and in the model. The anisotropy energy of Tb166 is very large,  $\text{meV}$  scale, compared to less exotic materials where we expect anisotropies on the  $\mu\text{eV}$  scale. The large anisotropies of the Tb166 facilitates the fast reorientation (10's of  $\text{ps}$  timescale).

It is notable that increasing the value of  $\Delta T$  in the step-function model does not necessarily increase the speed of the reorientation. Indeed, the rise time at  $\Delta T=31.5 \text{ K}$  was longer than for a smaller  $\Delta T$  of  $25.1 \text{ K}$ . To understand the reason, we must investigate the full three-dimensional

nature of the spin orientation with time, rather than focusing on only the  $x$ -component. In Fig. 5.9, we plot the direction of the time-dependent magnetization unit vector as annotations on a sphere. The initial state is the same in each subfigure. The initial temperature is 270  $K$ , meaning that the spin is orientated out-of-plane, i.e. on the  $z$ -axis. The applied field of 185  $mT$  in the  $+x$  direction means that the initial state has a small  $+x$  component, i.e. it is a little canted off the  $z$ -axis. The sample temperature is increased either instantaneously as a step-function (left-hand column) or with the three-exponential model (right-hand column). In this figure, slightly higher fluences are investigated than in the rest of this section. However, all data still remains at least 100  $K$  below the Curie temperature. For the step-function model (left-hand column), increasing the temperature imparts more momentum into the system. However, the spin system doesn't necessarily reorient more efficiency. That is because it traces out a wider path between the initial and end points. Specifically, the transient  $y$ -component amplitude grows with increasing  $\Delta T$ .

In the second column of Fig. 5.9, we plot the results from the three-exponential temperature model. The temperature increases,  $\Delta T$ , are matched with the step-function model. At lower values of  $A_1$  (i.e. lower  $\Delta T$ ), the spin reorientation is incomplete and a small circle is traced out by the magnetization vector. For the highest  $\Delta T$ , (Fig. 5.9 (f)) we see something quite remarkable. As the sample cools, the magnetization vector does not return to its original orientation. Instead, it aligns to the opposite pole from which is began. Both poles are stable minima when  $T$  is below  $T_{SR}$  so there is nothing directly preventing the spin from switching in the re-thermalization process. At room temperature, there would be a very large barrier to reversing the spin-direction, but on heating, this is no longer the case. The reversal behavior occurs when  $A_1$  is anywhere in the range of 61-90  $K$ . In subfigures, (a), (c), (e), and (f) the reorientation "overshoots" the in-plane direction resulting in a small negative  $z$ -component. In the case of subfigure (f), the sample cools below  $T_{SR}$  while there is still a negative  $z$ -component. Therefore, when the magnetization vector reorients back out-of-plane as it cools, the  $-z$  direction is more favorable. We note that for more physical damping factors, i.e.  $\alpha = 0.1$  or  $0.01$ , this behavior still occurs but the final state is very sensitive to the exact temperature profile and the exact value of the damping. This is because the precessional motion

Figure 5.9: **A 3-dimensional depiction of the dynamics of the Tb166 magnetization vector.** The path of the magnetization unit vector is traced out in red over the first 200 ps of the dynamics. The sample plane is oriented in  $x - y$ . The  $z$ -axis is the out-of-plane direction. The initial sample temperature is 270 K, therefore the initial magnetization direction is out-of-plane aside from a small canting induced by the 185 mT applied field in  $+x$ . Three different magnitudes of induced temperature changes are plotted for the step-function model (LHS) and the three-exponential model (RHS).



can change the sign of the  $z$ -component and therefore send the system towards a different energy minimum.

Unfortunately, our measurement technique is not sensitive  $+z$  vs.  $-z$  alignments. It would be very interesting to confirm such behavior experimentally. We have no way of determining the initial  $z$ -axis direction in our experimental as both directions are energetically equivalent and the initial  $z$ -direction does not effect the  $x$ -projected dynamics that are measured. The  $180^\circ$  reorientation of subfigure (f) presents the possibility that this material could be optically switched by ultrafast pulses between two exceedingly stable ground state configurations without requiring very large laser fluences. The anisotropy barrier at room temperature is much larger than transition metal alloys traditionally used in magnetic recording. Furthermore, Tb166 only requires a small amount of heating to reach  $T_{SR}$ , compared to approaching the Curie temperature in a HAMR hard-drive. However, Tb166 may not support the small domains required for practical data storage applications and precessional motion may make the final state difficult to predict.

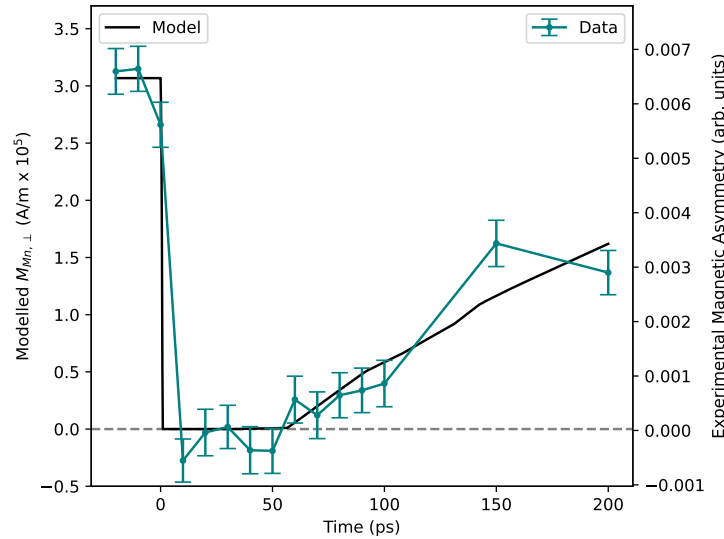
### 5.2.5.2 High Fluence Modeling

In the highest fluence experimental data,  $2.1 \text{ mJ/cm}^2$  and  $3.6 \text{ mJ/cm}^2$ , the sample is rapidly heated above  $T_C$  and then re-magnetizes in-plane, Fig. 5.5 (b). The signals continue to increase until the longest timescale of  $200 \text{ ps}$ . This implies that the sample is still in the process of remagnetizing in-plane at  $200 \text{ ps}$ . The temperature profile does not pass through  $T_{SR}$  during the time window measured. Therefore, no spin precession needs to be modeled. The experimental curves can be modeled by applying a time-dependent temperature profile and tracking the saturation magnetization of the  $Mn$  sublattice.

In Fig. 5.10 the experimental data for  $3.6 \text{ mJ/cm}^2$  is plotted. A three-exponential temperature model is applied. For the model, a larger initial sample temperature ( $294 \text{ K}$ ) was used compared to the low fluence modeling ( $270 \text{ K}$ ) as the initial in-plane signal was larger for the high fluence data. The slow decay time was increased to  $800 \text{ ps}$  to match the experimental results, and the  $A_1$  amplitude was increased to  $275 \text{ K}$  (note that  $3.6 \text{ mJ/cm}^2$  is 6x larger than the the largest experimental fluence

in the low fluence results). The increase in the slow decay timescale is understandable as there are many competing timescales for heat transport in the sample and it may be more difficult for a sample to dissipate additional heat when the baseline temperature of the sample is hotter.

Figure 5.10: **Modeling the high fluence behavior of Tb166.** The model utilizes an initial temperature of 294 K, an  $A_1$  amplitude of 275 K, and a slow decay time constant of 800 ps. The experimental data is for a fluence of 3.6 mJ/cm<sup>2</sup>.



### 5.3 Conclusion

By measuring very small TMOKE signals at the  $Mn$   $M$ -edge, we are able to uncover the ultrafast dynamics of spin reorientation in  $TbMn_6Sn_6$  for the very first time. The ultrafast demagnetization proceeds on a timescale of about 1 ps. This is consistent with what we expect for a RE-TM alloy. The spin reorientation occurs on a timescale of  $\sim 20$  ps. This timescale is consistent with the reorientation being driven by very large anisotropies energies,  $\sim meV$  scale. We note that the spin reorientation timescale ( $\sim 20$  ps) is an order of magnitude slower than the ultrafast demagnetization ( $\sim 1$  ps). We observe distinct behavior in key regimes of high and low fluence pumping. The high fluence timescales are governed by heat dissipation at temperatures around  $T_C$ . The early timescales of the low fluence measurements are governed by impulsive anisotropy changes.

The later timescales are governed by heat dissipation at temperatures around  $T_{SR}$ . We verify the spin reorientation timescale by implementing the LL equation with a temperature-dependent magnetocrystalline anisotropy field.

The low fluence model successfully replicated the measured  $\sim 20$  ps spin-reorientation timescale both with a trial temperature profile and with a step-function temperature profile with few free parameters. We note that the overall shape of the experimental curves were replicated for a wide range of different model parameters. The magnetic damping was set to  $\alpha=1$  to remove precessional motion as it wasn't seen in the experimental data (most likely due to non-uniform sample excitation). Interesting, with a specific range of excitation fluences, the model predicts a  $180^\circ$  reorientation of the out-of-plane moment. This could facilitate optically controlled magnetization switching between very stable ground states, which could have useful applications in spintronics or data storage. However, this result still needs to be verified experimentally. The high fluence data did not involve spin reorientation but could be fit extremely accurately with a "slow recovery" timescale of 800 ps.

#### 5.4 Signal Normalization

The measurements in Fig. 5.5 took between 16 and 24 hrs of data collection per fluence to achieve the signal-to-noise ratio presented. One issue associated with taking data over these long timescales, was sample damage induced by the pump and probe lasers. The sample was very small (few mm's diameter) and, in many areas, the surface roughness was too large to make a measurement. Therefore, we were limited to taking data in one sample location per fluence. The pump pulses were a low energy ( 1.59 eV), high fluence (few  $mJ/cm^2$  range) source of damage, while the probe laser has a comparatively much lower fluence (four orders of magnitude lower) but significantly higher photon energy (30 -73 eV range). The sample damage reduced the magnetic signal over time. To prevent sample damage from influencing the measured dynamic behavior, the order in which the time points were measured was randomized. This random order was then repeated hundreds of times. This prevented systematic errors that would arise when measuring the time points sequentially. Nonetheless, the sample damage reduced the overall size of the signal. The amount of damage

differed between different pump fluences and sample locations.

After taking the original data with 6 fluences on 6 different sample locations, we devised a normalization procedure to allow us to compare the magnitudes of signals obtained despite sample inhomogeneities and fluence-dependent damage from the pump laser. We called this the normalization factor, denoted (NF). The NF is calculated in Table 5.4 and applied to all the data in Figs. 5.4, 5.5, and 5.6. The steps used to determine the NF value are described below.

The measurement of the NF was made after the original 16-24 hr scans of varying fluence depicted in Fig. 5.5. The sample locations used for the original scans were already highly damaged. Therefore, we chose 6 new high reflectivity, undamaged locations on the sample for the NF measurement. These 6 sample locations were used to determine the NFs for the 6 fluences used in the study and appear in Table 5.4, column 1. The measurement of the NF consisted of two steps: the CV measurement and the MV measurement.

The first step is the control value (CV) measurement. To obtain the CV, we measured the magnetic signal with  $0.54 \text{ mJ/cm}^2$  pumping, taken at a fixed pump-probe delay (30 ps). The fluence of  $0.54 \text{ mJ/cm}^2$  was chosen because it induced a well-defined magnetic response without excessive sample damage. The time delay of 30 ps was chosen as this is where the signal is largest for  $0.54 \text{ mJ/cm}^2$  pumping. By measuring each new sample location under the same conditions, we determined the severity of sample inhomogeneities and attempted to mitigate their influence. We calculated the mean of the six measurements and use this to normalize each CV measurement. The normalized CV values are depicted in column 2 of Table 5.4. The maximum deviation from the mean was 20%. i.e. CV=1.2 (at location 2).

The second step is the measurement value (MV) measurement. The MV is obtained by measuring the MOKE signal for each of the six fluences with a pump-probe delay chosen to maximize the signal. Each fluence is measured on a different one of the six sample locations that were previously used for the CV measurement. The time delays for the MV measurements were chosen to maximize the signal for each specific fluence. The chosen time delays were: 20 ps, 30 ps, 30 ps, 70 ps, 200 ps, and -10 ps respectively. The MV values are listed in Table 5.4, column 4. Unlike the CV values,

the MV values across different sample locations should not be similar to each other as they were taken at different fluences and different time delays. Before both the CV and MV measurements, the sample had to thermalize with the relevant pump fluence so that the temperature of the sample would be stable throughout the scan. The probe was blocked while thermalizing with the pump (to limit sample damage from EUV). Furthermore, we kept each measurement as short as possible to limit sample damage. The timing was as follows: thermalize for 35 mins with  $0.54 \text{ mJ/cm}^2$ , measure the CV for 1 hour, thermalize for 15 mins with chosen fluence, measure the MV for 1 hour. These timings were a trade-off between improving signal-to-noise and minimizing exposure to the laser beams.

Finally, in Table 5.4, column 5, we recorded the measured asymmetries from the full dynamic fluence-dependent traces at the same specific fluences and time delays used for the MV measurement. These values are the real values (RVs). The RVs give us information on how much the measured signal was reduced due to sample damage over a long scan compared to the relatively short MV scans. By combining the values of the CV, MV and RV, the normalization factor can be calculated using the formula in Table 5.4, column 6.

For all fluences, except  $0.27 \text{ mJ/cm}^2$ , the normalization factor was greater than 1, i.e. the normalization process increased the magnitude of the signal. An  $\text{NF} > 1$  is expected in order to compensate for sample damage that occurs over the dynamic scans. The reason the  $0.27 \text{ mJ/cm}^2$  fluence NF was not  $> 1$ , may be because it had the least pumping, and therefore the least sample damage. Furthermore, the error bars on the  $0.27 \text{ mJ/cm}^2$  NF were quite large due to the small overall magnetic signal induced by this fluence.

Table 5.1: **Calculations of the normalization factors used for each fluence on Tb166.** Error bars in the CV, MV, and RV represent the standard error based on repeated measurements. The errors in NF are calculated using standard error propagation techniques. Error on the NF is not represented in the error bars on figures in the main text.

<b>Sample Location</b>	<b>Control Value CV</b>	<b>Fluence (<math>mJ/cm^2</math>)</b>	<b>Measured Value MV (<math>1e-3</math>)</b>	<b>Real Value RV (<math>1e-3</math>)</b>	<b>Normalization Factor</b> $NF = (MV/RV) * 1/CV$
1	$0.96 \pm 0.17$	0.27	$1.9 \pm 0.9$	$2.5 \pm 0.3$	$0.8 \pm 0.4$
2	$1.20 \pm 0.22$	0.43	$4.8 \pm 1.1$	$2.9 \pm 0.4$	$1.4 \pm 0.4$
3	$1.00 \pm 0.17$	0.54	$5.7 \pm 0.9$	$4.1 \pm 0.3$	$1.4 \pm 0.3$
4	$0.96 \pm 0.15$	1.1	$9.0 \pm 0.8$	$5.2 \pm 0.4$	$1.8 \pm 0.3$
5	$0.98 \pm 0.15$	2.1	$8.4 \pm 0.9$	$4.7 \pm 0.4$	$1.8 \pm 0.4$
6	$0.90 \pm 0.20$	3.6	$6.0 \pm 1.0$	$5.8 \pm 0.4$	$1.1 \pm 0.3$

## Chapter 6

### Outlook

This chapter contains an overview of possibilities for future beamline upgrades and a summary of the main findings of this thesis.

#### 6.1 Future Beamline Upgrades

In section, I will give an overview of some possible improvements to the X-MATTER beamline including: sample temperature control, sample chamber upgrades, changes to the pump energy or pulse duration, as well as two-color high harmonic generation.

##### 6.1.1 Temperature Control

The current iteration of the X-MATTER beamline does not allow control over the temperature of the sample. Many magnetic samples have interesting low temperature phase transitions including: multiple phase transitions in spinel oxides, the Verwey transition in Magnetite, the low temperature phase transition in Tb166, low temperature phase transitions in Heuslers, and many more. Furthermore, sample heating would allow us to bring samples through high temperature phase transitions with different combinations of static heating and transient pump-induced heating which could reveal interesting behaviors.

The TMOKE beamline of Stefan Mathias's group in Göttingen has an integrated cryostat[171] (Janis Research ST400) which allows for sample temperatures between 10 and 420 K. However, they have not yet published any dynamic data with sample cooling (to my knowledge). One major

consideration for cold temperature measurements is mitigating contamination. When the sample is the coldest object in the vacuum chamber, contaminants will condense on the sample surface at an increased rate. Furthermore, the focused EUV beam at the sample surface can interact with contaminants and this increases the rate of sample damage. Therefore, it is reasonable to expect that ultrahigh vacuum (UHV) (or vacuum levels close to UHV quality) would be required for a cryo-cooled sample. The X-MATTER beamline is high vacuum (HV) but not UHV. They are currently several components in the vacuum which are not compatible with UHV. For example, Quickflange (QF) vacuum components with rubber gaskets are used in most of the chambers. These would need to be replaced with ConFlat (CF) components which utilize copper gaskets. These perform better and can be heated to high temperatures to bake the chamber. Baking the chamber over several hours or days increases the rate of out-gassing and is used to achieve UHV conditions. However, this process would have to be repeated every time vacuum is broken- i.e. every time the sample is changed (unless a special sample loading system is implemented). HV and UHV portions of the vacuum system can be separated using an Al-filter[171], since Al is semi-transparent to EUV.

Sample heating may be easier to achieve than cooling. In fact, we were able to augment the current sample chamber to allow for heating of a  $VO_2$  sample to measure the metal-insulator transition at  $80\text{ }^\circ\text{C}$  with a heater designed by the KM group nanothermal team. However, this was a non-magnetic sample and transient reflectivity measurements were made with no applied magnetic field. Accommodating the heater required adding an attachment to extend the sample chamber. This attachment blocked access from the projection field electromagnet. The projection field drops-off very rapidly with distance and so it must be very close to the sample. This means there is very little space for heating apparatus. In the following section, I discuss other options for the application of an external magnetic field. These options might allow additional space for heating or cooling apparatus.

### 6.1.2 Sample Chamber

Several studies have noted the impact of changing the angle of incidence on the measured TMOKE signal[19, 172]. Our sample chamber is built to accommodate a  $50^\circ$  angle of incidence. The MOKE signal is maximized at the Brewster angle (e.g.  $45^\circ$ ). However, measuring at exactly the Brewster angle leads to the more non-magnetic artifacts[172]. Therefore, a  $50^\circ$  angle of incidence is used as a compromise between maximizing the signal strength and reducing artifacts. Nevertheless, the angle of acceptance of the chamber is quite large, and with careful placement of the chamber, it can accept  $50 \pm 5^\circ$ . However, the sample chamber could be upgraded to accommodate measurements at a wider range of possible angles. Furthermore, if precise changes to the angle of incidence could be made without unbolting the entire chamber, this would significantly aid alignments. This is especially relevant because samples aren't always epoxied at the exact same angle relative to the sample mount. Unfortunately, the current chamber design does not accommodate rotating the sample independently from the chamber. However, an alternative could be to introduce a small pivot centered on the sample plane, around which the chamber can rotate, thereby changing the angle of incidence. Alternatively, the chamber itself could be redesigned. Designing a chamber where the sample could rotate while still applying a consistent strength of external magnetic field could be somewhat challenging but not impossible.

In the X-MATTER beamline, the sample is mounted on high precision SmarAct XYZ positioning stages. This allows nm-precision movements of the sample. In general, these stages are used to find areas of highest reflectivity which is most important on samples with poor surface quality. Furthermore, this allows us to move the sample away from damaged areas to perform further measurements. Damage occurs from exposure to the pump and probe beams. The high photon energy of the probe pulses and the intense electric fields of the pump pulses are both very damaging when focused onto the sample. The reflectivity of the sample generally degrades significantly on a several hours timescales. The exact rate of damage is strongly depend on the sample composition, capping layer, and pump fluence used. These high precision stages could be used to make a spatially-resolved

MOKE measurement. However, the resolution of such a measurement would be limited by the spot size of the probe. The probe spot size at the sample plane has a  $1/e^2$  radius of  $\sim 40 \mu\text{m}$ , while the pump spot  $1/e^2$  radius of  $\sim 500 \mu\text{m}$ . TMOKE is not the most ideal MOKE technique for spatial measurements. This is because the magnetic contrast is obtained by fully magnetizing the sample in two opposite directions and observing a difference in reflectivity. This prevents, for example, the imaging of domains which would be destroyed by magnetizing the sample. Nonetheless, there could be some specific sample geometries where spatial information would be interesting. For example, if a sample contained nanostructures or distinct regions with different properties.

One limitation of the X-MATTER beamline is that it cannot apply magnetizing fields above  $200 \text{ mT}$ . This means that only softer magnets can be studied since the sample magnetization needs to be fully saturated to make the TMOKE measurements. The X-MATTER beamline currently utilizes a GMW Model 5201 projection field electromagnet. This magnet sits outside the vacuum and the projected magnetic field penetrates into the vacuum chamber via a glass plate. A stronger magnetic field could be incorporated using custom flanges designed to incorporate magnetic pole tips. A similar geometry is used by Möller *et al.*[171] and field strengths of up to  $860 \text{ mT}$  are achieved.

The X-MATTER beamline could be adapted for magnetic circular dichroism (MCD) measurements. An HHG based MCD beamline is described by Yao *et al.*[173]. MCD signals are easier to interpret than TMOKE signal. Furthermore, they are not limited to measuring only the top surface of the sample. However, MCD signals are typically an order of magnitude smaller than TMOKE signals and measuring them requires the generation of circularly polarized high harmonics[174] with a transmission mode measurement geometry.

Measuring in transmission mode would require building a new sample chamber designed for a normal incidence illumination. This chamber would need to accommodate a spectrometer behind the sample to catch the transmitted beam. MCD measurements would require samples to be grown on thin EUV-transmissive substrates (normally Al or  $\text{Si}_3\text{N}_4$  films). These substrates require delicate handling. Furthermore, they may introduce strain and may only be able withstand weak pump fluences. In the TMOKE geometry (i.e. reflection mode), samples can be grown on thick substrates.

This makes seeding the correct crystal structure easier. Furthermore, the samples are more robust and better at dissipating heat.

The X-MATTER beamline could also be used for resonant magnetic scattering (RMS) measurements. The easiest way to do this would be to incorporate the resonant magnetic scattering (RMS) chamber currently being designed by I. Binnie. The RMS chamber could be placed in lieu of the current sample chamber. After the focal plane of the X-MATTER sample toroid, a second focusing optic (part of the RMS chamber design) could refocus the beam to a new sample plane within the RMS chamber. This would require minimal changes to the beamline and the reference arm would still be functional for the elimination of source noise. Furthermore, with this combination of two focusing optics, the spot size may be smaller than what could be achieved with a single focusing optic. In the RMS measurements, a small probe spot size is important for finding individual regions with consistent domain structures. Another other option to incorporate the RMS chamber would be to remove all the chambers from the X-MATTER beamline and keep only the HHG part for use with the RMS chamber. This would reduce the total number of optics and therefore improve the throughput. However, this would require major changes to the beamline when switching between TMOKE and RMS experiments. Alternatively, a mirror could be inserted to pick off the EUV beam and send it to a separate RMS chamber. However, due to geometry constraints, it is unlikely this mirror could be at a grazing incidence and efficiency would therefore be low. Furthermore, space restrictions on the optical bench would make it very difficult to find space for the RMS chamber in this scenario. With all three of these proposed RMS designs, additional planning and alignments would be required to deliver a pump beam into the RMS chamber for dynamic measurements.

### 6.1.3 Pump Upgrades

One powerful upgrade to the pump beamline would be to introduce control over the pump photon energy. This would allow us to target specific optical excitations in the samples. For example, low energy photons could be used to pump the energy regime of the Weyl points in *Co<sub>2</sub>MnGa*. Alternatively, the photon energy could be tuned above and below the half-metallic gap in different

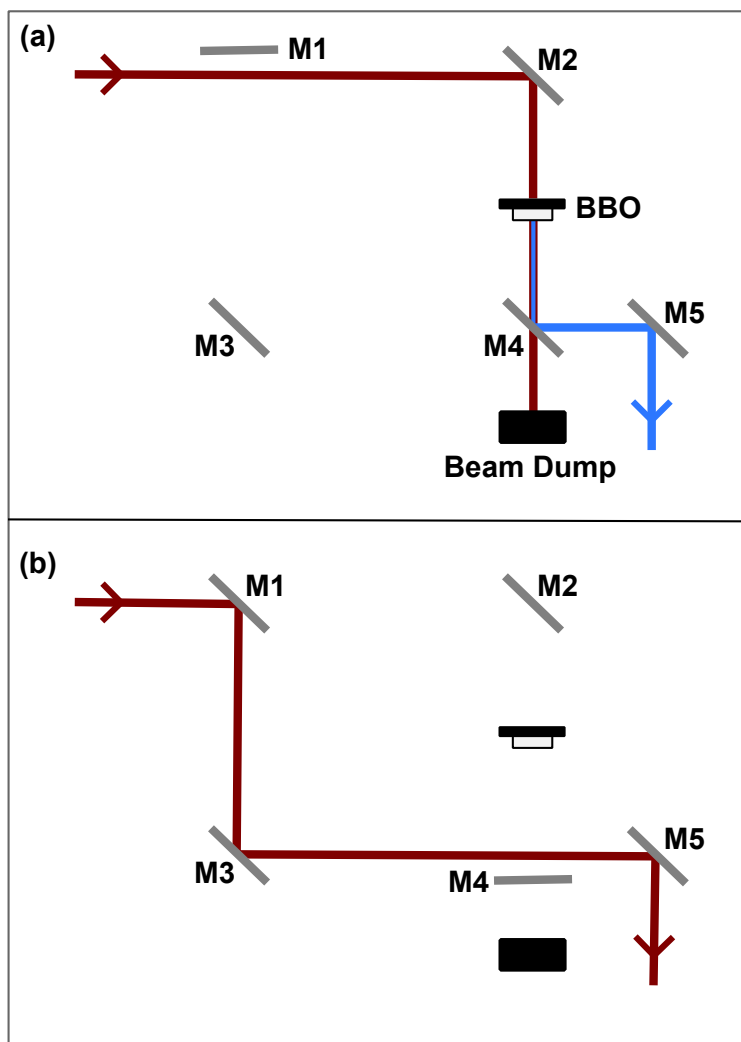
Heusler materials to determine how this impacts the dynamics of their OISTR signatures.

Ideally, an optical parametric amplifier (OPA) would be implemented to allow control over the photon energy. An OPA utilizes non-linear processes inside a crystal to divide incident photons into two lower energy photons. One of the two lower energies produced would be used for the pump beam. The photon energies produced can be tuned by changing the angle of the nonlinear crystal. However, with the current laser system, we do not have enough power to drive an OPA. To reach the  $M$ -edges of transition metals such as  $Co$ ,  $Fe$  and  $Ni$  we require 90% of the power from our KM Labs cryo-cooled Ti:Sapphire Wyvern system. This leaves very little optical power for the pump arm. To achieve the pump powers required to drive an OPA, we would most likely need to replace the Wyvern system or use a sample that requires lower energy harmonics. For harmonics with energies below 42 eV, we can use an argon gas target which requires a much lower driving power than neon or helium.

One scheme for changing the pump photon energy, which would be significantly easier to implement, would be to use a beta barium borate (BBO) crystal to up-convert the 800 nm (red) pump photons to 400 nm (blue) photons. This would require minimal changes to the beamline. A clever design would allow the user to effortlessly switch between red and blue beams, Fig. 6.1.

Another improvement to the pump arm would be to shorten the duration of pump pulses. Due to the nature of the HHG process, only the brightest part of the laser pulse has sufficient energy to drive the production of harmonics. This means that the probe pulse is significantly shorter than the pump pulse, in this case, by a factor of 2-3x. Therefore, the time resolution of the experiment could be significantly improved by shortening either the driving laser (which would shorten both the pump and probe pulses) or by shortening the pump pulses alone. The pulse duration from the Wyvern system when fully optimized is 38 fs, as measured with a frequency-resolved optical gating (FROG) system. Shorter pulses cannot be supported by the bandwidth of the Wyvern system. Therefore, to produce shorter pulses, the bandwidth would have to be increased by either upgrading the laser system or by exploiting spectral broadening achieved through self-phase modulation. The latter technique can be realized through the use of either a hollow-core fiber filled with a high pressure

Figure 6.1: **A possible design for a combined red and blue pump arm.** (a) When M1 (flip mirror) is removed, a blue pump beam is produced. (b) When M4 (flip mirror) is removed a red pump beam is produced. A BBO crystal is used for frequency doubling of the 800 nm beam. Mirrors M1, M2, and M3 are coated for low group delay dispersion (GDD) at 800 nm. Mirror M4 is a low GDD mirror which transmits 800 nm while reflecting 400 nm, such as the UBS24 mirror from Thorlabs. Mirror M5 is a dielectric mirror coated for low GDD at both 400 nm and 800 nm, such as the UFM10R mirror from Thorlabs. M5 is the in-vacuum steering mirror. With this arrangement of mirrors, the path lengths of (a) and (b) can be matched so that the pump-probe time-zero is similar for both.



noble gas[175, 176] or multiple glass plates[177].

#### 6.1.4 Probe Upgrades

The techniques for tuning the driving laser energy described in Chapter 4 allows for most probing energies within the teeth of the harmonic comb to be accessible. However, these energy tunings are only possible when the oscillator and amplifier are performing optimally. Furthermore, the required detuning of spectrum and chirp comes at the cost of pulse duration and HHG flux. Another solution, to span more energies, would be to implement two-color driving. In this scheme, the driving laser (red) is combined with its second harmonic (blue). By independently adjusting the phase of the two colors, one can control the divergence of the beam as it travels through the HHG gas medium based on the ratio of short and long electron trajectories. By improving the focusability of the beam, the conversion efficiency can be improved[178]. Furthermore, both even and odd harmonics will be produced, yielding twice as many probing energies. Kfir *et al.*[179] have proposed a compact scheme for the in-line production of blue and red harmonics, known as MAZEL-TOV. The use of an achromatic  $\frac{\lambda}{4}$  waveplate allows switching between linearly, elliptically and circularly polarized harmonics. The MAZEL-TOV scheme was attempted by P. Johnsen and N. Brook at the X-MATTER beamline. However, creating spatial and temporal overlap of the red and blue foci within the gas cell proved to be very challenging. Kfir *et al.*'s design was fully removable, as demonstrated in their video (supplementary materials of [179]). Therefore, we assume that proper alignment of the MAZEL-TOV scheme could be achieved by creating a removable assembly and first achieving spatial and temporal overlap of the red and blue pulses by optimizing third harmonic signal from a four-wave mixing crystal. After optimizing, the assembly could then be inserted into the X-MATTER beamline.

## 6.2 Conclusion and Final Remarks

Condensed matter physics is the study of an exotic landscape of many-body interactions. While many useful models have been developed, we are far from a comprehensive understanding

of the physics of solids. Magnetic materials have proven themselves to be an incredibly powerful technological tool. However, there are still many exciting avenues to be explored. Just this year, there have been multiple headlines celebrating the discovery of a "new type of magnetism"[180, 181] for two entirely different discoveries: altermagnetism[182] (net zero moment but characteristics of both ferromagnetism and anti-ferromagnetism) and Kinetic magnetism[34] (ferromagnetism arising without exchange interaction). This is truly an abundant era for magnetism research.

Pulsed laser systems have the unique advantage of being able to investigate timescales which are much faster than conventional electronics. Furthermore, resonant techniques in the extreme ultra-violet or x-ray photon energy ranges, give us a unique insight into element-specific dynamics. By combining pulsed lasers with magnetic materials, we not only allow for ultrafast measurements of the most fundamental timescales of magnetism, but also, provide a means for ultrafast optically-controlled magnetization switching. In this thesis, I have focused on two main topics: spin-transfer in Heuslers, and spin-precession in ferrimagnetic  $TbMn_6Sn_6$ . The former represents the fast spin manipulation that we know of, and the latter is extremely relevant to the field of data storage and magnetic switching.

## Bibliography

- [1] Bharat Bhushan. Current status and outlook of magnetic data storage devices. Microsystem Technologies, 29(11):1529–1546, 2023.
- [2] Kathryn M. Goodenough, Frances Wall, and David Merriman. The Rare Earth Elements: Demand, Global Resources, and Challenges for Resourcing Future Generations. Natural Resources Research, 27(2):201–216, 2018.
- [3] Why HDDs Dominate Hyperscale Cloud Architecture | Seagate US. <https://www.seagate.com/blog/why-hdds-dominate-hyperscale-cloud-architecture/>, 2019. Accessed: 2023-11-10.
- [4] Data growth worldwide 2010-2025 | Statista. <https://www.statista.com/statistics/871513/worldwide-data-created/>, 2021. Accessed: 2023-11-10.
- [5] Jorge Puebla, Junyeon Kim, Kouta Kondou, and Yoshichika Otani. Spintronic devices for energy-efficient data storage and energy harvesting. Communications Materials, 1(1):1–9, 2020.
- [6] Amal El-Ghazaly, Jon Gorchon, Richard B. Wilson, Akshay Pattabi, and Jeffrey Bokor. Progress towards ultrafast spintronics applications. Journal of Magnetism and Magnetic Materials, 502:166478, 2020.
- [7] E. Beaurepaire, J.C. Merle, A. Daunois, and J.Y. Bigot. Ultrafast Spin Dynamics in Ferromagnetic Nickel. Physical Review Letters, 76(22):4250–4253, 1996.
- [8] C. Stamm, T. Kachel, N. Pontius, R. Mitzner, T. Quast, K. Holldack, S. Khan, C. Lupulescu, E. F. Aziz, M. Wietstruk, H. A. Dürr, and W. Eberhardt. Femtosecond modification of electron localization and transfer of angular momentum in nickel. Nature Materials, 6(10):740–743, 2007.
- [9] G. P. Zhang and W. Hübner. Laser-Induced Ultrafast Demagnetization in Ferromagnetic Metals. Physical Review Letters, 85(14):3025–3028, 2000.
- [10] B. Koopmans, J. J. M. Ruigrok, F. Dalla Longa, and W. J. M. de Jonge. Unifying Ultrafast Magnetization Dynamics. Physical Review Letters, 95(26):267207, 2005.
- [11] S. R. Tauchert, M. Volkov, D. Ehberger, D. Kazenwadel, M. Evers, H. Lange, A. Donges, A. Book, W. Kreuzpaintner, U. Nowak, and P. Baum. Polarized phonons carry angular momentum in ultrafast demagnetization. Nature, 602(7895):73–77, 2022.

- [12] V Shokeen, M Sanchez Piaia, J-Y Bigot, T Müller, P Elliott, JK Dewhurst, S Sharma, and EKV Gross. Spin flips versus spin transport in nonthermal electrons excited by ultrashort optical pulses in transition metals. Physical Review Letters, 119(10):107203, 2017.
- [13] E. Carpena, H. Hedayat, F. Boschini, and C. Dallera. Ultrafast demagnetization of metals: Collapsed exchange versus collective excitations. Physical Review B, 91(17):174414, 2015.
- [14] Dmitriy Zusin, Phoebe M. Tengdin, Maithreyi Gopalakrishnan, Christian Gentry, Adam Blonsky, Michael Gerrity, Dominik Legut, Justin M. Shaw, Hans T. Nembach, T. J. Silva, Peter M. Oppeneer, Henry C. Kapteyn, and Margaret M. Murnane. Direct measurement of the static and transient magneto-optical permittivity of cobalt across the entire  $M$ -edge in reflection geometry by use of polarization scanning. Physical Review B, 97(2):024433, 2018.
- [15] Emrah Turgut, Dmitriy Zusin, Dominik Legut, Karel Carva, Ronny Knut, Justin M. Shaw, Cong Chen, Zhensheng Tao, Hans T. Nembach, Thomas J. Silva, Stefan Mathias, Martin Aeschlimann, Peter M. Oppeneer, Henry C. Kapteyn, Margaret M. Murnane, and Patrik Grychtol. Stoner versus Heisenberg: Ultrafast exchange reduction and magnon generation during laser-induced demagnetization. Physical Review B, 94(22):220408, 2016.
- [16] Emrah Turgut, Chan La-o vorakiat, Justin M. Shaw, Patrik Grychtol, Hans T. Nembach, Dennis Rudolf, Roman Adam, Martin Aeschlimann, Claus M. Schneider, Thomas J. Silva, Margaret M. Murnane, Henry C. Kapteyn, and Stefan Mathias. Controlling the Competition between Optically Induced Ultrafast Spin-Flip Scattering and Spin Transport in Magnetic Multilayers. Physical Review Letters, 110(19):197201, 2013.
- [17] B. Koopmans, M. van Kampen, J. T. Kohlhepp, and W. J. M. de Jonge. Ultrafast Magneto-Optics in Nickel: Magnetism or Optics? Physical Review Letters, 85(4):844–847, 2000.
- [18] Somnath Jana, R. S. Malik, Yaroslav O. Kvashnin, Inka L. M. Locht, R. Knut, R. Stefanuik, Igor Di Marco, A. N. Yaresko, Martina Ahlberg, Johan Åkerman, Raghuvveer Chimata, Marco Battiato, Johan Söderström, Olle Eriksson, and Olof Karis. Analysis of the linear relationship between asymmetry and magnetic moment at the M edge of 3d transition metals. Physical Review Research, 2(1):013180, 2020.
- [19] Henrike Probst, Christina Möller, Maren Schumacher, Thomas Brede, John Kay Dewhurst, Marcel Reutzler, Daniel Steil, Sangeeta Sharma, G. S. Matthijs Jansen, and Stefan Mathias. Unraveling femtosecond spin and charge dynamics with extreme ultraviolet transverse MOKE spectroscopy. Physical Review Research, 6:013107, Jan 2024.
- [20] Chan La-O-Vorakiat, Emrah Turgut, Carson A. Teale, Henry C. Kapteyn, Margaret M. Murnane, Stefan Mathias, Martin Aeschlimann, Claus M. Schneider, Justin M. Shaw, Hans T. Nembach, and T. J. Silva. Ultrafast Demagnetization Measurements Using Extreme Ultraviolet Light: Comparison of Electronic and Magnetic Contributions. Physical Review X, 2(1):011005, 2012.
- [21] Daniel C Mattis and Daniel C Mattis. History of magnetism. Springer, 1981.
- [22] William Gilbert. De Magnete. Courier Corporation, 1958.
- [23] U.S. utility-scale electricity generation by source, amount, and share of total in 2022 | Energy Information Administration. <https://www.eia.gov/tools/faqs/faq.php?id=427&t=3>, 2023. Accessed: 2024-01-18.

- [24] Yongxiang Yang, Allan Walton, Richard Sheridan, Konrad Güth, Roland Gauß, Oliver Gutfleisch, Matthias Buchert, Britt-Marie Steenari, Tom Van Gerven, Peter Tom Jones, et al. REE recovery from end-of-life NdFeB permanent magnet scrap: a critical review. Journal of Sustainable Metallurgy, 3:122–149, 2017.
- [25] Claudiu C Pavel, Roberto Lacal-Arántegui, Alain Marmier, Doris Schüler, Evangelos Tzimas, Matthias Buchert, Wolfgang Jenseit, and Darina Blagoeva. Substitution strategies for reducing the use of rare earths in wind turbines. Resources Policy, 52:349–357, 2017.
- [26] Research: AI and compute | OpenAI. <https://openai.com/research/ai-and-compute>, 2018. Accessed: 2024-01-18.
- [27] What is the role of data centres and data transmission networks in clean energy transitions? | International Energy Agency. <https://www.iea.org/energy-system/buildings/data-centres-and-data-transmission-networks>, 2023. Accessed: 2024-01-18.
- [28] Why does Bitcoin use so much energy? | Forbes. <https://www.forbes.com/advisor/investing/cryptocurrency/bitcoins-energy-usage-explained/>, 2022. Accessed: 2024-01-18.
- [29] Seagate’s HAMR Update: 32 TB in Early 2024, 40+ TB Two Years Later. <https://www.anandtech.com/show/21125/seagates-hamr-update-32-tb-in-early-2024-40-tb-two-years-later>, 2023. Accessed: 2024-02-27.
- [30] Atsufumi Hirohata, Keisuke Yamada, Yoshinobu Nakatani, Ioan-Lucian Prejbeanu, Bernard Diény, Philipp Pirro, and Burkard Hillebrands. Review on spintronics: Principles and device applications. Journal of Magnetism and Magnetic Materials, 509:166711, 2020.
- [31] Ching H Tsang, RE Fontana, Tsann Lin, David E Heim, Bruce A Gurney, and ML Williams. Design, fabrication, and performance of spin-valve read heads for magnetic recording applications. IBM journal of research and development, 42(1):103–116, 1998.
- [32] Nilson Maciel, Elaine Marques, Lírída Naviner, Yongliang Zhou, and Hao Cai. Magnetic tunnel junction applications. Sensors, 20(1):121, 2019.
- [33] Vinod Kumar Joshi. Spintronics: A contemporary review of emerging electronics devices. Engineering Science and Technology, an International Journal, 19(3):1503–1513, 2016.
- [34] L. Ciorciaro, T. Smoleński, I. Morera, N. Kiper, S. Hiestand, M. Kroner, Y. Zhang, K. Watanabe, T. Taniguchi, E. Demler, and A. İmamoğlu. Kinetic magnetism in triangular moiré materials. Nature, 623(7987):509–513, November 2023.
- [35] Wikimedia Commons. Bethe–slater curve: elements above the horizontal axis are ferromagnetic, and those below are antiferromagnetic. [https://en.wikipedia.org/wiki/Bethe%E2%80%9393Slater\\_curve#/media/File:Bethe-Slater\\_curve\\_by\\_Zureks.svg](https://en.wikipedia.org/wiki/Bethe%E2%80%9393Slater_curve#/media/File:Bethe-Slater_curve_by_Zureks.svg), 2009. Accessed: 2024-01-17.
- [36] J. Stöhr and H.C. Siegmann. Magnetism: From Fundamentals to Nanoscale Dynamics, volume 152 of Solid-State Sciences. Springer, Heidelberg, Germany, 2006.

- [37] Patrick Bruno. Tight-binding approach to the orbital magnetic moment and magnetocrystalline anisotropy of transition-metal monolayers. Physical Review B, 39(1):865, 1989.
- [38] Frederick T Calkins, Alison B Flatau, and Marcelo J Dapino. Overview of magnetostrictive sensor technology. Journal of Intelligent Material Systems and Structures, 18(10):1057–1066, 2007.
- [39] Frank Claeysen, N Lhermet, R Le Letty, and P Bouchilloux. Actuators, transducers and motors based on giant magnetostrictive materials. Journal of Alloys and Compounds, 258(1-2):61–73, 1997.
- [40] Rajat K Roy, Ashis K Panda, and Amitava Mitra. Alloy development through rapid solidification for soft magnetic application. New Trends in Alloy Development, Characterization and Application, 2:39, 2015.
- [41] Nawshad Haque, Anthony Hughes, Seng Lim, and Chris Vernon. Rare earth elements: Overview of mining, mineralogy, uses, sustainability and environmental impact. Resources, 3(4):614–635, 2014.
- [42] A Vaterlaus, T Beutler, and F Meier. Spin-lattice relaxation time of ferromagnetic gadolinium determined with time-resolved spin-polarized photoemission. Physical Review Letters, 67(23):3314, 1991.
- [43] W Hübner and KH Bennemann. Simple theory for spin-lattice relaxation in metallic rare-earth ferromagnets. Physical Review B, 53(6):3422, 1996.
- [44] B. Koopmans, G. Malinowski, F. Dalla Longa, D. Steiauf, M. Fähnle, T. Roth, M. Cinchetti, and M. Aeschlimann. Explaining the paradoxical diversity of ultrafast laser-induced demagnetization. Nature Materials, 9(3):259–265, 2010.
- [45] Benedikt Y Mueller, T Roth, M Cinchetti, M Aeschlimann, and B Rethfeld. Driving force of ultrafast magnetization dynamics. New Journal of Physics, 13(12):123010, 2011.
- [46] M Cinchetti, M Sánchez Albaneda, D Hoffmann, T Roth, J-P Wüstenberg, M Krauß, O Andreyev, HC Schneider, M Bauer, and M Aeschlimann. Spin-flip processes and ultrafast magnetization dynamics in co: Unifying the microscopic and macroscopic view of femtosecond magnetism. Physical Review Letters, 97(17):177201, 2006.
- [47] D Steiauf and M Fähnle. Elliott-yafet mechanism and the discussion of femtosecond magnetization dynamics. Physical Review B, 79(14):140401, 2009.
- [48] Michael Krauß, Tobias Roth, Sabine Alebrand, Daniel Steil, Mirko Cinchetti, Martin Aeschlimann, and Hans Christian Schneider. Ultrafast demagnetization of ferromagnetic transition metals: The role of the coulomb interaction. Physical Review B, 80(18):180407, 2009.
- [49] Daniel Steil, Sabine Alebrand, Tobias Roth, Michael Krauß, Takahide Kubota, Mikihiko Oogane, Yasuo Ando, Hans Christian Schneider, Martin Aeschlimann, and Mirko Cinchetti. Band-structure-dependent demagnetization in the Heusler alloy  $Co_2Mn_{1-x}Fe_{1-x}Si$ . Physical Review Letters, 105(21):217202, 2010.

- [50] E. Carpene, E. Mancini, C. Dallera, M. Brenna, E. Puppini, and S. De Silvestri. Dynamics of electron-magnon interaction and ultrafast demagnetization in thin iron films. Physical Review B, 78(17):174422, 2008.
- [51] AB Schmidt, M Pickel, M Donath, Pawel Buczek, Arthur Ernst, VP Zhukov, PM Echenique, Leonid M Sandratskii, EV Chulkov, and M Weinelt. Ultrafast magnon generation in an Fe film on Cu (100). Physical Review Letters, 105(19):197401, 2010.
- [52] Michael Haag, Christian Illg, and Manfred Fähnle. Role of electron-magnon scatterings in ultrafast demagnetization. Physical Review B, 90(1):014417, 2014.
- [53] Dennis Rudolf, Chan La-O-Vorakiat, Marco Battiato, Roman Adam, Justin M Shaw, Emrah Turgut, Pablo Maldonado, Stefan Mathias, Patrik Grychtol, Hans T Nembach, et al. Ultrafast magnetization enhancement in metallic multilayers driven by superdiffusive spin current. Nature Communications, 3(1):1037, 2012.
- [54] Andrea Eschenlohr, Marco Battiato, Pablo Maldonado, N Pontius, T Kachel, K Holldack, R Mitzner, Alexander Föhlisch, Peter M Oppeneer, and C Stamm. Ultrafast spin transport as key to femtosecond demagnetization. Nature Materials, 12(4):332–336, 2013.
- [55] Marco Battiato, Karel Carva, and Peter M Oppeneer. Superdiffusive spin transport as a mechanism of ultrafast demagnetization. Physical Review Letters, 105(2):027203, 2010.
- [56] P. Elliott, N. Singh, K. Krieger, E. K. U. Gross, S. Sharma, and J. K. Dewhurst. The microscopic origin of spin-orbit mediated spin-flips. Journal of Magnetism and Magnetic Materials, 502:166473, 2020.
- [57] K. Krieger, J. K. Dewhurst, P. Elliott, S. Sharma, and E. K. U. Gross. Laser-Induced Demagnetization at Ultrashort Time Scales: Predictions of TDDFT. Journal of Chemical Theory and Computation, 11(10):4870–4874, 2015.
- [58] SI Anisimov, BL Kapeliovich, and TL Perelman. Electron emission from metal surfaces exposed to ultrashort laser pulses. Journal of Experimental and Theoretical Physics, 66(2):375–377, 1974.
- [59] GL Eesley. Observation of nonequilibrium electron heating in copper. Physical Review Letters, 51(23):2140, 1983.
- [60] Je-Ho Shim, Akbar Ali Syed, Jea-Il Kim, Hong-Guang Piao, Sang-Hyuk Lee, Seung-Young Park, Yeon Suk Choi, Kyung Min Lee, Hyun-Joong Kim, Jong-Ryul Jeong, et al. Role of non-thermal electrons in ultrafast spin dynamics of ferromagnetic multilayer. Scientific Reports, 10(1):6355, 2020.
- [61] Alber Lukas, Scalera Valentino, Unikandanunni Vivek, and Bonetti Stefano. NTMpy - N-Temperature Model solver. <https://github.com/udcm-su/NTMpy>, 2018. Accessed: 2023-12-08.
- [62] Lukas Alber, Valentino Scalera, Vivek Unikandanunni, Daniel Schick, and Stefano Bonetti. Ntmpy: An open source package for solving coupled parabolic differential equations in the framework of the three-temperature model. Computer Physics Communications, 265:107990, 2021.

- [63] Phoebe Tengdin, Wenjing You, Cong Chen, Xun Shi, Dmitriy Zusin, Yingchao Zhang, Christian Gentry, Adam Blonsky, Mark Keller, Peter M. Oppeneer, Henry C. Kapteyn, Zhensheng Tao, and Margaret M. Murnane. Critical behavior within 20 fs drives the out-of-equilibrium laser-induced magnetic phase transition in nickel. Science Advances, 4(3):eaap9744, 2018.
- [64] F. Seitz and D. Turnbull, editors. Solid State Physics, volume 14. Academic, 1963.
- [65] RJ Elliott. Theory of the effect of spin-orbit coupling on magnetic resonance in some semiconductors. Physical Review, 96(2):266, 1954.
- [66] Marco Battiato, Karel Carva, and Peter M Oppeneer. Theory of laser-induced ultrafast superdiffusive spin transport in layered heterostructures. Physical Review B, 86(2):024404, 2012.
- [67] A. J. Schellekens and B. Koopmans. Microscopic model for ultrafast magnetization dynamics of multisublattice magnets. Physical Review B, 87(2):020407, 2013.
- [68] Martin Henneke, Ilie Radu, Radu Abrudan, Torsten Kachel, Karsten Holldack, Rolf Mitzner, Arata Tsukamoto, and Stefan Eisebitt. Angular momentum flow during ultrafast demagnetization of a ferrimagnet. Physical Review Letters, 122(15):157202, 2019.
- [69] Peter Oppeneer. Handbook of Magnetic Materials: Chapter 3 Magneto-optical kerr spectra, volume 13C. Elsevier Science B.V., 2001.
- [70] Cornelis Harm Wind. On the theory of magneto-optic phenomena. ii. Physical Review (Series I), 6(2):98, 1898.
- [71] Guangyu Fan, K Legare, V Cardin, Xinhua Xie, R Safaei, E Kaksis, G Andriukaitis, A Pugžlys, BE Schmidt, JP Wolf, et al. Ultrafast magnetic scattering on ferrimagnets enabled by a bright yb-based soft x-ray source. Optica, 9(4):399–407, 2022.
- [72] Tenio Popmintchev, Ming-Chang Chen, Alon Bahabad, Michael Gerrity, Pavel Sidorenko, Oren Cohen, Ivan P Christov, Margaret M Murnane, and Henry C Kapteyn. Phase matching of high harmonic generation in the soft and hard x-ray regions of the spectrum. Proceedings of the National Academy of Sciences, 106(26):10516–10521, 2009.
- [73] Gerrit van der Laan and Adriana I. Figueroa. X-ray magnetic circular dichroism—a versatile tool to study magnetism. Coordination Chemistry Reviews, 277-278:95–129, 2014. Following Chemical Structures using Synchrotron Radiation.
- [74] Jeffrey L Krause, Kenneth J Schafer, and Kenneth C Kulander. High-order harmonic generation from atoms and ions in the high intensity regime. Physical Review Letters, 68(24):3535, 1992.
- [75] Maciej Lewenstein, Ph Balcou, M Yu Ivanov, Anne L’huillier, and Paul B Corkum. Theory of high-harmonic generation by low-frequency laser fields. Physical Review A, 49(3):2117, 1994.
- [76] Paul B Corkum. Plasma perspective on strong field multiphoton ionization. Physical Review Letters, 71(13):1994, 1993.
- [77] Christian Kern, Michael Zürch, and Christian Spielmann. Limitations of extreme nonlinear ultrafast nanophotonics. Nanophotonics, 4(3):303–323, 2015.

- [78] Maxim V Ammosov, Nikolai B Delone, and Vladimir P Krainov. Tunnel ionization of complex atoms and atomic ions in electromagnetic field. In High Intensity Laser Processes, volume 664, pages 138–141. SPIE, 1986.
- [79] XF Li, A l’Huillier, M Ferray, LA Lompré, and G Mainfray. Multiple-harmonic generation in rare gases at high laser intensity. Physical Review A, 39(11):5751, 1989.
- [80] Andy Rundquist, Charles G Durfee III, Zenghu Chang, Catherine Herne, Sterling Backus, Margaret M Murnane, and Henry C Kapteyn. Phase-matched generation of coherent soft x-rays. Science, 280(5368):1412–1415, 1998.
- [81] Justin Peatross, Julia R Miller, Kelly R Smith, Steven E Rhynard, and Benjamin W Pratt. Phase matching of high-order harmonic generation in helium-and neon-filled gas cells. Journal of Modern Optics, 51(16-18):2675–2683, 2004.
- [82] Andrew Ralph Rundquist. Phase-matched generation of coherent, ultrafast x-rays using high harmonics. Washington State University, 1998.
- [83] Charles G Durfee III, Andy R Rundquist, Sterling Backus, Catherine Herne, Margaret M Murnane, and Henry C Kapteyn. Phase matching of high-order harmonics in hollow waveguides. Physical Review Letters, 83(11):2187, 1999.
- [84] Stefan Mathias, Chan La-O-Vorakiat, Patrik Grychtol, Patrick Granitzka, Emrah Turgut, Justin M Shaw, Roman Adam, Hans T Nembach, Mark E Siemens, Steffen Eich, et al. Probing the timescale of the exchange interaction in a ferromagnetic alloy. Proceedings of the National Academy of Sciences, 109(13):4792–4797, 2012.
- [85] I Radu, Christian Stamm, Andrea Eschenlohr, Florin Radu, R Abrudan, Kadir Vahaplar, Torsten Kachel, Niko Pontius, Rolf Mitzner, Karsten Holldack, et al. Ultrafast and distinct spin dynamics in magnetic alloys. In Spin, volume 5:03, page 1550004. World Scientific, 2015.
- [86] Somnath Jana, Ronny Knut, Shreyas Muralidhar, Rameez Saeed Malik, Robert Stefanuik, Johan Åkerman, Olof Karis, Christian Schüßler-Langeheine, and Niko Pontius. Experimental confirmation of the delayed Ni demagnetization in FeNi alloy. Applied Physics Letters, 120(10), 2022.
- [87] Peter C. Johnsen, Sinéad A. Ryan, Christian Gentry, Anya Grafov, Henry Kapteyn, and Margaret Murnane. A beamline for ultrafast extreme ultraviolet magneto-optical spectroscopy in reflection near the shot noise limit. Review of Scientific Instruments, 94(3):033001, 2023.
- [88] Alexey Kimel, Anatoly Zvezdin, Sangeeta Sharma, Samuel Shallcross, Nuno de Sousa, Antonio García-Martín, Georgeta Salvan, Jaroslav Hamrle, Ondřej Stejskal, Jeffrey McCord, Silvia Tacchi, Giovanni Carlotti, Pietro Gambardella, Gian Salis, Markus Münzenberg, Martin Schultze, Vasily Temnov, Igor V. Bychkov, Leonid N. Kotov, Nicolò Maccaferri, Daria Ignatyeva, Vladimir Belotelov, Claire Donnelly, Aurelio Hierro Rodriguez, Iwao Matsuda, Thierry Ruchon, Mauro Fanciulli, Maurizio Sacchi, Chunhui Rita Du, Hailong Wang, N. Peter Armitage, Mathias Schubert, Vanya Darakchieva, Bilu Liu, Ziyang Huang, Baofu Ding, Andreas Berger, and Paolo Vavassori. The 2022 magneto-optics roadmap. Journal of Physics D: Applied Physics, 55(46):463003, 2022.

- [89] Andrei Kirilyuk, Alexey V. Kimel, and Theo Rasing. Ultrafast optical manipulation of magnetic order. *Reviews of Modern Physics*, 82(3):2731–2784, 2010.
- [90] Chan La-O-Vorakiat, Mark Siemens, Margaret M. Murnane, Henry C. Kapteyn, Stefan Mathias, Martin Aeschlimann, Patrik Grychtol, Roman Adam, Claus M. Schneider, Justin M. Shaw, Hans Nembach, and T. J. Silva. Ultrafast Demagnetization Dynamics at the M Edges of Magnetic Elements Observed Using a Tabletop High-Harmonic Soft X-Ray Source. *Physical Review Letters*, 103(25):257402, 2009.
- [91] I. Radu, K. Vahaplar, C. Stamm, T. Kachel, N. Pontius, H. A. Dürr, T. A. Ostler, J. Barker, R. F. L. Evans, R. W. Chantrell, A. Tsukamoto, A. Itoh, A. Kirilyuk, Th Rasing, and A. V. Kimel. Transient ferromagnetic-like state mediating ultrafast reversal of antiferromagnetically coupled spins. *Nature*, 472(7342):205–208, 2011.
- [92] Phoebe Tengdin, Christian Gentry, Adam Blonsky, Dmitriy Zusin, Michael Gerrity, Lukas Hellbrück, Moritz Hofherr, Justin Shaw, Yaroslav Kvashnin, Erna K. Delczeg-Czirjak, Monika Arora, Hans Nembach, Tom J. Silva, Stefan Mathias, Martin Aeschlimann, Henry C. Kapteyn, Danny Thonig, Konstantinos Koumpouras, Olle Eriksson, and Margaret M. Murnane. Direct light-induced spin transfer between different elements in a spintronic Heusler material via femtosecond laser excitation. *Science Advances*, 6(3):eaaz1100, 2020.
- [93] M. Hofherr, S. Häuser, J. K. Dewhurst, P. Tengdin, S. Sakshath, H. T. Nembach, S. T. Weber, J. M. Shaw, T. J. Silva, H. C. Kapteyn, M. Cinchetti, B. Rethfeld, M. M. Murnane, D. Steil, B. Stadtmüller, S. Sharma, M. Aeschlimann, and S. Mathias. Ultrafast optically induced spin transfer in ferromagnetic alloys. *Science Advances*, 6(3):eaay8717, 2020.
- [94] John Kay Dewhurst, Peter Elliott, Sam Shallcross, Eberhard K. U. Gross, and Sangeeta Sharma. Laser-Induced Intersite Spin Transfer. *Nano Letters*, 18(3):1842–1848, 2018.
- [95] Daniel Steil, Jakob Walowski, Felicitas Gerhard, Tobias Kiessling, Daniel Ebke, Andy Thomas, Takahide Kubota, Mikihiro Oogane, Yasuo Ando, Johannes Otto, Andreas Mann, Moritz Hofherr, Peter Elliott, John Kay Dewhurst, Günter Reiss, Laurens Molenkamp, Martin Aeschlimann, Mirko Cinchetti, Markus Münzenberg, Sangeeta Sharma, and Stefan Mathias. Efficiency of ultrafast optically induced spin transfer in Heusler compounds. *Physical Review Research*, 2(2):023199, 2020.
- [96] Felix Willems, Clemens von Korff Schmising, Christian Strüber, Daniel Schick, Dieter W Engel, JK Dewhurst, Peter Elliott, Sangeeta Sharma, and Stefan Eisebitt. Optical inter-site spin transfer probed by energy and spin-resolved transient absorption spectroscopy. *Nature Communications*, 11(1):871, 2020.
- [97] Sinéad A. Ryan, Peter C. Johnsen, Mohamed F. Elhanoty, Anya Grafov, Na Li, Anna Delin, Anastasios Markou, Edouard Lesne, Claudia Felser, Olle Eriksson, Henry C. Kapteyn, Oscar Grånäs, and Margaret M. Murnane. Optically controlling the competition between spin flips and intersite spin transfer in a Heusler half-metal on sub-100-fs time scales. *Science Advances*, 9(45):ead1428, 2023.
- [98] Tanja Graf, Claudia Felser, and Stuart S. P. Parkin. Simple rules for the understanding of Heusler compounds. *Progress in Solid State Chemistry*, 39(1):1–50, 2011.

- [99] I Galanakis, PH Dederichs, and N Papanikolaou. Slater-pauling behavior and origin of the half-metallicity of the full-heusler alloys. Physical Review B, 66(17):174429, 2002.
- [100] W. Al-Sawai, Hsin Lin, R. S. Markiewicz, L. A. Wray, Y. Xia, S.-Y. Xu, M. Z. Hasan, and A. Bansil. Topological electronic structure in half-Heusler topological insulators. Physical Review B, 82(12):125208, 2010.
- [101] Di Xiao, Yugui Yao, Wanxiang Feng, Jun Wen, Wenguang Zhu, Xing-Qiu Chen, G. Malcolm Stocks, and Zhenyu Zhang. Half-Heusler Compounds as a New Class of Three-Dimensional Topological Insulators. Physical Review Letters, 105(9):096404, 2010.
- [102] Hsin Lin, L. Andrew Wray, Yuqi Xia, Suyang Xu, Shuang Jia, Robert J. Cava, Arun Bansil, and M. Zahid Hasan. Half-Heusler ternary compounds as new multifunctional experimental platforms for topological quantum phenomena. Nature Materials, 9(7):546–549, 2010.
- [103] Stanislav Chadov, Xiaoliang Qi, Jürgen Kübler, Gerhard H. Fecher, Claudia Felser, and Shou Cheng Zhang. Tunable multifunctional topological insulators in ternary Heusler compounds. Nature Materials, 9(7):541–545, 2010.
- [104] I. Galanakis, Ph Mavropoulos, and P. H. Dederichs. Electronic structure and Slater–Pauling behaviour in half-metallic Heusler alloys calculated from first principles. Journal of Physics D: Applied Physics, 39(5):765, 2006.
- [105] T. Klimczuk, C. H. Wang, K. Gofryk, F. Ronning, J. Winterlik, G. H. Fecher, J.-C. Griveau, E. Colineau, C. Felser, J. D. Thompson, D. J. Safarik, and R. J. Cava. Superconductivity in the Heusler family of intermetallics. Physical Review B, 85(17):174505, 2012.
- [106] J. H. Wernick, G. W. Hull, T. H. Geballe, J. E. Bernardini, and J. V. Waszczak. Superconductivity in ternary Heusler intermetallic compounds. Material Letters, 2(2):90–92, 1983.
- [107] C. Uher, J. Yang, S. Hu, D. T. Morelli, and G. P. Meisner. Transport properties of pure and doped MNiSn (M=Zr, Hf). Physical Review B, 59(13):8615–8621, 1999.
- [108] S. Sakurada and N. Shutoh. Effect of Ti substitution on the thermoelectric properties of (Zr,Hf)NiSn half-Heusler compounds. Applied Physics Letters, 86(8):082105, 2005.
- [109] Chenguang Fu, Shengqiang Bai, Yintu Liu, Yunshan Tang, Lidong Chen, Xinbing Zhao, and Tiejun Zhu. Realizing high figure of merit in heavy-band p-type half-Heusler thermoelectric materials. Nature Communications, 6(1):8144, 2015.
- [110] Kaiyang Xia, Chaoliang Hu, Chenguang Fu, Xinbing Zhao, and Tiejun Zhu. Half-Heusler thermoelectric materials. Applied Physics Letters, 118(14):140503, 2021.
- [111] F. Casper, T. Graf, S. Chadov, B. Balke, and C. Felser. Half-Heusler compounds: novel materials for energy and spintronic applications. Semiconductor Science and Technology, 27(6):063001, 2012.
- [112] Kelvin Elphick, William Frost, Marjan Samiepour, Takahide Kubota, Koki Takanashi, Hiroaki Sukegawa, Seiji Mitani, and Atsufumi Hirohata. Heusler alloys for spintronic devices: review on recent development and future perspectives. Science and Technology of Advanced Materials, 22(1), 2021.

- [113] Lakhan Bainsla and K. G. Suresh. Equiatomic quaternary Heusler alloys: A material perspective for spintronic applications. *Applied Physics Reviews*, 3(3):031101, 2016.
- [114] Koichiro Inomata, Susumu Okamura, Ryota Goto, and Nobuki Tezuka. Large Tunneling Magnetoresistance at Room Temperature Using a Heusler Alloy with the B2 Structure. *Japanese Journal of Applied Physics.*, 42(4B):L419, 2003.
- [115] S Kämmerer, Andy Thomas, Andreas Hütten, and Günter Reiss.  $Co_2MnSi$  Heusler alloy as magnetic electrodes in magnetic tunnel junctions. *Applied Physics Letters*, 85(1):79–81, 2004.
- [116] P. G. van Engen, K. H. J. Buschow, R. Jongebreur, and M. Erman. PtMnSb, a material with very high magneto-optical Kerr effect. *Applied Physics Letters*, 42(2):202–204, 1983.
- [117] R. A. de Groot, F. M. Mueller, P. G. van Engen, and K. H. J. Buschow. New Class of Materials: Half-Metallic Ferromagnets. *Physical Review Letters*, 50(25):2024–2027, 1983.
- [118] L. Chioncel, M. I. Katsnelson, R. A. de Groot, and A. I. Lichtenstein. Nonquasiparticle states in the half-metallic ferromagnet NiMnSb. *Physical Review B*, 68(14):144425, 2003.
- [119] P. Elliott, T. Müller, J. K. Dewhurst, S. Sharma, and E. K. U. Gross. Ultrafast laser induced local magnetization dynamics in Heusler compounds. *Scientific Reports*, 6(1):38911, 2016.
- [120] Georg M. Müller, Jakob Walowski, Marija Djordjevic, Gou-Xing Miao, Arunava Gupta, Ana V. Ramos, Kai Gehrke, Vasily Moshnyaga, Konrad Samwer, Jan Schmalhorst, Andy Thomas, Andreas Hütten, Günter Reiss, Jagadeesh S. Moodera, and Markus Münzenberg. Spin polarization in half-metals probed by femtosecond spin excitation. *Nature Materials*, 8(1):56–61, 2009.
- [121] Jan-Peter Wüstenberg, Daniel Steil, Sabine Alebrand, Tobias Roth, Martin Aeschlimann, and Mirko Cinchetti. Ultrafast magnetization dynamics in the half-metallic Heusler alloy  $Co_2Cr_{0.6}Fe_{0.4}Al$ . *Physica Status Solidi (b)*, 248(10), 2011.
- [122] Andreas Mann, Jakob Walowski, Markus Münzenberg, Stefan Maat, Matthew J. Carey, Jeffrey R. Childress, Claudia Mewes, Daniel Ebke, Volker Drewello, Günter Reiss, and Andy Thomas. Insights into Ultrafast Demagnetization in Pseudogap Half-Metals. *Physical Review X*, 2(4):041008, 2012.
- [123] Evangelos Golias, Ivar Kumberg, Ismet Gelen, Sangeeta Thakur, Jendrik Gördes, Rahil Hosseinifar, Quentin Guillet, JK Dewhurst, S Sharma, C Schüßler-Langeheine, et al. Ultrafast optically induced ferromagnetic state in an elemental antiferromagnet. *Physical Review Letters*, 126(10):107202, 2021.
- [124] Florian Siegrist, Julia A. Gessner, Marcus Ossiander, Christian Denker, Yi-Ping Chang, Malte C. Schröder, Alexander Guggenmos, Yang Cui, Jakob Walowski, Ulrike Martens, J. K. Dewhurst, Ulf Kleineberg, Markus Münzenberg, Sangeeta Sharma, and Martin Schultze. Light-wave dynamic control of magnetism. *Nature*, 571(7764):240–244, 2019.
- [125] Marcel Hennes, Benedikt Rösner, Valentin Chardonnet, Gheorghe S. Chiuzbaian, Renaud Delaunay, Florian Döring, Vitaliy A. Guzenko, Michel Hehn, Romain Jarrier, Armin Kleibert, Maxime Lebugle, Jan Lüning, Gregory Malinowski, Aladine Merhe, Denys Naumenko, Ivaylo P. Nikolov, Ignacio Lopez-Quintas, Emanuele Pedersoli, Tatiana Savchenko, Benjamin Watts,

- Marco Zangrando, Christian David, Flavio Capotondi, Boris Vodungbo, and Emmanuelle Jal. Time-Resolved XUV Absorption Spectroscopy and Magnetic Circular Dichroism at the Ni  $M_{2,3}$ -Edges. Applied Sciences, 11(1):325, 2021.
- [126] Kelvin Yao, Felix Willems, Clemens von Korff Schmising, Ilie Radu, Christian Strüber, Daniel Schick, Dieter Engel, Arata Tsukamoto, J. K. Dewhurst, Sangeeta Sharma, and Stefan Eisebitt. Distinct spectral response in M-edge magnetic circular dichroism. Physical Review B, 102(10):100405, 2020.
- [127] Hung-Tzu Chang, Alexander Guggenmos, Scott K. Cushing, Yang Cui, Naseem Ud Din, Shree Ram Acharya, Ilana J. Porter, Ulf Kleineberg, Volodymyr Turkowski, Talat S. Rahman, Daniel M. Neumark, and Stephen R. Leone. Electron thermalization and relaxation in laser-heated nickel by few-femtosecond core-level transient absorption spectroscopy. Physical Review B, 103(6):064305, 2021.
- [128] Tobias Lojewski, Mohamed F. Elhanoty, Loïc Le Guyader, Oscar Grånäs, Naman Agarwal, Christine Boeglin, Robert Carley, Andrea Castoldi, Christian David, Carsten Deiter, Florian Döring, RobinY Engel, Florian Erdinger, Hans Fangohr, Carlo Fiorini, Peter Fischer, Natalia Gerasimova, Rafael Gort, Frank deGroot, Karsten Hansen, Steffen Hauf, David Hickin, Manuel Izquierdo, Benjamin E. Van Kuiken, Yaroslav Kvashnin, Charles-Henri Lambert, David Lomidze, Stefano Maffessanti, Laurent Mercadier, Giuseppe Mercurio, Piter S. Miedema, Katharina Ollefs, Matthias Pace, Matteo Porro, Javad Rezvani, Benedikt Rösner, Nico Rothenbach, Andrey Samartsev, Andreas Scherz, Justina Schlappa, Christian Stamm, Martin Teichmann, Patrik Thunström, Monica Turcato, Alexander Yaroslavtsev, Jun Zhu, Martin Beye, Heiko Wende, Uwe Bovensiepen, Olle Eriksson, and Andrea Eschenlohr. The interplay of local electron correlations and ultrafast spin dynamics in fcc Ni. Material Research Letters, 11(8):655–661, 2023.
- [129] K. Carva, D. Legut, and P. M. Oppeneer. Influence of laser-excited electron distributions on the X-ray magnetic circular dichroism spectra: Implications for femtosecond demagnetization in Ni. Europhysics Letters, 86(5):57002, 2009.
- [130] Loïc Le Guyader, Daniel J. Higley, Matteo Pancaldi, Tianmin Liu, Zhao Chen, Tyler Chase, Patrick W. Granitzka, Giacomo Coslovich, Alberto A. Lutman, Georgi L. Dakovski, William F. Schlotter, Padraic Shafer, Elke Arenholz, Olav Hellwig, Mark L. M. Lalieu, Bert Koopmans, Alexander H. Reid, Stefano Bonetti, Joachim Stöhr, and Hermann A. Dürr. State-resolved ultrafast charge and spin dynamics in [Co/Pd] multilayers. Applied Physics Letters, 120(3):032401, 2022.
- [131] Mohamed F. Elhanoty, Olle Eriksson, Ronny Knut, Olof Karis, and Oscar Grånäs. Element-selective ultrafast magnetization dynamics of hybrid Stoner-Heisenberg magnets. Physical Review B, 105(10):L100401, 2022.
- [132] Justin M Shaw, Ronny Knut, Abigail Armstrong, Sumanta Bhandary, Yaroslav Kvashnin, Danny Thonig, Erna K Delczeg-Czirjak, Olof Karis, TJ Silva, Eugen Weschke, et al. Quantifying spin-mixed states in ferromagnets. Physical Review Letters, 127(20):207201, 2021.
- [133] H. Ebert, D. Ködderitzsch, and J. Minár. Calculating condensed matter properties using the KKR-Green’s function method—recent developments and applications. Reports on Progress in Physics, 74(9):096501, 2011.

- [134] Y. Kubo, S. Ishida, and J. Ishida. Optical spectrum of  $Cu_2MnAl$ . Journal of Physics F: Metal Physics, 11(11):2443, 1981.
- [135] Y. Kubo, N. Takakura, and S. Ishida. Optical spectra of the ferromagnetic Heusler alloys. Journal of Physics F: Metal Physics, 13(1):161, 1983.
- [136] Y. V. Kudryavtsev, Y. P. Lee, and J. Y. Rhee. Dependence of the optical and magneto-optical properties and electronic structures on the atomic order in NiMnIn Heusler alloys. Physical Review B, 69(19):195104, 2004.
- [137] Kohei Yamamoto, Souliman El Moussaoui, Yasuyuki Hirata, Susumu Yamamoto, Yuya Kubota, Shigeki Owada, Makina Yabashi, Takeshi Seki, Koki Takanashi, Iwao Matsuda, and Hiroki Wadati. Element-selectively tracking ultrafast demagnetization process in Co/Pt multilayer thin films by the resonant magneto-optical Kerr effect. Applied Physics Letters, 116(17):172406, 2020.
- [138] Ilya Belopolski, Kaustuv Manna, Daniel S. Sanchez, Guoqing Chang, Benedikt Ernst, Jiaxin Yin, Songtian S. Zhang, Tyler Cochran, Nana Shumiya, Hao Zheng, Bahadur Singh, Guang Bian, Daniel Multer, Maksim Litskevich, Xiaoting Zhou, Shin-Ming Huang, Baokai Wang, Tay-Rong Chang, Su-Yang Xu, Arun Bansil, Claudia Felser, Hsin Lin, and M. Zahid Hasan. Discovery of topological Weyl fermion lines and drumhead surface states in a room temperature magnet. Science, 365(6459):1278–1281, 2019.
- [139] Satya N. Guin, Kaustuv Manna, Jonathan Noky, Sarah J. Watzman, Chenguang Fu, Nitesh Kumar, Walter Schnelle, Chandra Shekhar, Yan Sun, Johannes Gooth, and Claudia Felser. Anomalous Nernst effect beyond the magnetization scaling relation in the ferromagnetic Heusler compound  $Co_2MnGa$ . NPG Asia Materials, 11(1):1–9, 2019.
- [140] Guoqing Chang, Su-Yang Xu, Xiaoting Zhou, Shin-Ming Huang, Bahadur Singh, Baokai Wang, Ilya Belopolski, Jiaxin Yin, Songtian Zhang, Arun Bansil, Hsin Lin, and M. Zahid Hasan. Topological Hopf and Chain Link Semimetal States and Their Application to  $Co_2MnGa$ . Physical Review Letters, 119(15):156401, 2017.
- [141] Helena Reichlova, Richard Schlitz, Sebastian Beckert, Peter Swekis, Anastasios Markou, Yi-Cheng Chen, Dominik Kriegner, Savio Fabretti, Gyu Hyeon Park, Anna Niemann, Shashank Sudheendra, Andy Thomas, Kornelius Nielsch, Claudia Felser, and Sebastian T. B. Goennenwein. Large anomalous Nernst effect in thin films of the Weyl semimetal  $Co_2MnGa$ . Applied Physics Letters, 113(21):212405, 2018.
- [142] Anastasios Markou, Dominik Kriegner, Jacob Gayles, Liguozhang, Yi-Cheng Chen, Benedikt Ernst, Yu-Hong Lai, Walter Schnelle, Ying-Hao Chu, Yan Sun, and Claudia Felser. Thickness dependence of the anomalous Hall effect in thin films of the topological semimetal  $Co_2MnGa$ . Physical Review B, 100(5):054422, 2019.
- [143] Kaustuv Manna, Lukas Muechler, Ting-Hui Kao, Rolf Stinshoff, Yang Zhang, Johannes Gooth, Nitesh Kumar, Guido Kreiner, Klaus Koepf, Roberto Car, Jürgen Kübler, Gerhard H. Fecher, Chandra Shekhar, Yan Sun, and Claudia Felser. From Colossal to Zero: Controlling the Anomalous Hall Effect in Magnetic Heusler Compounds via Berry Curvature Design. Physical Review X, 8(4):041045, 2018.

- [144] Chris P. Weber. Ultrafast investigation and control of Dirac and Weyl semimetals. Journal of Applied Physics, 129(7):070901, 2021.
- [145] Christina Möller, Henrike , GS Matthijs Jansen, Maren Schumacher, Mariana Brede, John Kay Dewhurst, Marcel Reutzler, Daniel Steil, Sangeeta Sharma, and Stefan Mathias. Verification of ultrafast spin transfer effects in iron-nickel alloys. Communications Physics, 7(1):74, 2024.
- [146] Justin M Shaw, Erna K Delczeg-Czirjak, Eric RJ Edwards, Yaroslav Kvashnin, Danny Thonig, Martin AW Schoen, Matt Pufall, Michael L Schneider, Thomas J Silva, Olof Karis, et al. Magnetic damping in sputter-deposited  $Co_2MnGe$  Heusler compounds with  $A_2$ ,  $B_2$ , and  $L_2_1$  orders: Experiment and theory. Physical Review B, 97(9):094420, 2018.
- [147] S Picozzi, A Continenza, and Arthur J Freeman.  $Co_2MnX$  ( $X = Si, Ge, Sn$ ) Heusler compounds: An ab initio study of their structural, electronic, and magnetic properties at zero and elevated pressure. Physical Review B, 66(9):094421, 2002.
- [148] K Özdoğan, E Şaşıoğlu, B Aktaş, and Iosif Galanakis. Doping and disorder in the  $Co_2MnAl$  and  $Co_2MnGa$  half-metallic Heusler alloys. Physical Review B, 74(17):172412, 2006.
- [149] C Guillemard, S Petit-Watelot, L Pasquier, D Pierre, J Ghanbaja, JC Rojas-Sánchez, A Bataille, J Rault, P Le Fèvre, F Bertran, et al. Ultralow magnetic damping in  $Co_2Mn$ -based Heusler compounds: Promising materials for spintronics. Physical Review Applied, 11(6):064009, 2019.
- [150] Barthélémy Pradines, Rémi Arras, Iman Abdallah, N Biziere, and Lionel Calmels. First-principles calculation of the effects of partial alloy disorder on the static and dynamic magnetic properties of  $Co_2MnSi$ . Physical Review B, 95(9):094425, 2017.
- [151] S Picozzi, AJFA Continenza, and AJ Freeman. Role of structural defects on the half-metallic character of  $Co_2MnGe$  and  $Co_2MnSi$  Heusler alloys. Physical Review B, 69(9):094423, 2004.
- [152] Mahdi Sargolzaei, Manuel Richter, Klaus Koepernik, Ingo Opahle, Helmut Eschrig, and Igor Chaplygin. Spin and orbital magnetism in full Heusler alloys: A density functional theory study of  $Co_2YZ$  ( $Y = Mn, Fe; Z = Al, Si, Ga, Ge$ ). Physical Review B, 74(22):224410, 2006.
- [153] P. J. Webster. Magnetic and chemical order in Heusler alloys containing cobalt and manganese. Journal of Physics and Chemistry of Solids, 32(6):1221–1231, 1971.
- [154] K.H.J. Buschow. Encyclopedia of Materials - Science and Technology, Volumes 1-11 - Magnetism in Solids: General Introduction. Elsevier, 2001.
- [155] Se Kwon Kim, Geoffrey S. D. Beach, Kyung-Jin Lee, Teruo Ono, Theo Rasing, and Hyunsoo Yang. Ferrimagnetic spintronics. Nature Materials, 21(1):24–34, 2022.
- [156] Sergei Ovcharenko, Mikhail Gaponov, Alexey Klimov, Nicolas Tiercelin, Philippe Pernod, Elena Mishina, Alexandr Sigov, and Vladimir Preobrazhensky. Photoinduced spin dynamics in a uniaxial intermetallic heterostructure  $TbCo_2/FeCo$ . Scientific Reports, 10(1):15785, 2020.
- [157] Alexey Klimov, Nicolas Tiercelin, Yannick Dusch, Stefano Giordano, Théo Mathurin, Philippe Pernod, Vladimir Preobrazhensky, Anton Churbanov, and Sergei Nikitov. Magnetoelectric write and read operations in a stress-mediated multiferroic memory cell. Applied Physics Letters, 110(22):222401, 2017.

- [158] D Connor Jones, Suvadip Das, Hari Bhandari, Xiaoxiong Liu, Peter Siegfried, Madhav P Ghimire, Stepan S Tsirkin, II Mazin, and Nirmal J Ghimire. Origin of spin reorientation and intrinsic anomalous hall effect in the kagome ferrimagnet  $TbMn_6Sn_6$ . arXiv preprint arXiv:2203.17246, 2022.
- [159] Jia-Xin Yin, Wenlong Ma, Tyler A. Cochran, Xitong Xu, Songtian S. Zhang, Hung-Ju Tien, Nana Shumiya, Guangming Cheng, Kun Jiang, Biao Lian, Zhida Song, Guoqing Chang, Ilya Belopolski, Daniel Multer, Maksim Litskevich, Zi-Jia Cheng, Xian P. Yang, Bianca Swidler, Huibin Zhou, Hsin Lin, Titus Neupert, Ziqiang Wang, Nan Yao, Tay-Rong Chang, Shuang Jia, and M. Zahid Hasan. Quantum-limit Chern topological magnetism in  $TbMn_6Sn_6$ . Nature, 583(7817):533–536, 2020.
- [160] H. Horner and C. M. Varma. Nature of Spin-Reorientation Transitions. Physical Review Letters, 20(16):845–846, 1968.
- [161] Marko Wietstruk, Alexey Melnikov, Christian Stamm, Torsten Kachel, Niko Pontius, Muhammad Sultan, Cornelius Gahl, Martin Weinelt, Hermann A. Dürr, and Uwe Bovensiepen. Hot-Electron-Driven Enhancement of Spin-Lattice Coupling in Gd and Tb  $4f$  Ferromagnets Observed by Femtosecond X-Ray Magnetic Circular Dichroism. Physical Review Letters, 106(12):127401, 2011.
- [162] V. López-Flores, N. Berggaard, V. Halté, C. Stamm, N. Pontius, M. Hehn, E. Otero, E. Beaurepaire, and C. Boeglin. Role of critical spin fluctuations in ultrafast demagnetization of transition-metal rare-earth alloys. Physical Review B, 87(21):214412, 2013.
- [163] J. H. Mentink, J. Hellsvik, D. V. Afanasiev, B. A. Ivanov, A. Kirilyuk, A. V. Kimel, O. Eriksson, M. I. Katsnelson, and Th. Rasing. Ultrafast Spin Dynamics in Multisublattice Magnets. Physical Review Letters, 108(5):057202, 2012.
- [164] R. Medapalli, I. Razdolski, M. Savoini, A. R. Khorsand, A. Kirilyuk, A. V. Kimel, Th. Rasing, A. M. Kalashnikova, A. Tsukamoto, and A. Itoh. Efficiency of ultrafast laser-induced demagnetization in  $Gd_xFe_{100-x-y}Co_y$  alloys. Physical Review B, 86(5):054442, 2012.
- [165] Thomas L Gilbert. A phenomenological theory of damping in ferromagnetic materials. IEEE transactions on magnetics, 40(6):3443–3449, 2004.
- [166] B Chafik El Idrissi, G Venturini, B Malaman, and D Fruchart. Magnetic structures of  $TbMn_6Sn_6$  and  $HoMn_6Sn_6$  compounds from neutron diffraction study. Journal of the Less Common Metals, 175(1):143–154, 1991.
- [167] M Sato and Y Ishii. Simple and approximate expressions of demagnetizing factors of uniformly magnetized rectangular rod and cylinder. Journal of Applied Physics, 66(2):983–985, 1989.
- [168] Jack B Collings, Ricardo Rama-Eiroa, Rubén M Otxoa, Richard FL Evans, and Roy W Chantrell. Generalized form of the magnetic anisotropy field in micromagnetic and atomistic spin models. Physical Review B, 107(6):064413, 2023.
- [169] Oksana Chubykalo-Fesenko, Ulrich Nowak, Roy W Chantrell, and D Garanin. Dynamic approach for micromagnetics close to the curie temperature. Physical Review B, 74(9):094436, 2006.

- [170] A Lyberatos and K Yu Guslienko. Thermal stability of the magnetization following thermomagnetic writing in perpendicular media. Journal of Applied Physics, 94(2):1119–1129, 2003.
- [171] Christina Möller, Henrike Probst, Johannes Otto, Karen Stroh, Carsten Mahn, Sabine Steil, Vasily Moshnyaga, GS Jansen, Daniel Steil, and Stefan Mathias. Ultrafast element-resolved magneto-optics using a fiber-laser-driven extreme ultraviolet light source. Review of Scientific Instruments, 92(6), 2021.
- [172] Emrah Turgut. Studying laser-induced spin currents using ultrafast extreme ultraviolet light. PhD thesis, University of Colorado at Boulder, 2014.
- [173] Kelvin Yao, Felix Willems, Clemens von Korff Schmising, Christian Strüber, Piet Hessian, Bastian Pfau, Daniel Schick, Dieter Engel, Kathinka Gerlinger, Michael Schneider, et al. A tabletop setup for ultrafast helicity-dependent and element-specific absorption spectroscopy and scattering in the extreme ultraviolet spectral range. Review of Scientific Instruments, 91(9), 2020.
- [174] F Willems, CTL Smeenk, N Zhavoronkov, O Kornilov, I Radu, M Schmidbauer, M Hanke, C von Korff Schmising, MJJ Vrakking, and S Eisebitt. Probing ultrafast spin dynamics with high-harmonic magnetic circular dichroism spectroscopy. Physical Review B, 92(22):220405, 2015.
- [175] Mauro Nisoli, Sandro De Silvestri, and Orazio Svelto. Generation of high energy 10 fs pulses by a new pulse compression technique. Applied Physics Letters, 68(20):2793–2795, 1996.
- [176] Mauro Nisoli, Sandro De Silvestri, Orazio Svelto, R Szipöcs, K Ferencz, Ch Spielmann, S Sartania, and Ferenc Krausz. Compression of high-energy laser pulses below 5 fs. Optics Letters, 22(8):522–524, 1997.
- [177] Xinhua Xie, Yunpei Deng, and Steven L Johnson. Compact and robust supercontinuum generation and post-compression using multiple thin plates. High Power Laser Science and Engineering, 9:e66, 2021.
- [178] Sylvianne DC Roscam Abbing, Filippo Campi, Alexandra Zeltsi, Peter Smorenburg, and Peter M Kraus. Divergence and efficiency optimization in polarization-controlled two-color high-harmonic generation. Scientific Reports, 11(1):24253, 2021.
- [179] Ofer Kfir, Eliyahu Bordo, Gil Ilan Haham, Oren Lahav, Avner Fleischer, and Oren Cohen. In-line production of a bi-circular field for generation of helically polarized high-order harmonics. Applied Physics Letters, 108(21), 2016.
- [180] Zack Savitsky. Researchers discover new kind of magnetism. Science, 383(6683):574–575, 2024.
- [181] Isabelle Dumé | physics world IOP publishing. New type of magnetism appears in a layered semiconductor. <https://physicsworld.com/a/new-type-of-magnetism-appears-in-a-layered-semiconductor/#:~:text=Known%20as%20kinetic%20magnetism%2C%20and,of%20electron%20exchange%20interactions%20vanishes.>, 2024. Accessed: 2024-02-23.

- [182] Libor Šmejkal, Jairo Sinova, and Tomas Jungwirth. Beyond conventional ferromagnetism and antiferromagnetism: A phase with nonrelativistic spin and crystal rotation symmetry. Physical Review X, 12(3):031042, 2022.